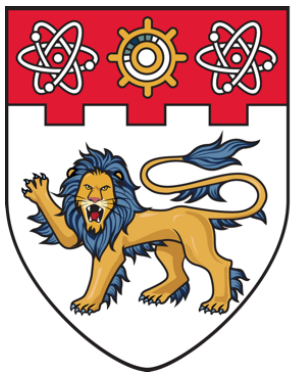

NANYANG TECHNOLOGICAL UNIVERSITY
SINGAPORE

Cu-M-Chalcogenides as catalysts for electrochemical CO_2 reduction

Daniel Goh Yong Yi

SCHOOL OF MATERIALS SCIENCE AND ENGINEERING

2024

Cu-M-Chalcogenides as catalysts for electrochemical CO_2 reduction

Daniel Goh Yong Yi

SCHOOL OF MATERIALS SCIENCE AND ENGINEERING

A thesis submitted to the Nanyang Technological University
in partial fulfilment of the requirement for the degree of
Doctor of Philosophy

2024

Statement of Originality

I hereby certify that the work embodied in this thesis is the result of original research, is free of plagiarised materials, and has not been submitted for a higher degree to any other University or Institution.

22 July 2024
. . . . . .
Date

. . . . . .
Daniel Goh Yong Yi

Supervisor Declaration Statement

I have reviewed the content and presentation style of this thesis and declare it is free of plagiarism and of sufficient grammatical clarity to be examined. To the best of my knowledge, the research and writing are those of the candidate except as acknowledged in the Author Attribution Statement. I confirm that the investigations were conducted in accord with the ethics policies and integrity standards of Nanyang Technological University and that the research data are presented honestly and without prejudice.

22 July 2024

. . . . . .

Date

. . . . . .

Professor Lydia Helena Wong

Authorship Attribution Statement

This thesis contains material from one paper published in the following peer-reviewed journal(s) / from papers accepted at conferences in which I am listed as an author.

Chapter 5 is published as D.Y.Y. Goh, K.M. Yam, L. Rekhi, A.D. Handoko, Y.C. Tan, Y. Wang, J.M.R. Tan, T.S. Choksi, Y. Lum, and L.H. Wong. Covalency-aided electrochemical CO_2 reduction to CO on sulfide-derived Cu–Sb. *Journal of Materials Chemistry A*, **12**, 1840-1851 (2024). DOI: 10.1039/D3TA04777F.

The contributions of the co-authors are as follows:

- Prof Wong and Prof Lum provided the initial project direction and edited the manuscript drafts.
- I prepared the manuscript drafts. The manuscript was revised by Dr A.D. Handoko and Dr Y.C. Tan.
- I co-designed the study with Prof Wong and Prof Lum and performed all the laboratory work at the School of Materials Science and Engineering (NTU MSE) and the Institute of Materials Research and Engineering (A*STAR IMRE). I also analyzed the data.
- XRD, SEM and EDX was conducted by me in the Facility for Analysis, Characterization, Testing and Simulation.
- Dr K.M. Yam, L. Rekhi and Prof T.S. Choksi performed the DFT simulations.
- Dr J.M.R. Tan designed the synthesis procedure.
- Dr Y. Wang carried out the TEM characterization.

22 July 2024 . . . . . .
Date

. . . . . .
Daniel Goh Yong Yi

Abstract

Electrochemical CO_2 reduction (CO_2RR) is gaining attention in research as a promising way to produce chemical feedstocks. CO_2 can be reduced to several products, such as $HCOO^-$, CO, as well as reduced products such as CH_4, C_2H_4 and C_2H_5OH. CO and C_2H_4 in particular are valuable products as CO is a useful intermediate for the production of synthetic kerosene or green methanol, while C_2H_4 is useful to make plastics. However, achieving high selectivity and a high current density with low-cost catalysts to these products is challenging. For example, the state-of-the-art Ag and Au catalysts for CO_2 reduction to CO are expensive, while Cu catalyst for CO_2 reduction to C_2H_4 is not selective. Scaling up to high current density is also challenging on these catalysts due to the competing H_2 evolution reaction (HER). Understanding the underlying mechanisms for the catalyst to bind to CO_2 and relevant intermediates is important to achieve these aims.

As copper is the only metal known to produce reduced products, but at the same time is also capable of producing $HCOO^-$ and CO, it is the most flexible starting point for the construction of more complex catalysts that favour certain reaction products. For example, oxide-derived copper has been shown to favour liquid products, while various bimetallic catalysts consisting of copper and another metallic element have been tried for increasing copper's selectivity to CO, CH_4 or C_2H_4. On another hand, sulfide-derived catalysts have been shown to produce almost exclusively $HCOO^-$ and attempts to use this method for other products has not been very successful. This is despite calculations showing that sulfur can have an effect in stabilizing *COOH relative to *CO to tune selectivity towards CO. Some particularly successful studies have shown that CdS produces CO and is effectively the only sulfide-derived monometallic catalyst thus far to do so. In contrast to two-element catalysts which have been extensively researched, three-element catalysts are comparatively rare in the literature. This thesis focuses on Cu-M-S/Se as possible three-element catalysts to achieve selective CO_2 reduction, preferably to CO or even reduced products.

In the first work, nine Cu-M-S bimetallics (M=In, Sn, Sb, Bi, Ga, Ge, Ag, Co, Fe) are tested. It is found that the Cu-Sb-S system is able to selectively produce CO and the sulfoselenide Cu-Sb-S/Se is then tested. It is also found that the sulfide-derived version is better than the sulfoselenide-derived one. Other elements (including In, Sn, as well as other metals such as Ag, Co, Fe, Ga, Ge) as the second metal are not able to do so, and this is linked to the ability of the metal sulfide to reduce during electrochemical CO_2 reduction to remove excess sulfur, indicating that small amounts of sulfur doping is able to boost CO selectivity while the usual $HCOO^-$ tuning effect is minimized as this effect seems to be greater when sulfur is present in larger amounts.

In the second work, an in-depth study of the Cu-Sb-S system for electrochemical CO_2 reduction is carried out. Three phases, skinnerite (SK, Cu_3SbS_3), tetrahedrite (TH, $Cu_{12}Sb_4S_{13}$) and chalcostibite (CS, $CuSbS_2$) are synthesized and tested for electrochemical CO_2 reduction. The Cu-Sb-S catalysts are found to have high CO selectivities of 50-80%. This is in contrast to the individual control samples of CuS_x and SbS_x that demonstrate a preference towards the formate product. The Cu-Sb-S catalysts are found to lose most of the sulfur during reduction, with post-reduction sulfur content ranging from 2-15% found in EDX and XPS. The differences in CO selectivity between the SK, TH and CS phases are attributed to crystallinity in XRD where a higher amount of sulfur induces a drop in crystallinity in the TH sample, and phase segregation caused by a higher Cu at% resulting in S-doped Cu that produces excess $HCOO^-$ and H_2 by-products. DFT calculations indicate that the substitution of Sb sites with sulfur improves *COOH binding relative to *CO, breaking scaling relations and facilitating subsequent CO (g) formation. It is found that the TH phase results in the highest CO selectivity of 80% at −1.0 V RHE with 37.6 mA cm^{-2} geometric partial current density.

In the third work, the Cu-Sb/Bi-S system is tested to elucidate the role of the second metal. It is found that Sb promotes CO while Bi promotes $HCOO^-$, where the difference likely stems from the miscibility of the second metal with Cu as well as elemental loss. The results indicate that: (1) Sb alloys well with Cu, which weakens the binding of Cu to form CO. (2)

Bi does not alloy very well with Cu, leading to loss of Bi, increasing the amount of sulfur-doped Cu which then results in $HCOO^-$ as well as H_2 formation.

These results point to the limitations of sulfur in three-element catalysts in electrochemical CO_2 reduction, where recommendations are made in the conclusion that: (1) for electrochemical CO_2 reduction, trimetallics are better while (2) for sulfides, photoelectrochemical CO_2 reduction is better.

Lay Summary

Currently, the world obtains 80% its energy from fossil fuels according to the International Energy Agency. As the world population increases in the 21st century, even more energy is needed. However, the burning of fossil fuels is releasing carbon dioxide, a potent greenhouse gas causing climate change. This has resulted in the Earth having warmed 1.2°C since the Industrial Revolution and it is projected that humanity is on track to achieve 2.5-3°C of warming by 2100. This has dangerous consequences for the climate, resulting in natural disasters, more frequent heatwaves and sea level rise. As such, it is vital that humanity shifts to energy sources that do not have CO_2 emissions.

While CO_2 emissions in power generation can easily be reduced or eliminated by switched to renewable sources such as solar, wind and hydroelectricity, and in road transport by electrification to electric vehicles, CO_2 emissions in hard-to-abate sectors such as industry, shipping and aviation are harder to eliminate. In these areas, electrocatalysis can play a vital role. For example, green hydrogen, or hydrogen produced from electrolysis of water, can be used to replace hydrogen produced from natural gas used to produce ammonia, methanol or steel. As a further step, fuels and chemicals produced from the electrochemical reduction of carbon dioxide (CO_2RR) can be used to replace fossil fuels used in transport or industry. Carbon monoxide is an intermediate for production of methanol (used in chemical industry and possibly as shipping fuel) or kerosene (aviation fuel), while ethylene is used to make plastics such as polyethylene (PE).

Electrochemical CO_2 reduction (CO_2RR) works by the supply of CO_2 to the cathode of a water electrolysis cell to be reduced to products such as formate, carbon monoxide, methane, ethylene or ethanol. Water acts as the proton source for the reduction of CO_2, while at the anode water is oxidized to oxygen via the oxygen evolution reaction (OER). State-of-the-art catalysts currently have limitations, such as copper having low selectivity to produce ethylene or silver being an expensive catalyst for the production of carbon monoxide. Common methods to mitigate these issues include introducing a second metal

to form a bimetallic or using metal chalcogenides such as sulfides or oxides to increase selectivity. Examples include copper oxide for the production of ethanol, copper sulfide for the production of formate, and copper zinc for the production of carbon monoxide.

As two-element catalysts reach the saturation of their abilities, having three elements may be advantageous to push the boundaries of catalyst performance. This thesis focuses on Cu-M-S/Se as possible three-element catalysts to achieve selective CO_2 reduction, preferably to CO or even reduced products. In the first work, copper-metal-sulfides (where the metal can be In, Sn, Sb, Bi, Ga, Ge, Ag, Co, Fe) are investigated. It is found that Cu-Sb-S is the best performing catalyst for electrochemical CO_2 reduction to carbon monoxide. In the second work, it is revealed that Cu-Sb-S reduces when electricity is applied to sulfur-doped Cu-Sb where the sulfur acts to disrupt the crystal regularity and improve performance. In the third work, comparison is then made between Cu-Sb-S, Cu-Bi-S and two intermediate Cu-Sb/Bi-S samples where it is revealed that the second metal is crucial for selectivity to formate or carbon monoxide, and this may partly be due to the better ability of Sb to alloy with Cu compared to Bi which modifies the selectivity to carbon monoxide, as well as partly due to Bi loss resulting in excess Cu tuning the catalyst back to formate.

Acknowledgements

This 5 year journey to a PhD degree has been the hardest of any education period in my life, and it is a relief that I can now submit this thesis. I hope the thesis is an interesting read, especially Chapter 5 and the accompanying paper which took most of the time. I am so grateful it is published now, but there were times in the middle of it which I thought it would not get published. Thank you so much to the people and funding who have contributed to this project.

I would like to acknowledge the NTU Research Scholarship for funding my PhD, as well as the MOE Tier 1 funding (RG68/21) for support for this project.

I would like to thank first and foremost my main supervisor Prof Lydia Helena Wong. She was the one that introduced me to this field of electrochemical CO_2 reduction and to my co-supervisor, applied for and provided the funding for this project and provided the machinery in Solar Fuels Lab for the experimental work. Thank you for the patience, faith and encouragement in me, even when experiments and things did not go well. Thank you also for the resources mentioned that were crucial for the completion of this thesis.

I would also like to thank my co-supervisor, Prof Yanwei Lum. He kindly provided me with access to his labs at A*STAR IMRE, taught me the expertise for how to operate the electrochemical CO_2 cell, guided me through collecting the data for Chapter 5 and the paper, and also for introducing me to the people at A*STAR who would go on to guide me through the rest of my PhD. Thank you for being the expertise behind the work in this thesis as well as access to your A*STAR labs which was also crucial for this thesis.

Thank you to my mentors at A*STAR Dr Albertus Denny Handoko and Dr Ying Chuan Tan. They were the ones who provided me with the day-to-day guidance on electrochemical CO_2 reduction and how to solve experimental or other issues as well as edited my manuscript for Chapter 5. Thank you for all your help and your time even when

you were busy to contribute to the work in this thesis as well as the chats and meals at A*STAR.

I would also like to thank the people I worked closely with, Zheng Hao Tan, Surani bin Dolmanan, Dr Ying Fan Tay, Dr Meltem Yilmaz, Dr Joel Tan, Dr Mengyuan Zhang, Dr Mahmoud Ahmed, Dr Cai Jing and Dr Roong Jien Wong. These were the people

- I had talks and lunches with (I miss the ones at A*STAR with the lunch coordination gang! Zheng Hao, Ying Fan, Ying Chuan)
- I received guidance from through group meeting presentations (Surani, Ying Fan, Mahmoud)
- taught me how to do heat-up and solvothermal synthesis (Joel)
- taught me how to do NMR (Zheng Hao, Meltem)
- set up the A*STAR equipment (Ying Fan, Surani)
- helped to check my thesis (Mahmoud)
- collected CO2 reduction results with me in solar fuels lab (Cai Jing)
- guided me in setting up my lab equipment in the starting days of my PhD (Mengyuan)
- invited me to his lab to learn from him regarding gas chromatography (GC) as well as came on some occasions to guide me in GC matters (Roong Jien)

Thank you for making my PhD life fun and enriching and teaching me in the ways that you did.

I also thank the TAC members Prof Alex Yan and Prof Xue Can for their advice for this project.

Thank you also to my family, my fiancée and my friends for your encouragement and support.

Table of Contents

Table of Contents

Table Captions

Figure Captions

Abbreviations

CO_2RR	CO_2 Reduction Reaction
CV	Cyclic Voltammetry
DFT	Density Functional Theory
ECSA	ElectroChemically active Surface Area
EDX	Energy Dispersive X-ray spectroscopy
EIS	Electrochemical Impedance Spectroscopy
FE	Faradaic Efficiency
GC	Gas Chromatograph
GDE	Gas Diffusion Electrode
HER	Hydrogen Evolution Reaction
(HP)LC	(High-Performance) Liquid Chromatograph
ICP	Inductively Coupled Plasma
LSV	Linear Sweep Voltammetry
NMR	Nuclear Magnetic Resonance
OER	Oxygen Evolution Reaction
PCET	Proton-Coupled Electron Transfer
RDS	Rate Determining Step
RHE	Reversible Hydrogen Electrode
SEM	Scanning Electron Microscopy
SHE	Standard Hydrogen Electrode
TEM	Transmission Electron Microscopy
XPS	X-ray Photoelectron Spectroscopy
XRD	X-Ray Diffraction

Chapter 1 Introduction

This chapter presents an overview of the renewable energy transition. Then an introduction to the field of electrocatalysis and CO_2 reduction is made. This section covers the two-element catalysts (bimetallics, metal chalcogenides) in the field so far. The hypothesis and objectives of this study are then elucidated, which includes investigating bimetallic sulfides as three-element catalysts for better control of catalyst performance. The chapter concludes with a section on findings and originality of the study.

1.1 Hypothesis/Problem Statement

1.1.1 Background

The world is currently in the midst of a renewable energy transition, with a view on curbing anthropogenic climate change. Humanity is on track to miss the target of keeping warming within 1.5°C and more drastic action is needed to prevent catastrophic warming. Concurrent with a shift in electricity generation from fossil fuels to renewable energy is the switching of end uses of energy from fossil fuels to either electricity (electrification) or to renewable fuels and chemicals.[1]

Electrocatalysis, by utilizing electrical energy to convert water, CO_2 or nitrogen, is pivotal in the production of renewable fuels and chemicals, such as hydrogen, hydrocarbons, and ammonia.[2-4] In particular, the electrochemical CO_2 reduction reaction (CO_2RR) stands out for its potential to yield valuable feedstocks like ethylene, critical for the plastics industry. It can also produce a key intermediate, carbon monoxide (CO), which can then be used for the production of useful products such as methanol which is an important feedstock in the chemical industry, or the Fischer-Tropsch process to produce kerosene which can be used as sustainable aviation fuel.[3, 5]

The electrochemical CO_2 electrolyzer features two reactions, the electrochemical reduction of CO_2 (CO_2RR) takes place at the cathode, while the oxygen evolution reaction (OER) takes place at the anode (more details discussed in Chapters 2 and 3). Electricity, in particular voltage, is the driving force behind the chemical reaction. However, because of the use of abundant water as electrolyte, the hydrogen evolution reaction (HER) is always a competing reaction with CO_2RR on the cathode side. Thus, a suitable catalyst is necessary to suppress the competing HER reaction and selectively produce one CO_2RR product over other side products (high Faradaic efficiency).

	C-bound	O-bound
2e	CO	HCOOH
Reduced	CH_4 C_2H_4 C_2H_5OH	

Figure 1.1: Major CO_2RR products

Electrochemical CO_2 reduction on metals form five major products (Figure 1.1).[6] Such products consist of two-electron products such as formic acid/formate ($HCOOH/HCOO^-$) and carbon monoxide (CO) as well as reduced products such as methane (CH_4) ethylene (C_2H_4) or ethanol (C_2H_5OH). These products have different binding configurations, with the intermediates for formic acid binding to the catalyst via the oxygen atom(s) and the intermediates for the other products binding to the catalyst via the carbon atom(s).[6]

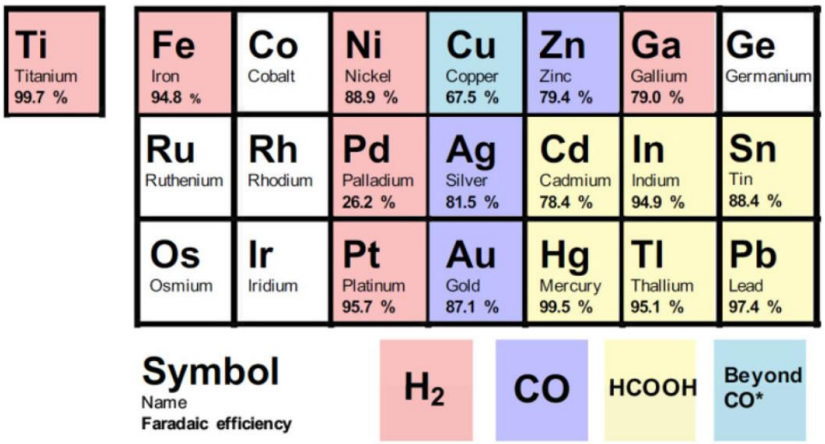

Figure 1.2: Main CO_2RR product according to element. Reproduced with permission from [7]

The metallic catalysts can be broadly classified into 4 categories based on its main products (Figure 1.2): $HCOO^-$-selective metals (main group elements such as Sn, In and Pb), CO-selective metals (Ag, Au and Zn), reduced products-selective metal (Cu only) and hydrogen-selective metals (transition metals in columns to the left of Cu).[7] For two-electron products, tin (Sn) and silver (Ag) are the benchmark catalysts for $HCOO^-$ and CO respectively, achieving near-unity Faradaic efficiency. However, silver is expensive and it

is difficult for copper to produce any individual reduced product with Faradaic efficiencies exceeding 60% due to similar energetics for the reduced products (CH_4, C_2H_4, C_2H_5OH). Thus, the main thrusts of current research in CO_2RR are (1) to find cheaper alternative catalysts to expensive Ag for the reduction of CO_2 to CO and (2) to improve the selectivity of Cu-based catalysts for the reduction of CO_2 to a particular reduced product.

Given the limitations (cost, selectivity, etc) of single element catalysts, catalysts with two or more elements are currently under investigation in the scientific community as cheap alternatives to Ag or to improve on the selectivity of Cu. Bimetallics and chalcogen-derived catalysts are two categories which have been investigated and are elaborated in the subsections below. In this study, sulfide-derived bimetallics are investigated to understand the dual effects of bimetallics as well as sulfide on selectivity.

1.1.2 Cu bimetallic alloys

Bimetallic alloys are of interest because of the ability to tune the binding energy of the surface to improve selectivity. The interaction of second metal with Cu, forming bimetallic alloys, has shown enhanced selectivity of Cu towards certain products. The selectivity of bimetallic Cu-based catalyst is highly dependent on the second metal. The selectivity trends are correlated with the type of phase and interaction formed between Cu and the second metal as follows:[8]

Solid solutions (Cu-Pd, Cu-Au, Cu-Zn) are able to form a continuum of stable compositions providing a means to finely tune the properties of bimetallic catalysts. Small amounts of these alloying elements can increase the selectivity of Cu to reduced products.[9-11] However, Au and Zn are themselves active sites for electrochemical CO_2 reduction to CO. Consequently, Au/Zn-heavy compositions will steer the selectivity towards CO.[12, 13]

Intermetallic compounds (Cu-In, Cu-Sn and Cu-Sb) form at discrete compositions. This means they are likely to phase segregate at intermediate compositions, making their product distribution an average of the individual phases and thus less tunable. All three

intermetallics are known to produce CO where the active site responsible is primarily Cu.[14-16] However, In, Sn and Sb are themselves more capable of producing $HCOO^-$ which binds to the metal via oxygen rather than carbon. Consequently, In/Sn/Sb-heavy compositions will steer the selectivity towards $HCOO^-$.[17-19]

1.1.3 Chalcogenide-derived catalysts

Oxide- and sulfide-derived (as well as selenide-derived) materials are also of interest as they impart different product selectivity behaviour compared to bare metallic catalysts. Notably, copper has different selectivities when it is derived from copper oxide or copper sulfide. Oxide-derived Cu shows an increased formation of ethanol, which has been attributed to the formation of extra grain boundaries.[20] Sulfide-derived Cu shows a different behaviour with increased $HCOO^-$ selectivity at the expense of CO and reduced products,[21] which has been attributed to the residual sulfur tuning the binding energies of the reaction intermediates although the exact mechanism is disputed.[22, 23] Selenide-derived Cu shows a similar behaviour as sulfide-derived Cu, but with more CO and H_2 and less $HCOO^-$.[22] Thus, research to more conclusively explain the effect of chalcogen and particularly sulfur in CO_2 reduction is needs to be done.

In a very small minority of cases, sulfide-derived catalysts do not produce $HCOO^-$ as the main product. The main exception is CdS, which produces CO as the main product as reported by He et al.[24] They also explored CdSe, but it produced mainly H_2 instead of CO.[24] Cd on its own also produces CO in some amount but with smaller Faradaic efficiency, showing that a good strategy may be to start with a metal catalyst that produces CO and then using its sulfide to improve the CO selectivity for CO_2RR. Combining the effect of second metal and S with Cu, the selectivity for CO_2RR on Cu-M-S catalysts can be synergistically tuned to produce CO with high Faradaic efficiency, hence this study.

One key issue in chalcogenides is whether they reduce under an applied potential. When the applied potential is more positive than the standard reduction potential, the sulfides are unaffected. However, when the applied potential is more negative than their standard reduction potential, the sulfides are thermodynamically unstable under the applied

potential.[25-27] Thus, the catalyst might undergo a reconstruction process to form the active phase for CO_2RR. This active phase (or chalcogenide-derived phase) should then be determined by post-catalysis characterization.

1.1.4 Hypothesis and design target

The hypothesis is that ternary catalysts, of which Cu-M sulfide-derived or selenide-derived catalysts are considered, will be able to improve the selectivity of the catalyst over binary catalysts mentioned above. This study explores the role of combining Cu with another metal (such as In, Sn, Sb, Bi, Ga, Ge, Ag, Co, Fe) in sulfides and looking at the product selectivity trends (such as $HCOO^-$, CO and reduced products). The role of second metal in tuning, as well as the role of sulfur in either parent sulfide or reduced forms, will be elucidated. The hypotheses of this thesis are:

1. **Cu-M-S (M=In, Sn, Sb, Bi) will be active for electrochemical CO_2 reduction.** As Cu is the key metal that produces CO in most Cu-M alloys, if post-transition metals are alloyed with Cu, sulfur may improve their selectivity. For example, Gregoire group's study indicates that Cu-M (where M=In, Sn and Sb) bimetallic produces CO, which indicates that the bimetallic as a whole binds loosely to CO which allows it to leave.[28] On the other hand, Cu-Bi produces $HCOO^-$.[29] It is predicted that these combinations of second metal (M=In, Sn, Sb, Bi) with Cu and S will be more active for electrochemical CO_2 reduction than the other combinations (M=Ga, Ge, Ag, Co, Fe) which will produce mainly H_2.
2. **Interaction of chalcogen with metals can improve selectivity of CO if reduced or improve HCOOH if unreduced.** This is because the mechanisms for CO and $HCOO^-$, which sulfur or selenium can modify, are different. Sulfide-derived and selenide-derived catalysts have shown a tendency to produce either $HCOO^-$ or H_2. This behaviour may be attributed to a hypothesized mechanism where sulfur or selenium binds *H (S-H or Se-H), which can then react with an incoming hydrogen atom to form H_2 or an incoming CO_2 molecule to form $HCOO^-$ according to Abild-Pedersen and co-workers.[30] Sulfur (and possibly also selenium) also has the potential to promote CO through a covalency-aided mechanism according to Kim et al, but this mechanism

relies on having only a minute doping of sulfur.[31] The *H bound mechanism may be dominant when the parent chalcogenide does not reduce,[32] while the covalency-aided mechanism may be dominant if it reduces. Whether the parent chalcogenide reduces depends on the standard reduction potentials of Cu and M metals.

3. **Cu-Sb-S will be the best candidate for electrochemical CO_2 reduction to CO.** From Gregoire's list of In, Sn and Sb, standard reduction potentials for In^{3+}, Sn^{4+} and SbO^{+} (as Sb^{3+} data is unavailable) are compared.[33] The values are -0.338, 0.021 and 0.2. Thus, Sb is the most susceptible to reduction. As mentioned in the previous hypothesis, for S to improve CO selectivity, the parent sulfide has to reduce to provide minute doping of sulfur. Thus, Cu-Sb-S will be the ideal candidate for electrochemical CO_2 reduction to CO.
4. **Varying the ratio between Sb on one hand and Bi on the other in Cu-(Sb, Bi)-S may tune the selectivity between CO and** $HCOO^-$ **respectively.** This also may shed light on the competing effects between Cu (which prefers CO) and main group element (which prefers $HCOO^-$). If the relationship is non-linear, there could be a possibility to improve the selectivity of the catalyst to either CO or $HCOO^-$.

1.2 Objectives and Scope

This study will explore the role of the second metal M (where M is In, Sn, Sb, Bi, Ga, Ge, Ag, Co, Fe) and sulfur in the Cu-M-S system on the product selectivity in electrochemical CO_2 reduction.

1. **Screening whole series of Cu-M-S (where M is In, Sn, Sb, Bi, Ag, Ga, Ge, Co, Fe) catalysts to identify catalysts with high CO selectivity. Comparing the resulting promising catalysts with selenium replacing sulfur.** This study will correlate reduction behaviour of sulfide and metal species to observed CO_2RR products. The study will also identify promising catalysts for the subsequent studies.
2. **Investigating and characterizing multiple Cu-Sb-S nanoparticle phases including post-reduction characterization.** Different phases of Cu-Sb-S nanoparticles are synthesized, tested for CO_2 reduction and investigated by various bulk and surface characterizations.

3. **Investigating tunable Cu-Sb/Bi-S catalysts with varying Sb:Bi ratios.** This is to further understand the effect of second metal species on the CO_2RR performance as well as reduction behaviour.

1.3 Dissertation overview

This thesis investigates the category of Cu-M-S/Se chalcogenide-derived bimetallic catalysts for electrochemical CO_2 reduction and correlates the CO_2 reduction products with catalyst composition and reduction behaviour. This study seeks to understand how the choice of second metal and the chalcogen type (S, Se) affects the catalytic activity as well as how easily the parent sulfide/selenide reduces when a voltage is applied. The phase and crystallinity of the catalyst after CO_2 reduction is linked to the type of CO_2RR product (CO, $HCOO^-$ or competing H_2) and insights are drawn on how to design catalysts that favour CO or $HCOO^-$.

The thesis is structured as follows:

Chapter 1 introduces the rationale, design and objective of the study in investigating Cu-M-S/Se catalysts for electrochemical CO_2 reduction.

Chapter 2 reviews the literature concerning the basics of electrochemical figures of merit, electrochemical CO_2 reduction, reaction mechanism and thermodynamics, types of catalysts and their selectivity.

Chapter 3 discusses the synthesis methods for catalysts, electrochemical CO_2 reduction measurement techniques and principles behind characterization techniques used to understand the catalysts.

Chapter 4 elaborates on the synthesis, electrochemical CO_2 reduction behaviour and characterization of Cu-M-S (M=In, Sn, Sb, Bi, Ga, Ge, Ag, Co, Fe). The behaviour of these catalysts fall into two groups, with (M=In, Sn, Sb, Bi) being active for electrochemical CO_2

reduction and (M=Ga, Ge, Ag, Co, Fe) mainly producing H_2. Cu-Sb-S is singled out for its ability to produce CO and Cu-Sb-S/Se is tested to compare S vs Se performance.

Chapter 5 elaborates on the synthesis, electrochemical CO_2 reduction performance and characterization of three phases of Cu-Sb-S: skinnerite (SK, Cu_3SbS_3), tetrahedrite (TH, $Cu_{12}Sb_4S_{13}$) and chalcostibite (CS, $CuSbS_2$). It is found that the catalyst reduces in all three phases but the reduced phases have different degrees of crystallinity and phase composition that result in different CO selectivity, with TH as the best performing catalyst with ~80% FE for CO.

Chapter 6 elaborates on the synthesis, electrochemical CO_2 reduction performance and characterization of $Cu_3(Sb_xBi_{1-x})S_3$ with four compositions: x=1, 0.66, 0.33, 0. It is found that Sb content is correlated with CO selectivity and Bi content is correlated with $HCOO^-$ selectivity. It is also found that Bi loss is more extensive than Sb loss, and when considered together with the production of a small amount of reduced products up to 2%, suggests that Bi is harder to alloy compared to Sb.

Chapter 7 summarizes the findings of this work. The bimetallic strategy is robust and trimetallic catalysts are recommended for further study to optimize reaction intermediate binding for more desirable products.

1.4 Findings and Outcomes/Originality

This research led to several novel outcomes:

1. Revealing selectivity trends in the Cu-M-S materials space with nine metals which combine with Cu in sulfides (M=In, Sn, Sb, Bi, Ga, Ge, Ag, Co, Fe). Specifically, heavier main group metals (M=In, Sn, Sb, Bi) can alloy with Cu for electrochemical CO_2 reduction to CO or $HCOO^-$, while the other metals (M=Ga, Ge, Ag, Co, Fe) produce H_2.

2. Revealing the changes in selectivities and reaction mechanism when Cu-Sb-S/Se is used where selenium is added to the synthesis. Selenium is shown to promote H_2, likely due to synergistically working with Sb to bind *H.
3. Achieving the first reported sulfide-derived copper-based catalyst that can selectively produce CO (i.e. Cu-Sb-S-derived catalyst)). The TH catalyst produced CO with a maximum Faradaic efficiency of 80%.
4. Investigating the interaction between copper and second metal by varying the ratio between Sb and Bi. In sulfide-derived Cu-Sb, CO is the main product, while for sulfide-derived Cu-Bi, $HCOO^-$ is the main product. A correlation is drawn between Sb content and CO production, as well as Bi content and $HCOO^-$ production.

References

[1] Z. J. Schiffer and K. Manthiram, "Electrification and Decarbonization of the Chemical Industry," *Joule,* vol. 1, no. 1, pp. 10-14, 2017/09/06/ 2017, doi: https://doi.org/10.1016/j.joule.2017.07.008.

[2] J. Zhu, L. Hu, P. Zhao, L. Y. S. Lee, and K.-Y. Wong, "Recent Advances in Electrocatalytic Hydrogen Evolution Using Nanoparticles," *Chemical Reviews,* vol. 120, no. 2, pp. 851-918, 2020/01/22 2020, doi: 10.1021/acs.chemrev.9b00248.

[3] S. Nitopi *et al.*, "Progress and Perspectives of Electrochemical CO2 Reduction on Copper in Aqueous Electrolyte," *Chemical Reviews,* vol. 119, no. 12, pp. 7610-7672, 2019/06/26 2019, doi: 10.1021/acs.chemrev.8b00705.

[4] M. A. Shipman and M. D. Symes, "Recent progress towards the electrosynthesis of ammonia from sustainable resources," *Catalysis Today,* vol. 286, pp. 57-68, 2017/05/15/ 2017, doi: https://doi.org/10.1016/j.cattod.2016.05.008.

[5] X. Jiang, X. Nie, X. Guo, C. Song, and J. G. Chen, "Recent Advances in Carbon Dioxide Hydrogenation to Methanol via Heterogeneous Catalysis," *Chemical Reviews,* vol. 120, no. 15, pp. 7984-8034, 2020/08/12 2020, doi: 10.1021/acs.chemrev.9b00723.

[6] R. Kortlever, J. Shen, K. J. P. Schouten, F. Calle-Vallejo, and M. T. M. Koper, "Catalysts and Reaction Pathways for the Electrochemical Reduction of Carbon Dioxide," *The Journal of Physical Chemistry Letters,* vol. 6, no. 20, pp. 4073-4082, 2015/10/15 2015, doi: 10.1021/acs.jpclett.5b01559.

[7] A. Bagger, W. Ju, A. S. Varela, P. Strasser, and J. Rossmeisl, "Electrochemical CO2 Reduction: A Classification Problem," *ChemPhysChem,* vol. 18, no. 22, pp. 3266-3273, 2017, doi: https://doi.org/10.1002/cphc.201700736.

[8] C. W. Lee *et al.*, "Defining a Materials Database for the Design of Copper Binary Alloy Catalysts for Electrochemical CO2 Conversion," *Advanced Materials,* vol. 30, no. 42, p. 1704717, 2018, doi: https://doi.org/10.1002/adma.201704717.

[9] J.-F. Xie *et al.*, "Selective electrochemical CO2 reduction on Cu-Pd heterostructure," *Applied Catalysis B: Environmental,* vol. 270, p. 118864, 2020/08/05/ 2020, doi: https://doi.org/10.1016/j.apcatb.2020.118864.

[10] X. Wang *et al.*, "Gold-in-copper at low *CO coverage enables efficient electromethanation of CO2," *Nature Communications,* vol. 12, no. 1, p. 3387, 2021/06/07 2021, doi: 10.1038/s41467-021-23699-4.

[11] D. Ren, B. S.-H. Ang, and B. S. Yeo, "Tuning the Selectivity of Carbon Dioxide Electroreduction toward Ethanol on Oxide-Derived CuxZn Catalysts," *ACS Catalysis,* vol. 6, no. 12, pp. 8239-8247, 2016/12/02 2016, doi: 10.1021/acscatal.6b02162.

[12] D. Kim, J. Resasco, Y. Yu, A. M. Asiri, and P. Yang, "Synergistic geometric and electronic effects for electrochemical reduction of carbon dioxide using gold–copper bimetallic nanoparticles," *Nature Communications,* vol. 5, no. 1, p. 4948, 2014/09/11 2014, doi: 10.1038/ncomms5948.

[13] L. Wang *et al.*, "Bimetallic effects on Zn-Cu electrocatalysts enhance activity and selectivity for the conversion of CO2 to CO," *Chem Catalysis,* vol. 1, no. 3, pp. 663-680, 2021/08/19/ 2021, doi: https://doi.org/10.1016/j.checat.2021.05.006.

[14] S. Rasul, D. H. Anjum, A. Jedidi, Y. Minenkov, L. Cavallo, and K. Takanabe, "A Highly Selective Copper–Indium Bimetallic Electrocatalyst for the Electrochemical Reduction of Aqueous CO2 to CO," *Angewandte Chemie International Edition,* vol. 54, no. 7, pp. 2146-2150, 2015, doi: https://doi.org/10.1002/anie.201410233.

[15] S. Sarfraz, A. T. Garcia-Esparza, A. Jedidi, L. Cavallo, and K. Takanabe, "Cu–Sn Bimetallic Catalyst for Selective Aqueous Electroreduction of CO2 to CO," *ACS Catalysis,* vol. 6, no. 5, pp. 2842-2851, 2016/05/06 2016, doi: 10.1021/acscatal.6b00269.

[16] S. Mou *et al.*, "Cu2Sb decorated Cu nanowire arrays for selective electrocatalytic CO2 to CO conversion," *Nano Research,* vol. 14, no. 8, pp. 2831-2836, 2021/08/01 2021, doi: 10.1007/s12274-021-3295-1.

[17] Q. Xie, G. O. Larrazábal, M. Ma, I. Chorkendorff, B. Seger, and J. Luo, "Copper-indium hydroxides derived electrocatalysts with tunable compositions for electrochemical CO2 reduction," *Journal of Energy Chemistry,* vol. 63, pp. 278-284, 2021/12/01/ 2021, doi: https://doi.org/10.1016/j.jechem.2021.09.008.

[18] M. Zhang *et al.*, "Tunable Selectivity for Electrochemical CO2 Reduction by Bimetallic Cu–Sn Catalysts: Elucidating the Roles of Cu and Sn," *ACS Catalysis,* vol. 11, no. 17, pp. 11103-11108, 2021/09/03 2021, doi: 10.1021/acscatal.1c02556.

[19] G. A. El-Nagar *et al.*, "Comparative Spectroscopic Study Revealing Why the CO2 Electroreduction Selectivity Switches from CO to HCOO– at Cu–Sn- and Cu–In-Based Catalysts," *ACS Catalysis,* vol. 12, no. 24, pp. 15576-15589, 2022/12/16 2022, doi: 10.1021/acscatal.2c04419.

[20] C. W. Li, J. Ciston, and M. W. Kanan, "Electroreduction of carbon monoxide to liquid fuel on oxide-derived nanocrystalline copper," *Nature,* vol. 508, no. 7497, pp. 504-507, 2014/04/01 2014, doi: 10.1038/nature13249.

[21] T. Shinagawa, G. O. Larrazábal, A. J. Martín, F. Krumeich, and J. Pérez-Ramírez, "Sulfur-Modified Copper Catalysts for the Electrochemical Reduction of Carbon Dioxide to Formate," *ACS Catalysis,* vol. 8, no. 2, pp. 837-844, 2018/02/02 2018, doi: 10.1021/acscatal.7b03161.

[22] R. García-Muelas, F. Dattila, T. Shinagawa, A. J. Martín, J. Pérez-Ramírez, and N. López, "Origin of the Selective Electroreduction of Carbon Dioxide to Formate by Chalcogen Modified Copper," *The Journal of Physical Chemistry Letters,* vol. 9, no. 24, pp. 7153-7159, 2018/12/20 2018, doi: 10.1021/acs.jpclett.8b03212.

[23] K. R. Phillips, Y. Katayama, J. Hwang, and Y. Shao-Horn, "Sulfide-Derived Copper for Electrochemical Conversion of CO2 to Formic Acid," *The Journal of Physical Chemistry Letters,* vol. 9, no. 15, pp. 4407-4412, 2018/08/02 2018, doi: 10.1021/acs.jpclett.8b01601.

[24] R. He *et al.*, "Achieving the Widest Range of Syngas Proportions at High Current Density over Cadmium Sulfoselenide Nanorods in CO2 Electroreduction," *Advanced Materials,* vol. 30, no. 7, p. 1705872, 2018, doi: https://doi.org/10.1002/adma.201705872.

[25] S. Licht, "Aqueous Solubilities, Solubility Products and Standard Oxidation‐Reduction Potentials of the Metal Sulfides," *Journal of The Electrochemical Society,* vol. 135, no. 12, p. 2971, 1988/12/01 1988, doi: 10.1149/1.2095471.

[26] N. Elgrishi, K. J. Rountree, B. D. McCarthy, E. S. Rountree, T. T. Eisenhart, and J. L. Dempsey, "A Practical Beginner's Guide to Cyclic Voltammetry," *Journal of Chemical Education,* vol. 95, no. 2, pp. 197-206, 2018/02/13 2018, doi: 10.1021/acs.jchemed.7b00361.

[27] H. Jiang, Q. He, Y. Zhang, and L. Song, "Structural Self-Reconstruction of Catalysts in Electrocatalysis," *Accounts of Chemical Research,* vol. 51, no. 11, pp. 2968-2977, 2018/11/20 2018, doi: 10.1021/acs.accounts.8b00449.

[28] Y. Lai, R. J. R. Jones, Y. Wang, L. Zhou, M. H. Richter, and J. Gregoire, "The sensitivity of Cu for electrochemical carbon dioxide reduction to hydrocarbons as revealed by high throughput experiments," *Journal of Materials Chemistry A,* 10.1039/C9TA10111J vol. 7, no. 47, pp. 26785-26790, 2019, doi: 10.1039/C9TA10111J.

[29] L. Jia *et al.*, "Copper-Bismuth Bimetallic Microspheres for Selective Electrocatalytic Reduction of CO2 to Formate," *Chinese Journal of Chemistry,* vol. 37, no. 5, pp. 497-500, 2019, doi: https://doi.org/10.1002/cjoc.201900010.

[30] M. T. Tang, H. Peng, P. S. Lamoureux, M. Bajdich, and F. Abild-Pedersen, "From electricity to fuels: Descriptors for C1 selectivity in electrochemical CO2 reduction," *Applied Catalysis B: Environmental,* vol. 279, p. 119384, 2020/12/15/ 2020, doi: https://doi.org/10.1016/j.apcatb.2020.119384.

[31] H.-K. Lim, H. Shin, W. A. Goddard, Y. J. Hwang, B. K. Min, and H. Kim, "Embedding Covalency into Metal Catalysts for Efficient Electrochemical Conversion of CO2," *Journal of the American Chemical Society,* vol. 136, no. 32, pp. 11355-11361, 2014/08/13 2014, doi: 10.1021/ja503782w.

[32] L.-P. Chi *et al.*, "Stabilizing indium sulfide for CO2 electroreduction to formate at high rate by zinc incorporation," *Nature Communications,* vol. 12, no. 1, p. 5835, 2021/10/05 2021, doi: 10.1038/s41467-021-26124-y.

[33] P. Vanysek, "Electrochemical series," *CRC handbook of chemistry and physics,* vol. 8, pp. 8-33, 2000.

Chapter 2 Literature Review

This chapter describes the basics and mechanism of electrochemical CO_2 reduction, the performance metrics used in evaluating CO_2 reduction catalysts, catalyst reconstruction, as well as the materials used as catalysts. Areas for study are then identified where research or understanding is lacking and where this study aims to focus.

2.1 Electrochemical CO_2 reduction

Electrochemical CO_2 reduction is typically carried out in a two- or three-compartment cell, as seen in Figure 2.1.

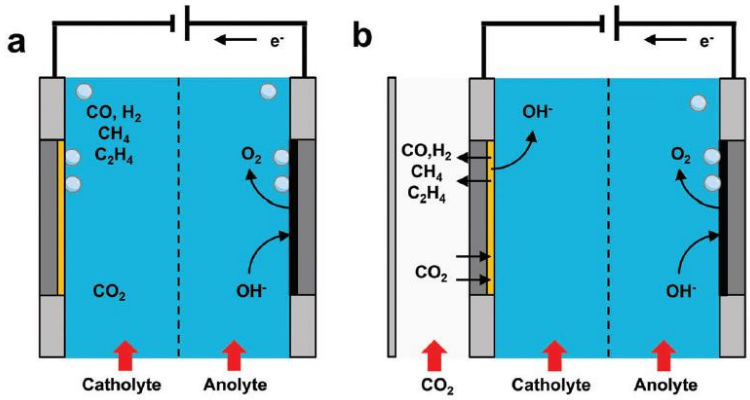

Figure 2.1: a) Two- or b) three-component CO_2RR flow cell[1]. The three compartments are the gas compartment (optional), the catholyte compartment and the anolyte compartment. *No permission is required for thesis purposes.*

On the cathode side, CO_2 is either saturated into the catholyte or introduced in gas phase to the catalyst, where the following half-reactions take place as shown in Table 2.1[2]:

Table 2.1: Reduction potentials of two-electron CO_2RR products

Half reaction	$E^0_{reduction}$ (V vs RHE)
$CO_2 + H^+ + 2e^- \rightarrow HCOO^-$	–0.12
$CO_2 + 2H^+ + 2e^- \rightarrow CO + H_2O$	–0.10

On Cu, the following reactions may take place with adsorbed CO, resulting in reduced products as shown in Table 2.2[2]:

Table 2.2: Reduction potentials of CO reduction to reduced products

Half reaction	$E^0_{reduction}$ (V vs RHE)
$CO + 6H^+ + 6e^- \rightarrow CH_4 + H_2O$	0.26
$2O + 8H^+ + 8e^- \rightarrow C_2H_4 + 2H_2O$	0.17
$2CO + 8H^+ + 8e^- \rightarrow C_2H_5H + H_2O$	0.19

On the anode side, the OER half-reaction takes place as shown in Table 2.3:

Table 2.3: Oxidation potential of OER

Half reaction	$E^0_{oxidation}$ (V vs RE)
$2H_2O \rightarrow O_2 + 4H^+ + 4e^-$	1.23

The minimum energy required to drive the full cell reaction is simply the addition of the cathode and anode side reactions:

$$E^0{}_{cell} = E^0{}_{reduction} + E^0{}_{oxidation}$$

However, on actual catalysts the potential needed to drive either half reaction is larger than the thermodynamic potentials due to the overpotential (η) required on the catalyst for all individual steps in the electrochemical reaction to be downhill. As a result, the potential applied at the cathode for CO_2RR can be expressed as:

$$E_{cathode} = E^0{}_{reduction} + \eta_{reduction}$$

2.2 Figures of merit for CO_2RR

There are a few key performance indicators to assess, compare and judge different CO_2RR catalysts.[2] The common metrics used for such performance evaluations of CO_2RR catalysts are elaborated below.

2.2.1 Faradaic efficiency

The key challenge of CO_2RR is that multiple reaction products are formed on the catalyst and HER is always a competing reaction with H_2 as side product. As such, to measure the amount of desired product formed over the total amount of products formed, Faradaic efficiency is introduced. Faradaic efficiency is defined as the amount of charge used to form a particular product over the total amount of charge passed:[2]

$$FE = \frac{Q_{product}}{Q_{total}}$$

In flow cells, due to the continuous flow of gases, a common approximation (which is not exactly equivalent due to fluctuations in product distribution) is the instantaneous current used to form a particular product over the total instantaneous current:

$$FE = \frac{I_{product}}{I_{total}}$$

$Q_{product}$ or $I_{product}$ can be obtained from the concentrations of liquid product (as measured by high-performance liquid chromatography (HPLC) or nuclear magnetic resonance spectroscopy (NMR) or gaseous product (as measured by the GC), converted to number of moles of electrons going to the product. Q_{total} or I_{total} can be obtained as measured from the electrochemical workstation.

The benchmark catalysts in the field are widely regarded to be Sn for $HCOO^-$, Ag for CO and Cu for reduced products. Sn is able to produce $HCOO^-$ with a typical FE over 90%, while Ag is able to produce CO with a similar typical FE over 90%. For Cu, FEs for reduced products are typically lower due to the much wider spread of products being formed dependent on the exposed facets and structure of the copper.

2.2.2 Partial current density

This is the figure of merit to evaluate the reaction rate of a particular product with the given catalyst surface area. This is given by:

$$j_{product} = \frac{I_{product}}{surface\ area}$$

While the exact surface area to be used is the electrochemical surface area (ECSA), in practice the geometric surface area is commonly used due to its convenience. The proper ECSA is typically determined by double-layer capacitance measurements, hydrogen underpotential deposition measurements or integration of cyclic voltametric peaks.[2]

2.2.3 Onset potential

The onset potential is the minimum applied potential at which a given reaction product begins to be formed. This is when the product starts being detected by available detection devices such as chromatographs.

In practice however, this is limited by the sensitivity of the detection device (GC, HPLC, NMR, etc). Thus, a practical definition is along the lines of *the applied potential at which a given reaction product is formed with a specified current density*.[3]

2.2.4 Tafel slope

The overpotential η mentioned above is related to the current density (of a specific CO_2RR product) through the Butler-Volmer equation:[2, 4]

$$j = j_0(e^{-\alpha f\eta} - e^{(1-\alpha)f\eta})$$

where j_0 is the exchange current density, α is the symmetry factor, $f = \frac{nF}{RT}$ where n is number of electrons transferred, F is Faraday constant, R is the universal gas constant and T is the temperature. At large overpotentials, the reverse current term $e^{(1-\alpha)f\eta}$ can be neglected, and the Butler-Volmer equation reduces to the Tafel equation:[2, 4]

$$\eta = \frac{2.3RT}{\alpha f}\log(j_0) - \frac{2.3RT}{\alpha f}\log(j)$$

As can be seen, if η is plotted against log(j), $\frac{2.3RT}{\alpha f}$ is obtained as the Tafel slope. If η=0 is taken and the line is extrapolated to the x-axis, the exchange current j_0 is obtained. The Tafel slope gives information regarding the electrochemical steps of the reaction before the rate determining step.[2, 4] Thus, the Tafel slope is a key indicator of the energy required for the electrochemical reduction to occur. A smaller Tafel slope is better because a lower amount of additional energy is required to increase the current density by a given amount.

2.2.5 Stability

The stability of the catalyst refers to the length of time that the catalyst can maintain a high Faradaic efficiency and current density towards a particular CO_2RR product. Stability is an important parameter for commercial viability. This is usually tested by chronopotentiometry (constant current) or chronoamperometry (constant voltage) for a period of time. Generally, a catalyst can be considered stable if it retains a high Faradaic efficiency and partial current density for a particular product for 7-12 hours or more.[2]

2.3 Mechanism of CO_2 reduction reaction

Designing a CO_2RR catalyst to produce only one reaction product selectively requires a good understanding of the underlying mechanism involved in CO_2 reduction and why different catalysts prefer certain reduction products.

2.3.1 CO vs HCOOH/HCOO⁻

The first bifurcation in the generally accepted CO_2 reduction reaction separates the pathways that produce CO and HCOOH/HCOO⁻ (Figure 2.2).

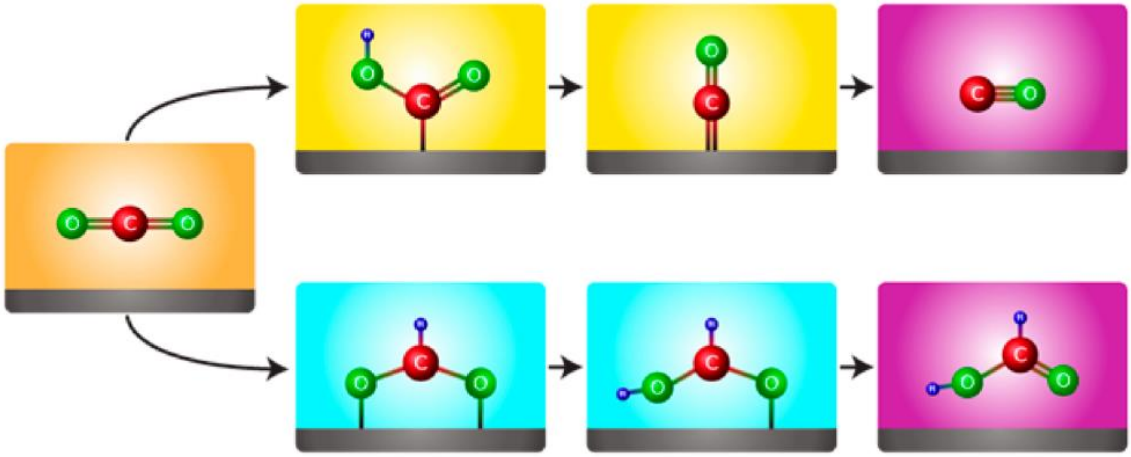

Figure 2.2: Reaction mechanism for CO_2 reduction to CO or HCOOH. Reprinted with permission from [5]. Copyright 2017 American Chemical Society.

To produce CO, the metal binds to the CO_2 molecule via the C atom while a proton and an electron are transferred to it, forming a bound *COOH intermediate where * represents the metal site. This intermediate then reacts further via a proton-coupled electron transfer (PCET) to produce bound *CO and a leaving H_2O molecule. The *CO then desorbs as CO. The most common proposed reaction mechanism in electrochemical CO_2 reduction to CO can be summarized as follows:[6, 7]

$$* + CO_2 + e^- \rightarrow * CO_2^-$$

$$* CO_2^- + H^+ \rightarrow * COOH$$

$$* COOH + H^+ + e^- \rightarrow * CO + H_2O$$

$$* CO \rightarrow * + CO$$

To produce HCOO⁻, the C atom must be protonated. For this to happen the metal binds with the CO_2 molecule via the O atom forming *OCHO after protonation. This intermediate then reacts further via an electron transfer to form *OCHO⁻. The *OCHO⁻ then desorbs as HCOO⁻. One possible reaction mechanism scheme (which is slightly

different from Figure 2.2) for electrochemical CO_2 reduction to $HCOO^-$ can be summarized as follows:[6, 7]

$$* + H^+ + e^- \rightarrow * H$$

$$* H + CO_2 \rightarrow * OCHO$$

$$* OCHO + e^- \rightarrow * OCHO^-$$

$$* OCHO^- \rightarrow * + HCOO^-$$

Given that metal atoms that bind C (or H, since *H and *CO scale linearly in a direct relationship)[8] optimally produce CO (or reduced products), while metal atoms that bind O optimally produce $HCOO^-$, metal atoms can be plotted with O binding on the y-axis and H-binding on the x-axis to form a map:[9]

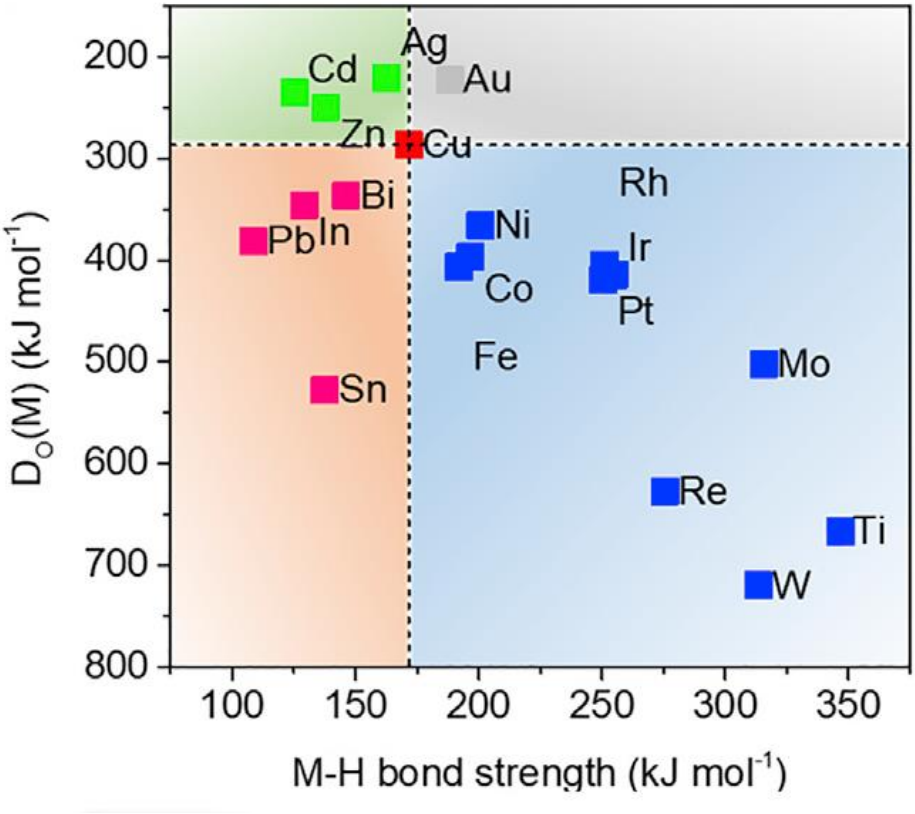

Figure 2.3: Intermediate M-H bond strength plotted against bond dissociation enthalpy of metal oxides. Reproduced with permission from [9]

As can be seen in Figure 2.3, there are four groups of metals:

- post-transition elements like In, Sn, Pb, Bi (that bind O strongly and C weakly)

- Group 11 and 12 transition elements like Ag, Au, Zn (that bind O weakly and C moderately)
- Cu (that binds O moderately and C moderately)
- Group 4 to 10 transition elements like Ni, Fe, Pt (that bind O strongly and C strongly)

As main group elements bind O strongly but C weakly, they produce $HCOO^-$ as their main product. Ag, Au and Zn bind O weakly but C moderately, thus they are able to produce CO as their main product. As Cu binds both O and C moderately, it can produce both CO and $HCOO^-$. Group 4 to 10 transition elements bind O strongly and C strongly, so theoretically they can produce both $HCOO^-$ and CO (which are indeed seen in Pd catalysts)[10], but most of these catalysts are inactive for CO_2 reduction due to CO catalyst poisoning as they have incomplete d-bands that can participate in pi backbonding with CO as shown below:

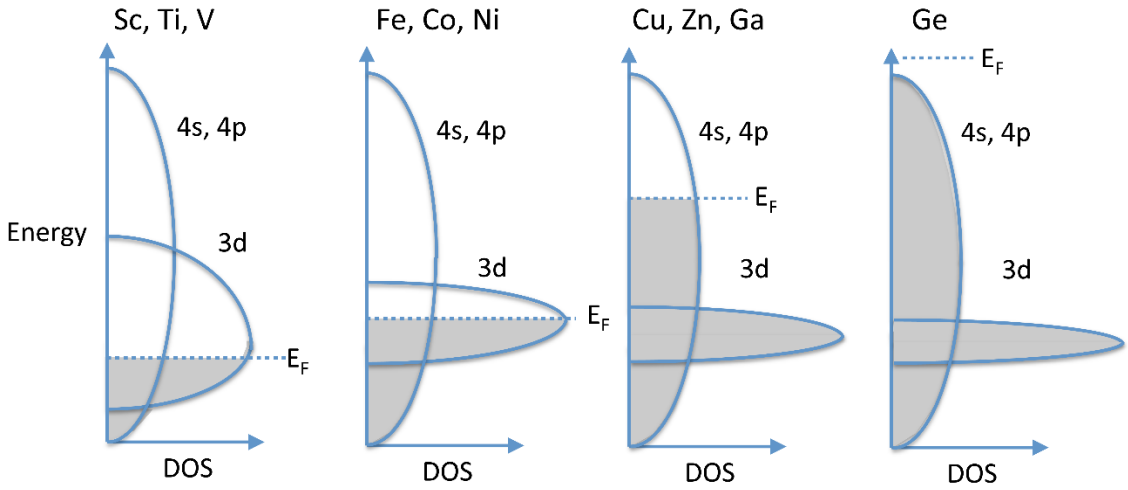

Figure 2.4: Schematic of 3d, 4s and 4p bands for metals Sc to Ge, taken from Wikipedia.

The d-band becomes fully filled only in Group 11 and beyond.[12] CO can be further reduced on Cu to form reduced products like methane, ethylene and ethanol, as detailed in the following section.

2.3.2 Reduced products on Cu (CH_4, C_2H_4 and C_2H_5OH)

The second bifurcation largely happens only on copper, and is whether the adsorbed *CO intermediate prefers to:

- Case 1: react further with more PCET steps to CH_4

- Case 2: dimerize to form a C-C bond and react further with more PCET steps to C_2H_4, C_2H_5OH or other minor products

To understand why copper is ideal, the volcano plot of the key intermediate steps is plotted in Figures 2.5 and 2.6. The rate-determining step of CO_2 to CO is likely to be the CO_2 to *COOH reaction which forms the right side of the volcano plot in Figures 2.5 and 2.6. The rate-determining step for the CO to CH_4 reaction is likely to be the *CO to *CHO reaction (Figure 2.5), and the rate-determining step for the 2CO to C_2H_4 or C_2H_5OH reaction is likely to be the 2*CO to *COCOH reaction (Figure 2.6). These two reactions form the left side of their respective volcano plots.

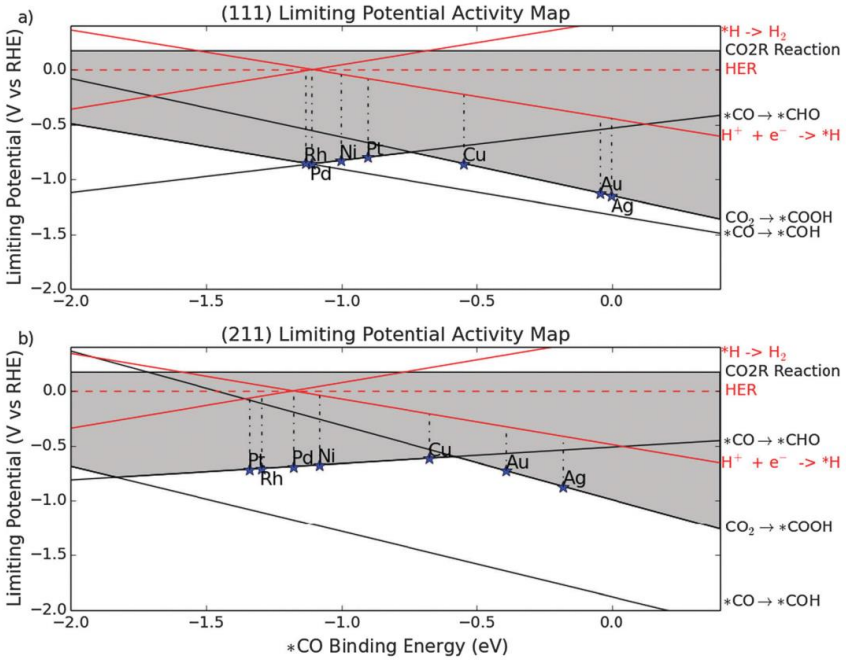

Figure 2.5: Volcano plots for CO_2 reduction to CH_4 on metal surfaces. Reproduced with permission from [8]

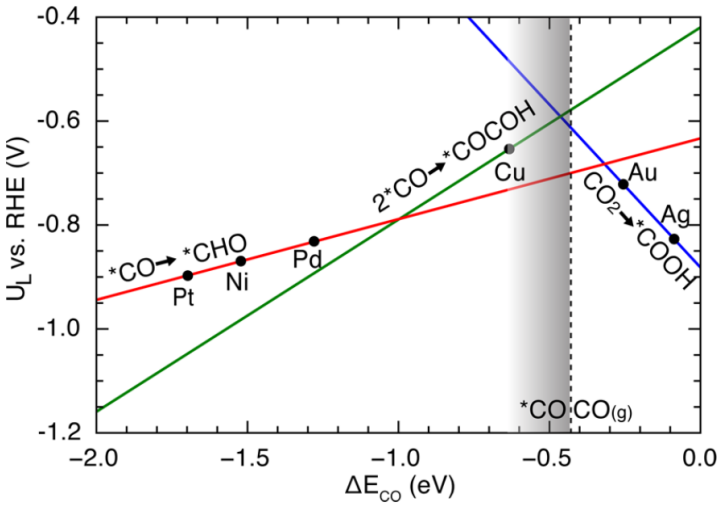

Figure 2.6: Volcano plot for CO_2 reduction to C_1 and C_2 species on metal surfaces. Reprinted with permission from [11]. Copyright 2015 American Chemical Society.

As can be seen in Figures 2.5 and 2.6, the metal closest to the peak of the volcano plots is Cu, indicating that Cu has optimal binding energy for the reduction of CO to reduced products in general. Au and Ag bind CO too weakly and thus CO prefers to desorb, while other transition metals such as Ni, Pt or Pd bind CO too strongly resulting in catalyst poisoning.

For Cu, it appears that surface facet heavily affects the selectivity between CH_4 on one hand (case 1) and C_2 products on the other (case 2, which leads to C_2H_4 and C_2H_5OH). Initial experiments by Hori et al showed that Cu(111) was selective towards methane and Cu(100) was selective towards ethylene.[12] This was later also verified by others such as Huang et al.[13] The selectivity differences between methane and ethylene was investigated computationally by Asthigiri's group, Goddard's group and Norskov's group,[14-18] where the difference was attributed to the low CO-CO dimerization barrier on Cu(100) facet favouring C_2H_4 and the low protonation barrier on Cu(111) facet favouring CH_4.

Also for Cu, the selectivity between C_2 products C_2H_4 on one hand and C_2H_5OH on the other is primarily affected by the surface population of *CO. Reports on Cu-Zn catalysts by Ren et al and Baek et al show that formulations in the range of Cu_2Zn_1 to Cu_4Zn_1 are

able to produce increased ethanol/ethylene ratios in the range of 6-9, with the Faradaic efficiency (FE) of ethanol in the range of 25-30%.[19, 20] The increased ethanol production with respect to ethylene has been attributed to the local increase in *CO due to Zn sites catalysing CO which are then available for further reduction on Cu sites.

Thus, while CH_4, C_2H_4 and C_2H_5OH are simultaneously produced on Cu, the nanostructures and exposed facets, as well as the local availability of *CO from other catalyst sites, can tune Cu towards more selective production of specific reduced products.

2.3.3 Thermodynamics of electrocatalysis and Gibbs free energy

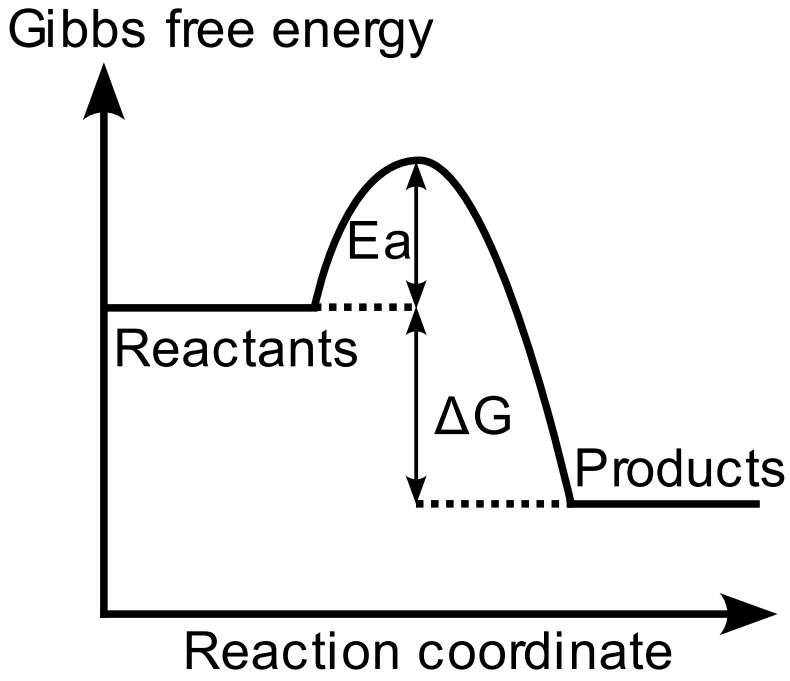

Figure 2.7: Gibbs free energy diagram of a one-step feasible reaction

The central concept of catalysis is the Gibbs free energy diagram, as shown in Figure 2.7. In a reaction, there is an activation energy (Ea) for reactants to overcome due to the breaking of bonds, which then reaches the peak which is a transition state. Once this is achieved, the transition state then forms bonds in a different configuration leading to the formation of products. The difference in Gibbs free energy between the reactants and the products is the Gibbs free energy change (ΔG). The diagram in Figure 2.7 shows a simple

one-step reaction. For a reaction to be feasible, the Gibbs free energy change (ΔG) must be negative.

In contrast, an electrochemical reaction consists of multiple steps. A single step consists of either an electrochemical step (usually involving simultaneous electron and proton transfer, named proton-coupled electron transfer or PCET) or a chemical step, which is a normal reaction that involves no transfer of protons or electrons. An example of the electrochemical reaction from CO_2 to CH_4 on Cu(211) is shown in Figure 2.8:[17]

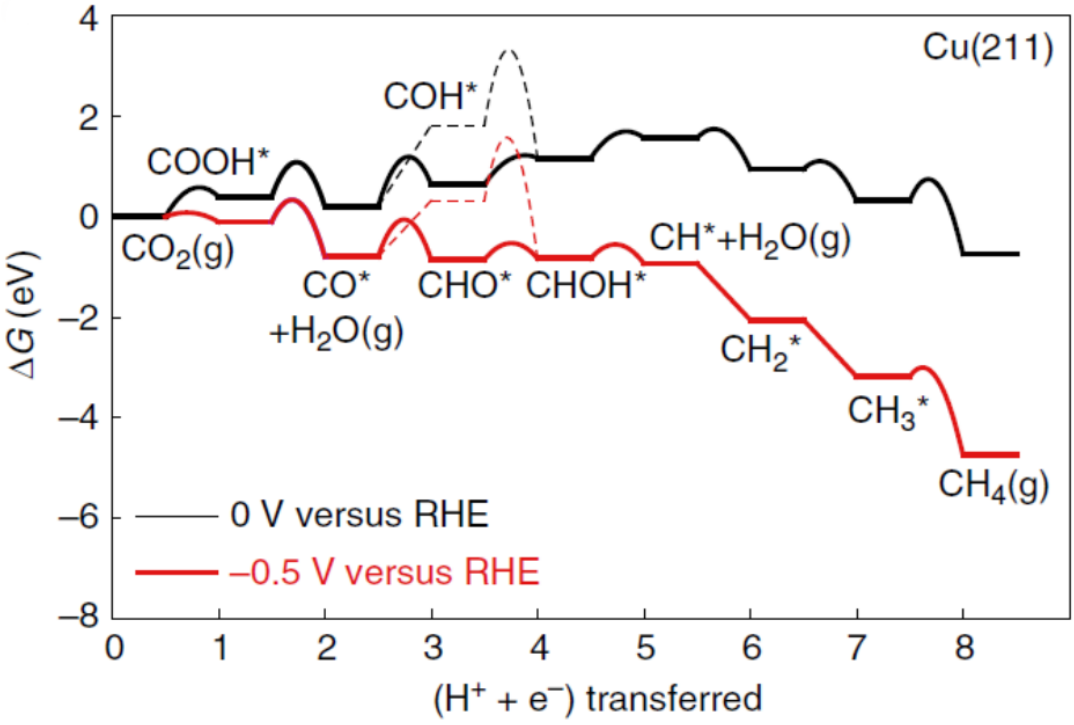

Figure 2.8: Gibbs free energy diagram of the 8e CO_2 to CH_4 reaction, taken from [17]. *No permission is required for thesis purposes.*

At 0V vs RHE, some steps have a positive ΔG, which implies an increase in entropy and thus the reaction is unfeasible. As the applied potential becomes more negative, there comes a point where all steps have negative ΔG and the limiting step has a ΔG of 0, known as the limiting potential (U_L). As can be seen in Figure 2.8, the limiting step with a ΔG of 0 is the *CO to *CHO step (solid line). The limiting potential (U_L) is greater than the E^0 half reduction potential because, even though the ΔG of the overall reaction is 0 already at 0V vs RHE, the ΔG of the individual steps are not. This difference is referred to as the

overpotential (η) as mentioned earlier. The limiting potential is catalyst-dependent because the individual steps are lowered by different amounts on different catalysts. Limiting potential, assuming perfect instrumentation to detect infinitesimal product amount, is equivalent to onset potential.

The activation energy (Ea) between the steps determines the rate constant, via the Arrhenius equation:

$$k = Ae^{-\frac{E_a}{T}}$$

As electrochemical reactions have multiple steps, the relationship between the Tafel slope and the rate constants of the individual steps is complicated and based on the surface coverage of the intermediates.[4] Theoretical Tafel slopes with different steps as the RDS can be computed, as has been done by Lee et al.[21]

2.4 Catalyst reconstruction

As the applied potential of the reaction for electrocatalysis is quite large, the electrical energy supplied does not merely induce reactions in the electrolyte but also induces change of the catalyst itself, which is referred to as catalyst reconstruction.[22] This happens when redox processes, catalyst surface changes or other reactions are energetically feasible at the applied potential. Catalysts can reduce (cathode side), oxidize (anode side), experience morphological changes (change in exposed crystal planes, etc). These effects can be classified into redox processes on one hand and surface topology changes on the other.[23]

Redox processes happen because the synthesized catalyst phase is not stable at the applied potential. For example, Cu oxides are reduced during electrochemical CO_2 reduction due to its thermodynamic instability in applied potentials more negative than 0V. This is illustrated via the Pourbaix diagram shown in Figure 2.9 (For more detailed Pourbaix diagram, check Beverskog et al[26]):

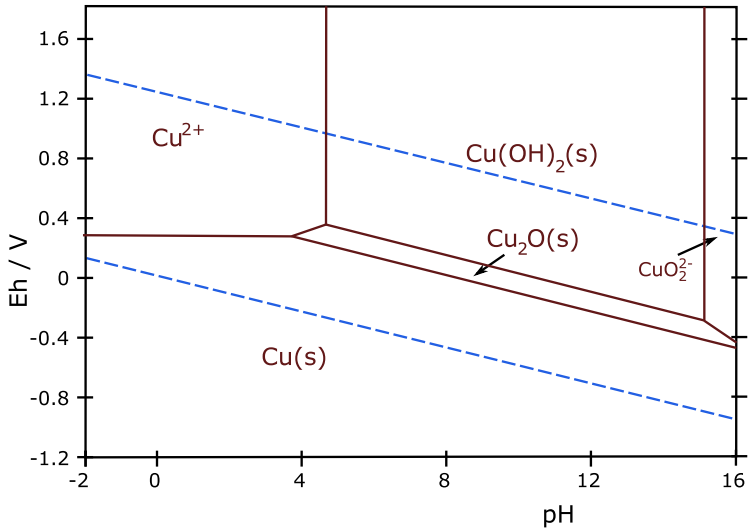

Figure 2.9: Pourbaix diagram of Cu and Cu oxides, taken from Wikipedia.

This type of reconstruction occasionally transforms the entire catalyst including the bulk, which implies that post-catalysis characterization should always be done to determine the catalyst state after reaction. However, this is also complicated by the fact that once the potential is removed, the most thermodynamically stable state is now the oxide (i.e. the catalyst re-oxidizes). In other words, post-catalysis characterization does not imply that the catalyst was in the same state during the reaction. In electrochemical CO_2 reduction, there was a debate over whether residual oxides are present in situ. Cuenya et al[24, 25] initially claimed that XPS measurement after the reaction imply the presence of copper during the reaction. In contrast, Ager et al[26, 27] found that no oxygen originated from the initial oxide by using isotopic labelling and in-situ Raman spectroscopy and proposed that the oxygen comes from catalyst re-oxidation. While the role of small amounts of residual subsurface oxides in the first 15 minutes or so can still be contended because of Cuenya et al's operando XANES experiments, this illustrates the importance of catalyst reconstruction and proper experimental verification to claims of activity involving chalcogenides or other catalysts where the Pourbaix diagram suggests its instability during the reaction.

The second type of catalyst reconstruction is surface typology changes. This happens because the catalyst atoms interact with the adsorbates and rearrange themselves. An

example of this phenomenon is the reconstruction of polycrystalline Cu into Cu(111) facets after 30 minutes and then Cu(100) facets after another 30 minutes as found by Kim et al.[28] The reconstruction to Cu(111) can be explained by the stability of the facet, but the eventual reconstruction to Cu(100) was unexpected. Sargent et al similarly find that the in situ electrodeposition of copper under CO_2 reduction conditions favours the Cu(100) facet.[29] They explain this phenomenon as due to the capping of CO_2RR intermediates which lowers the surface energy and favours the Cu(100) facet over the Cu(111) facet. This indicates that during CO_2RR, not only is CO_2 reduced by the catalyst, but the catalyst is also in turn affected by the CO_2, making the interaction two-way.

Thus, understanding of catalyst reconstruction (both redox and surface typology changes) and characterization of the catalyst after reduction (and even in-situ characterization) are necessary to understanding the behaviour of the catalyst during the CO_2RR reaction.

2.5 Materials for electrocatalytic CO_2 reduction

As mentioned in the introduction, the benchmark catalysts are Sn for $HCOO^-$ production, Ag for CO production and Cu for reduced products production. However, Ag is expensive, and Cu is not selective. As a result, research efforts are directed towards finding cheap and selective materials for CO_2 reduction to CO or reduced products. As monometallic catalysts have already been investigated, including the use of faceting, nanostructuring, etc, research efforts have been directed towards other categories of materials for electrocatalytic CO_2 reduction. These materials are elaborated in the following sections.

2.5.1 Cu bimetallic alloys

Bimetallic alloys have gained attention due to the ability to tune the resulting alloy's binding properties based on the ratio of the two metals as well as their structure (mixed, core-shell, etc).

Due to Cu being the most successful single metal for CO_2 reduction, bimetallic alloys have mostly focused on Cu-based bimetallics. The main products of Cu-based bimetallics are shown in Figure 2.10:

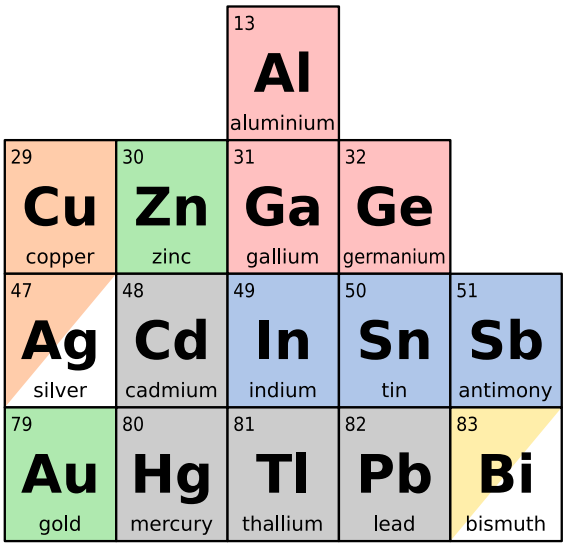

Figure 2.10: Schematic of main products of bimetallic formed with Cu and a second metal. Red indicates H_2, blue indicates CO, green indicates CO or CH_4, yellow indicates $HCOO^-$, and orange indicates reduced products. Grey elements are excluded due to toxicity, while Ag and Bi are not miscible with Cu.

In Figure 2.10, the (In, Sn, Sb) group weaken the C binding of Cu to form CO. (Zn, Au) produce CO as their major product by themselves and if alloyed with Cu, can promote CO or in minute amounts, reduced products. (Al, Ga, Ge) form H_2 when alloyed in more significant amounts. (Ag, Bi) are not miscible with Cu in their phase diagrams. (Cd, Hg, Tl, Pb) are toxic and as such are not considered for the project.

For (In, Sn, Sb), most research groups obtain CO as the dominant product when Cu is alloyed with (In, Sn, Sb). Takanabe and co-workers found that a Cu-In alloy biased at an electrode potential of -0.7V vs RHE selectively catalyzed CO_2 reduction to CO with an FE of 95%.[30] Takanabe and co-workers also found that a Cu-Sn alloy biased at −0.6 V vs RHE achieved an FE greater than 90% for CO_2 reduction to CO.[31] Mou et al found that a Cu-Sb alloy biased at an electrode potential of -0.9V vs RHE selectively catalyzed CO_2 reduction to CO with an FE of 86.5%.[32]

For (Al, Ga, Ge), if the alloy is predominantly Cu, some studies show increased reduced products formation on these alloys compared to pure Cu. Sargent and co-workers found that Cu-Al with a de-alloyed Al content of about 10% achieved an FE of 80% for C_2H_4 at a current density of 600mA/cm^2,[33] while Buonsanti and co-workers found that Cu-Ga with a Ga content of 17% achieved an FE of 52% for CH_4 at an applied voltage of -1.2 V vs RHE.[34] Thus, Al and Ga seem to favour the formation of different reduced products, with Al favouring C_2H_4 and Ga favouring CH_4.

For (Zn, Au), Cuenya and co-workers studied Cu-Zn alloy and found that while Cu-ZnO results in increased FE for CH_4, it slowly changes to CO as Cu and Zn form an alloy structure.[35] They proposed that ZnO induces lattice strain on the Cu which account for the increased production of reduced products, while CuZn alloy formation over time from the reduction of ZnO results in changed band structures that then disfavour said reduced products. Yang and co-workers initially found that adding substantial amounts of Au to Cu favours the production of CO,[36] but Sargent and co-workers later found that small amounts of Au added to Cu, at 7%, favours the formation of CH_4 and obtained an FE of 56% towards CH_4 with a partial current density of 112 mA cm^{-2}.[37] A similar trend appears for Cu-Zn, where Zn-heavy composition favours CO production.[38]

For (Ag, Bi), these elements are not miscible with Cu. Studies on these metallic "mixtures" show that CuAg produces reduced products and CuBi produces $HCOO^-$.[39, 40] This shows that CuAg is similar to Cu, while CuBi is similar to Bi. This indicates that: Ag can have surface strain effects on Cu to increase production of oxygenates but nonetheless maintains its overall tendency for reduced products, but Bi tunes Cu away to produce $HCOO^-$ in a similar manner to sulfur (see next section).[39, 40] This difference in behaviour is likely due to the mechanism of CO_2 reduction, where CO is an intermediate to reduced products but $HCOO^-$ lies on an entirely separate pathway.

Interestingly, these divergent behaviours may relate to the structure of their alloys. Nam and co-workers classified Cu-Au as forming a full solid solution and Cu-Zn and Cu-Al as forming intermediate solid solutions, while they classified Cu-In, Cu-Sn and Cu-Sb as

forming intermetallic compounds.[41] Small amount of alloying metal produces reduced products, while higher amount of alloying metal produces CO. In solid solutions (Cu-Au, Cu-Al and Cu-Zn), it behaves as expected. However, it is likely that due to the composition-restricted nature of intermetallic compounds (Cu-In, Cu-Sn, Cu-Sb), phase-separation results in phases with more second metal resulting in CO formation.

As the possible combinations of metals, facets and atomic motifs of these bimetallics (and also trimetallics) are very high, there have been extensive computational and machine learning studies on these metallics. Tran and Ulissi published a paper that took DFT results to train a machine learning model to predict possible high performing intermetallics with optimal CO adsorption energies.[42] A figure from their results is shown in Figure 2.11:

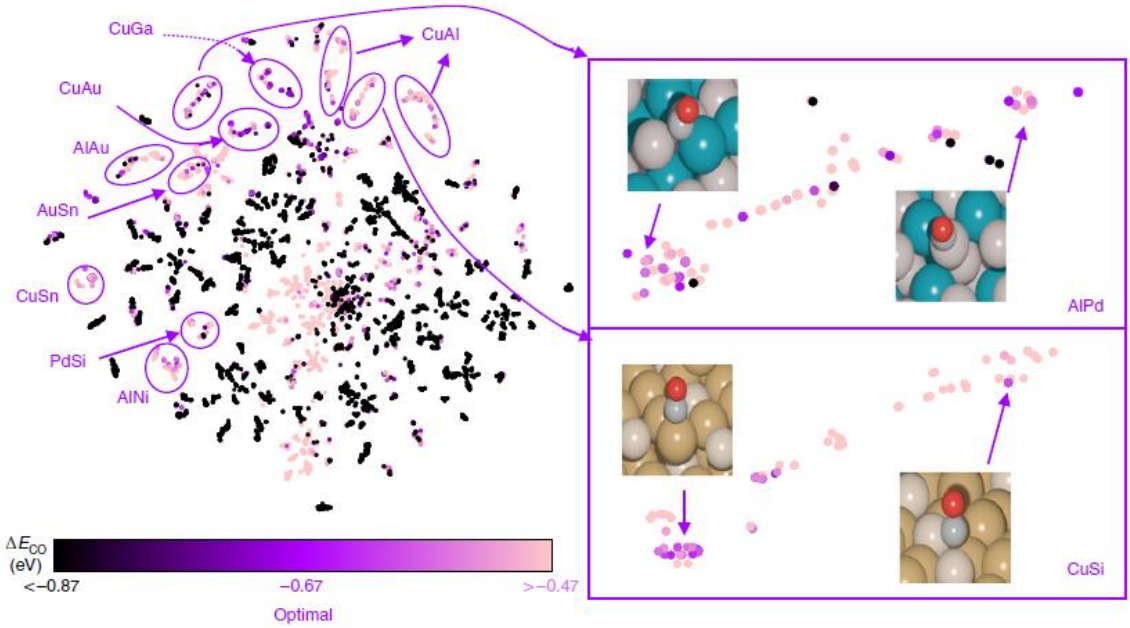

Figure 2.11: Active site motif analysis with optimal binding bimetallic catalysts labelled. Reproduced with permission from [42]

Most of the intermetallics in Figure 2.11 can be seen as transition metal-main group metal combinations:

Table 2.4: Classification of bimetallics for electrochemical CO_2RR identified in Figure 2.11 into transition metal and main group metal

Transition metal	**Main group metal**
Cu	Al
Cu	Ga
Cu, Au	
Au	Al
Au	Sn
Cu	Sn
Pd	Si
Ni	Al
Cu	Si
Pd	Al

From this study, the good heavy binding metals are Cu, Au and Pd, while good light binding metals are Al, Si and Sn. However, given that the machine learning was trained on somewhat sparse DFT results, the main group elements in Table 2.4 should be taken with a pinch of salt.

2.5.2 Chalcogenide-derived catalysts

Chalcogenide-derived catalysts (oxides, sulfides, selenides, etc) show different catalyst selectivity as compared to bare metallics. The most investigated catalysts are oxide-derived metals and sulfide-derived metals.

Oxide-derived metals show varying effects on electrochemical CO_2 reduction. Most metals have a thin oxide layer and the behaviour of this layer may be different for different metals. For example, Chen and Kanan showed that SnOx may be the source of catalytic activity for Sn in reducing CO_2 to $HCOO^-$, while Sn etched in strong acid to remove the surface SnOx layer shows significantly reduced activity.[43] In contrast, Lum and Ager showed that only a minute amount (<1%) of residual oxides remain after CO_2 reduction on Cu implying that their role in catalytic activity is insignificant.[26] Jiao and co-workers also state that although there is a small amount of oxide at potentials relevant to CO reduction,

it is not likely to be active.[44] The increased formation of ethanol on oxide-derived Cu is attributed to the formation of extra grain boundaries.[45] This implies that Transmission Electron Microscopy (TEM) can an important tool in understanding catalytic activities. Increasing the active surface area or engineering catalyst reconstruction such that the final catalyst form has more grain boundaries can be a good strategy for catalysts with increased activity for electrochemical CO_2 reduction. For example, Strasser and co-workers have found via in-situ TEM that copper(II) oxide nanoparticles evolve under electrochemical conditions to copper dendrites that resulted in increased C_2H_4 production.[46]

In contrast to the varying effect of oxides on the activity of the catalyst, sulfides seem to favour the formation of $HCOO^-$ on some metals. Zheng et al have found that sulfide-derived Sn is able to catalyse CO_2 reduction to $HCOO^-$ with improved Faradaic efficiency and current density when compared to tin.[47] Surprisingly, for sulfide-derived copper, Shinagawa et al found that the presence of the small amount of sulfur atoms in sulfide-derived Cu steers selectivity of copper towards $HCOO^-$ while suppressing the formation of CO or reduced products.[48] This was confirmed by Jiao and co-workers, who found that the addition of SO_2 to the CO_2 stream results in formation of sulfides, which slightly improves the FE of Sn for $HCOO^-$ but suppresses the formation of CO and reduced products on Cu.[49] They found however that sulfur does not affect CO production on Ag after SO_2 supply was stopped.

A likely explanation for the tuning of selectivity on sulfide-derived copper to $HCOO^-$ is CO poisoning of the surface. This was raised by Shao-Horn et al from in-situ surface-enhanced infrared absorption spectroscopy (SEIRAS) study which indicates high amount of adsorbed CO during CO_2RR.[50] This was also the finding from a computational study by Liu et al.[51] However, Deng et al with in-situ Raman spectroscopy found that sulfur suppresses the formation of *CO intermediates instead.[52] This research is also backed by the included computational study of Jiao et al who reported that *OCHO is more stable than *COOH on sulfur-doped copper.[49] More research is required to ascertain the true mechanism of sulfur in modifying the selectivity of sulfur-doped or sulfide-derived catalysts.

Other than $HCOO^-$, some studies reported a different role of sulfur in improving CO selectivity. An initial study by Lim et al indicate that sulfur can improve CO selectivity by imparting partial covalent character to the catalyst.[53] Since then, there have been no experimental reports on sulfur-doped Ag that demonstrates improved CO selectivity. However, CdS-derived catalyst was later reported by He et al to produce an 81% Faradaic efficiency for CO.[54] It is likely that sulfur modifies multiple mechanisms on metal catalysts and that the effect of sulfur on most catalysts is to improve $HCOO^-$, but that another effect that it can have in other catalysts is improved CO selectivity.

A key consideration of chalcogenide-derived materials is whether the parent chalcogenide acts as the active catalyst, or whether the chalcogenide reduces under the applied voltage and some other reduced phase acts as the active catalyst. An example if this is shown for Ag_2S:[55]

$Ag_2S(s) + 2e^- \rightleftharpoons 2\mathrm{Ag(s)} + S^{2-}$: -0.691V

The voltage shown is vs the standard hydrogen electrode (SHE). In this example, if the applied voltage is more negative than -0.69V vs SHE, Ag_2S might reduce,[22, 56, 57] and the active phase during catalysis will have to be determined by post-catalysis characterization (see section 2.4 on catalyst reconstruction).

Thus, chalcogenide-derived metals as catalysts affect the parent metal in different ways and more research in this area could yield more understanding of structure-property relationships of the catalyst and CO_2 reduction.

2.5.3 Metal-nitrogen doped carbon (MNC)

Metal atoms anchored on porphyrin, phthalocyanine or other complexes have been used as catalysts for electrochemical CO_2 reduction, producing mainly reports of CO but also methane and even methanol.[58, 59] However in a recent study, Varela et al reported Fe and Mn anchored on N-doped carbon black for electrochemical CO_2 reduction and found CO_2 to CO Faradaic efficiencies of about 80%.[60] Subsequent studies found Ni anchored on N-doped carbon to be the most active, reaching >90% Faradaic efficiency.[61-63] Thus,

Ni-NC catalysts have become cheap (vs Ag, Au) but highly efficient for electrochemical CO_2 reduction to CO.

2.6 Focus of study: Cu-M-sulfide-derived catalysts

As two-element catalysts (copper bimetallics, metal chalcogenides) have been investigated by the literature with limited selectivities, this study aims to increase their selectivities by including chalcogen into the copper bimetallics. The inclusion of chalcogen may improve the selectivity of $HCOO^-$ or CO via the two mechanisms as discussed earlier, while the inclusion of two metals allows greater tuning of binding energy. Two metals are chosen, Cu and another metal from a weak-binding group (In, Sn, Sb, Bi) to form a bimetallic sulfide. Other metals (Ga, Ge, Ag, Co, Fe) are also included in case the catalysts from these sulfides demonstrate surprising behaviours. The predicted behaviours of all these catalysts are summarized below:

Table 2.5: Bimetallic catalyst selectivities and predicted selectivities in their sulfide-derived versions

Metal combination	**Main product without sulfur**	**Predicted main product with sulfur**
Cu-In	CO	CO or $HCOO^-$
Cu-Sn		
Cu-Sb		
Cu-Bi	$HCOO^-$	$HCOO^-$
Cu-Ag	CO and reduced products	Unknown
Cu-Ga	Can produce reduced products if Cu-heavy	Hydrogen
Cu-Ge		
Cu-Co		
Cu-Fe		

This study aims to test the effect of sulfur in the bimetallic sulfide-derived catalysts and see if a high FE for a product other than $HCOO^-$ can be obtained since $HCOO^-$ appears to be favoured on sulfide-derived materials. If this is achieved, the reaction mechanisms and how sulfur affects the binding energies of the intermediates, especially in the presence of two metals, can also be elucidated.

References

[1] T. Burdyny and W. A. Smith, "CO2 reduction on gas-diffusion electrodes and why catalytic performance must be assessed at commercially-relevant conditions," *Energy & Environmental Science,* 10.1039/C8EE03134G vol. 12, no. 5, pp. 1442-1453, 2019, doi: 10.1039/C8EE03134G.

[2] J. E. Pander Iii, D. Ren, and B. S. Yeo, "Practices for the collection and reporting of electrocatalytic performance and mechanistic information for the CO2 reduction reaction," *Catalysis Science & Technology,* 10.1039/C7CY01785E vol. 7, no. 24, pp. 5820-5832, 2017, doi: 10.1039/C7CY01785E.

[3] C. Batchelor-McAuley, "Defining the onset potential," *Current Opinion in Electrochemistry,* vol. 37, p. 101176, 2023/02/01/ 2023, doi: https://doi.org/10.1016/j.coelec.2022.101176.

[4] T. Shinagawa, A. T. Garcia-Esparza, and K. Takanabe, "Insight on Tafel slopes from a microkinetic analysis of aqueous electrocatalysis for energy conversion," *Scientific Reports,* vol. 5, no. 1, p. 13801, 2015/09/08 2015, doi: 10.1038/srep13801.

[5] J. T. Feaster *et al.*, "Understanding Selectivity for the Electrochemical Reduction of Carbon Dioxide to Formic Acid and Carbon Monoxide on Metal Electrodes," *ACS Catalysis,* vol. 7, no. 7, pp. 4822-4827, 2017/07/07 2017, doi: 10.1021/acscatal.7b00687.

[6] R. Kortlever, J. Shen, K. J. P. Schouten, F. Calle-Vallejo, and M. T. M. Koper, "Catalysts and Reaction Pathways for the Electrochemical Reduction of Carbon Dioxide," *The Journal of Physical Chemistry Letters,* vol. 6, no. 20, pp. 4073-4082, 2015/10/15 2015, doi: 10.1021/acs.jpclett.5b01559.

[7] M. T. Tang, H. Peng, P. S. Lamoureux, M. Bajdich, and F. Abild-Pedersen, "From electricity to fuels: Descriptors for C1 selectivity in electrochemical CO2 reduction," *Applied Catalysis B: Environmental,* vol. 279, p. 119384, 2020/12/15/ 2020, doi: https://doi.org/10.1016/j.apcatb.2020.119384.

[8] C. Shi, H. A. Hansen, A. C. Lausche, and J. K. Nørskov, "Trends in electrochemical CO2 reduction activity for open and close-packed metal surfaces," *Physical Chemistry Chemical Physics,* 10.1039/C3CP54822H vol. 16, no. 10, pp. 4720-4727, 2014, doi: 10.1039/C3CP54822H.

[9] A. Vasileff, C. Xu, Y. Jiao, Y. Zheng, and S.-Z. Qiao, "Surface and Interface Engineering in Copper-Based Bimetallic Materials for Selective CO2 Electroreduction," *Chem,* vol. 4, no. 8, pp. 1809-1831, 2018/08/09/ 2018, doi: https://doi.org/10.1016/j.chempr.2018.05.001.

[10] D. Gao, H. Zhou, F. Cai, J. Wang, G. Wang, and X. Bao, "Pd-Containing Nanostructures for Electrochemical CO2 Reduction Reaction," *ACS Catalysis,* vol. 8, no. 2, pp. 1510-1519, 2018/02/02 2018, doi: 10.1021/acscatal.7b03612.

[11] X. Ma, Z. Li, L. E. K. Achenie, and H. Xin, "Machine-Learning-Augmented Chemisorption Model for CO2 Electroreduction Catalyst Screening," *The Journal of Physical Chemistry Letters,* vol. 6, no. 18, pp. 3528-3533, 2015/09/17 2015, doi: 10.1021/acs.jpclett.5b01660.

[12] Y. Hori, H. Wakebe, T. Tsukamoto, and O. Koga, "Adsorption of CO accompanied with simultaneous charge transfer on copper single crystal electrodes related with electrochemical reduction of CO2 to hydrocarbons," *Surface Science,* vol. 335, pp. 258-263, 1995/07/20/ 1995, doi: https://doi.org/10.1016/0039-6028(95)00441-6.

[13] Y. Huang, A. D. Handoko, P. Hirunsit, and B. S. Yeo, "Electrochemical Reduction of CO2 Using Copper Single-Crystal Surfaces: Effects of CO* Coverage on the Selective Formation of Ethylene," *ACS Catalysis,* vol. 7, no. 3, pp. 1749-1756, 2017/03/03 2017, doi: 10.1021/acscatal.6b03147.

[14] W. Luo, X. Nie, M. J. Janik, and A. Asthagiri, "Facet Dependence of CO2 Reduction Paths on Cu Electrodes," *ACS Catalysis,* vol. 6, no. 1, pp. 219-229, 2016/01/04 2016, doi: 10.1021/acscatal.5b01967.

[15] T. Cheng, H. Xiao, and W. A. Goddard, "Full atomistic reaction mechanism with kinetics for CO reduction on Cu(100) from ab initio molecular dynamics free-energy calculations at 298 K," *Proceedings of the National Academy of Sciences,* vol. 114, no. 8, pp. 1795-1800, 2017, doi: doi:10.1073/pnas.1612106114.

[16] H. Xiao, T. Cheng, W. A. Goddard, III, and R. Sundararaman, "Mechanistic Explanation of the pH Dependence and Onset Potentials for Hydrocarbon Products from Electrochemical Reduction of CO on Cu (111)," *Journal of the American Chemical Society,* vol. 138, no. 2, pp. 483-486, 2016/01/20 2016, doi: 10.1021/jacs.5b11390.

[17] X. Liu, J. Xiao, H. Peng, X. Hong, K. Chan, and J. K. Nørskov, "Understanding trends in electrochemical carbon dioxide reduction rates," *Nature Communications,* vol. 8, no. 1, p. 15438, 2017/05/22 2017, doi: 10.1038/ncomms15438.

[18] R. B. Sandberg, J. H. Montoya, K. Chan, and J. K. Nørskov, "CO-CO coupling on Cu facets: Coverage, strain and field effects," *Surface Science,* vol. 654, pp. 56-62, 2016/12/01/ 2016, doi: https://doi.org/10.1016/j.susc.2016.08.006.

[19] D. Ren, B. S.-H. Ang, and B. S. Yeo, "Tuning the Selectivity of Carbon Dioxide Electroreduction toward Ethanol on Oxide-Derived CuxZn Catalysts," *ACS Catalysis,* vol. 6, no. 12, pp. 8239-8247, 2016/12/02 2016, doi: 10.1021/acscatal.6b02162.

[20] Y. Baek *et al.*, "Electrochemical carbon dioxide reduction on copper–zinc alloys: ethanol and ethylene selectivity analysis," *Journal of Materials Chemistry A,* 10.1039/D1TA10345H vol. 10, no. 17, pp. 9393-9401, 2022, doi: 10.1039/D1TA10345H.

[21] C. W. Lee *et al.*, "New challenges of electrokinetic studies in investigating the reaction mechanism of electrochemical CO2 reduction," *Journal of Materials Chemistry A,* 10.1039/C8TA03480J vol. 6, no. 29, pp. 14043-14057, 2018, doi: 10.1039/C8TA03480J.

[22] H. Jiang, Q. He, Y. Zhang, and L. Song, "Structural Self-Reconstruction of Catalysts in Electrocatalysis," *Accounts of Chemical Research,* vol. 51, no. 11, pp. 2968-2977, 2018/11/20 2018, doi: 10.1021/acs.accounts.8b00449.

[23] W. Zhang, Y. Yang, Y. Tang, and Q. Gao, "In-situ reconstruction of catalysts in cathodic electrocatalysis: New insights into active-site structures and working mechanisms," *Journal of Energy Chemistry,* vol. 70, pp. 414-436, 2022/07/01/ 2022, doi: https://doi.org/10.1016/j.jechem.2022.02.036.

[24] D. Gao *et al.*, "Plasma-Activated Copper Nanocube Catalysts for Efficient Carbon Dioxide Electroreduction to Hydrocarbons and Alcohols," *ACS Nano,* vol. 11, no. 5, pp. 4825-4831, 2017/05/23 2017, doi: 10.1021/acsnano.7b01257.

[25] H. Mistry *et al.*, "Highly selective plasma-activated copper catalysts for carbon dioxide reduction to ethylene," (in eng), *Nat Commun,* vol. 7, p. 12123, Jun 30 2016, doi: 10.1038/ncomms12123.

[26] Y. Lum and J. W. Ager, "Stability of Residual Oxides in Oxide-Derived Copper Catalysts for Electrochemical CO2 Reduction Investigated with 18O Labeling," *Angewandte Chemie International Edition,* vol. 57, no. 2, pp. 551-554, 2018, doi: https://doi.org/10.1002/anie.201710590.

[27] L. Mandal *et al.*, "Investigating the Role of Copper Oxide in Electrochemical CO2 Reduction in Real Time," *ACS Applied Materials & Interfaces,* vol. 10, no. 10, pp. 8574-8584, 2018/03/14 2018, doi: 10.1021/acsami.7b15418.

[28] Y.-G. Kim, J. H. Baricuatro, A. Javier, J. M. Gregoire, and M. P. Soriaga, "The Evolution of the Polycrystalline Copper Surface, First to Cu(111) and Then to Cu(100), at a Fixed CO2RR Potential: A Study by Operando EC-STM," *Langmuir,* vol. 30, no. 50, pp. 15053-15056, 2014/12/23 2014, doi: 10.1021/la504445g.

[29] Y. Wang *et al.*, "Catalyst synthesis under CO2 electroreduction favours faceting and promotes renewable fuels electrosynthesis," *Nature Catalysis,* vol. 3, no. 2, pp. 98-106, 2020/02/01 2020, doi: 10.1038/s41929-019-0397-1.

[30] S. Rasul, D. H. Anjum, A. Jedidi, Y. Minenkov, L. Cavallo, and K. Takanabe, "A Highly Selective Copper–Indium Bimetallic Electrocatalyst for the Electrochemical Reduction of Aqueous CO2 to CO," *Angewandte Chemie International Edition,* vol. 54, no. 7, pp. 2146-2150, 2015, doi: https://doi.org/10.1002/anie.201410233.

[31] S. Sarfraz, A. T. Garcia-Esparza, A. Jedidi, L. Cavallo, and K. Takanabe, "Cu–Sn Bimetallic Catalyst for Selective Aqueous Electroreduction of CO2 to CO," *ACS Catalysis,* vol. 6, no. 5, pp. 2842-2851, 2016/05/06 2016, doi: 10.1021/acscatal.6b00269.

[32] S. Mou *et al.*, "Cu2Sb decorated Cu nanowire arrays for selective electrocatalytic CO2 to CO conversion," *Nano Research,* vol. 14, no. 8, pp. 2831-2836, 2021/08/01 2021, doi: 10.1007/s12274-021-3295-1.

[33] M. Zhong *et al.*, "Accelerated discovery of CO2 electrocatalysts using active machine learning," *Nature,* vol. 581, no. 7807, pp. 178-183, 2020/05/01 2020, doi: 10.1038/s41586-020-2242-8.

[34] V. Okatenko *et al.*, "Alloying as a Strategy to Boost the Stability of Copper Nanocatalysts during the Electrochemical CO2 Reduction Reaction," *Journal of the American Chemical Society,* vol. 145, no. 9, pp. 5370-5383, 2023/03/08 2023, doi: 10.1021/jacs.2c13437.

[35] H. S. Jeon *et al.*, "Operando Insight into the Correlation between the Structure and Composition of CuZn Nanoparticles and Their Selectivity for the Electrochemical CO2 Reduction," *Journal of the American Chemical Society,* vol. 141, no. 50, pp. 19879-19887, 2019/12/18 2019, doi: 10.1021/jacs.9b10709.

[36] D. Kim, J. Resasco, Y. Yu, A. M. Asiri, and P. Yang, "Synergistic geometric and electronic effects for electrochemical reduction of carbon dioxide using gold–copper bimetallic nanoparticles," *Nature Communications,* vol. 5, no. 1, p. 4948, 2014/09/11 2014, doi: 10.1038/ncomms5948.

[37] X. Wang *et al.*, "Gold-in-copper at low *CO coverage enables efficient electromethanation of CO2," *Nature Communications,* vol. 12, no. 1, p. 3387, 2021/06/07 2021, doi: 10.1038/s41467-021-23699-4.

[38] L. Wang *et al.*, "Bimetallic effects on Zn-Cu electrocatalysts enhance activity and selectivity for the conversion of CO2 to CO," *Chem Catalysis,* vol. 1, no. 3, pp. 663-680, 2021/08/19/ 2021, doi: https://doi.org/10.1016/j.checat.2021.05.006.

[39] L. Jia *et al.*, "Copper-Bismuth Bimetallic Microspheres for Selective Electrocatalytic Reduction of CO2 to Formate," *Chinese Journal of Chemistry,* vol. 37, no. 5, pp. 497-500, 2019, doi: https://doi.org/10.1002/cjoc.201900010.

[40] E. L. Clark, C. Hahn, T. F. Jaramillo, and A. T. Bell, "Electrochemical CO2 Reduction over Compressively Strained CuAg Surface Alloys with Enhanced Multi-Carbon Oxygenate Selectivity," *Journal of the American Chemical Society,* vol. 139, no. 44, pp. 15848-15857, 2017/11/08 2017, doi: 10.1021/jacs.7b08607.

[41] C. W. Lee *et al.*, "Defining a Materials Database for the Design of Copper Binary Alloy Catalysts for Electrochemical CO2 Conversion," *Advanced Materials,* vol. 30, no. 42, p. 1704717, 2018, doi: https://doi.org/10.1002/adma.201704717.

[42] K. Tran and Z. W. Ulissi, "Active learning across intermetallics to guide discovery of electrocatalysts for CO2 reduction and H2 evolution," *Nature Catalysis,* vol. 1, no. 9, pp. 696-703, 2018/09/01 2018, doi: 10.1038/s41929-018-0142-1.

[43] Y. Chen and M. W. Kanan, "Tin Oxide Dependence of the CO2 Reduction Efficiency on Tin Electrodes and Enhanced Activity for Tin/Tin Oxide Thin-Film Catalysts," *Journal of the American Chemical Society,* vol. 134, no. 4, pp. 1986-1989, 2012/02/01 2012, doi: 10.1021/ja2108799.

[44] Y. Zhao *et al.*, "Speciation of Cu Surfaces During the Electrochemical CO Reduction Reaction," *Journal of the American Chemical Society,* vol. 142, no. 21, pp. 9735-9743, 2020/05/27 2020, doi: 10.1021/jacs.0c02354.
[45] C. W. Li, J. Ciston, and M. W. Kanan, "Electroreduction of carbon monoxide to liquid fuel on oxide-derived nanocrystalline copper," *Nature,* vol. 508, no. 7497, pp. 504-507, 2014/04/01 2014, doi: 10.1038/nature13249.
[46] X. Wang *et al.*, "Morphology and mechanism of highly selective Cu(II) oxide nanosheet catalysts for carbon dioxide electroreduction," *Nature Communications,* vol. 12, no. 1, p. 794, 2021/02/04 2021, doi: 10.1038/s41467-021-20961-7.
[47] X. Zheng *et al.*, "Sulfur-Modulated Tin Sites Enable Highly Selective Electrochemical Reduction of CO2 to Formate," *Joule,* vol. 1, no. 4, pp. 794-805, 2017/12/20/ 2017, doi: https://doi.org/10.1016/j.joule.2017.09.014.
[48] T. Shinagawa, G. O. Larrazábal, A. J. Martín, F. Krumeich, and J. Pérez-Ramírez, "Sulfur-Modified Copper Catalysts for the Electrochemical Reduction of Carbon Dioxide to Formate," *ACS Catalysis,* vol. 8, no. 2, pp. 837-844, 2018/02/02 2018, doi: 10.1021/acscatal.7b03161.
[49] W. Luc *et al.*, "SO2-Induced Selectivity Change in CO2 Electroreduction," *Journal of the American Chemical Society,* vol. 141, no. 25, pp. 9902-9909, 2019/06/26 2019, doi: 10.1021/jacs.9b03215.
[50] K. R. Phillips, Y. Katayama, J. Hwang, and Y. Shao-Horn, "Sulfide-Derived Copper for Electrochemical Conversion of CO2 to Formic Acid," *The Journal of Physical Chemistry Letters,* vol. 9, no. 15, pp. 4407-4412, 2018/08/02 2018, doi: 10.1021/acs.jpclett.8b01601.
[51] D. Liu, Y. Liu, and M. Li, "Understanding How Atomic Sulfur Controls the Selectivity of the Electroreduction of CO2 to Formic Acid on Metallic Cu Surfaces," *The Journal of Physical Chemistry C,* vol. 124, no. 11, pp. 6145-6153, 2020/03/19 2020, doi: 10.1021/acs.jpcc.9b11830.
[52] Y. Deng *et al.*, "On the Role of Sulfur for the Selective Electrochemical Reduction of CO2 to Formate on CuSx Catalysts," *ACS Applied Materials & Interfaces,* vol. 10, no. 34, pp. 28572-28581, 2018/08/29 2018, doi: 10.1021/acsami.8b08428.
[53] H.-K. Lim, H. Shin, W. A. Goddard, Y. J. Hwang, B. K. Min, and H. Kim, "Embedding Covalency into Metal Catalysts for Efficient Electrochemical Conversion of CO2," *Journal of the American Chemical Society,* vol. 136, no. 32, pp. 11355-11361, 2014/08/13 2014, doi: 10.1021/ja503782w.
[54] R. He *et al.*, "Achieving the Widest Range of Syngas Proportions at High Current Density over Cadmium Sulfoselenide Nanorods in CO2 Electroreduction," *Advanced Materials,* vol. 30, no. 7, p. 1705872, 2018, doi: https://doi.org/10.1002/adma.201705872.
[55] P. Vanysek, "Electrochemical series," *CRC handbook of chemistry and physics,* vol. 8, pp. 8-33, 2000.
[56] S. Licht, "Aqueous Solubilities, Solubility Products and Standard Oxidation‐Reduction Potentials of the Metal Sulfides," *Journal of The Electrochemical Society,* vol. 135, no. 12, p. 2971, 1988/12/01 1988, doi: 10.1149/1.2095471.
[57] N. Elgrishi, K. J. Rountree, B. D. McCarthy, E. S. Rountree, T. T. Eisenhart, and J. L. Dempsey, "A Practical Beginner's Guide to Cyclic Voltammetry," *Journal of Chemical Education,* vol. 95, no. 2, pp. 197-206, 2018/02/13 2018, doi: 10.1021/acs.jchemed.7b00361.
[58] M. Li, H. Wang, W. Luo, P. C. Sherrell, J. Chen, and J. Yang, "Heterogeneous Single-Atom Catalysts for Electrochemical CO2 Reduction Reaction," *Advanced Materials,* vol. 32, no. 34, p. 2001848, 2020, doi: https://doi.org/10.1002/adma.202001848.
[59] Y. Wu, Z. Jiang, X. Lu, Y. Liang, and H. Wang, "Domino electroreduction of CO2 to methanol on a molecular catalyst," *Nature,* vol. 575, no. 7784, pp. 639-642, 2019/11/01 2019, doi: 10.1038/s41586-019-1760-8.
[60] A. S. Varela, N. Ranjbar Sahraie, J. Steinberg, W. Ju, H.-S. Oh, and P. Strasser, "Metal-Doped Nitrogenated Carbon as an Efficient Catalyst for Direct CO2 Electroreduction to CO and

Hydrocarbons," *Angewandte Chemie International Edition,* vol. 54, no. 37, pp. 10758-10762, 2015, doi: https://doi.org/10.1002/anie.201502099.

[61] W. Ju *et al.*, "Understanding activity and selectivity of metal-nitrogen-doped carbon catalysts for electrochemical reduction of CO2," *Nature Communications,* vol. 8, no. 1, p. 944, 2017/10/16 2017, doi: 10.1038/s41467-017-01035-z.

[62] X.-M. Hu *et al.*, "Selective CO2 Reduction to CO in Water using Earth-Abundant Metal and Nitrogen-Doped Carbon Electrocatalysts," *ACS Catalysis,* vol. 8, no. 7, pp. 6255-6264, 2018/07/06 2018, doi: 10.1021/acscatal.8b01022.

[63] P. Lu *et al.*, "Facile synthesis of single-nickel-atomic dispersed N-doped carbon framework for efficient electrochemical CO2 reduction," *Applied Catalysis B: Environmental,* vol. 241, pp. 113-119, 2019/02/01/ 2019, doi: https://doi.org/10.1016/j.apcatb.2018.09.025.

Chapter 3 Experimental Methodology

This chapter describes the synthesis, electrochemical performance testing and characterization methods used in the study. Synthesis methods include solution-based heat up and solvothermal methods. Electrochemical performance testing methods include chronopotentiometry, chronoamperometry, EIS, LSV, CV, etc. Characterization methods include SEM, EDX, XRD, XPS.

3.1 Rationale for selection

Solution-based nanoparticle synthesis route was chosen as a simpler and cheaper way to synthesize catalysts for CO_2 reduction. As the catalysts have to be deposited on gas diffusion electrodes to be used in the flow cell, this precludes the use of thin films for catalysts.

The gas diffusion electrode flow cell was chosen due to the ability to circumvent the solubility limit of CO_2 in aqueous electrolyte, thus allowing high current densities to be applied without drastic FE loss due to local CO_2 depletion. This is done by supplying gaseous CO_2 directly to the catalyst via a porous gas diffusion electrode (GDE) without the need to saturate the electrolyte with CO_2. The supply of CO_2 to the catalyst was noted by Burdyny and Smith as important to the selectivity of the CO_2RR reaction and an excellent review on this topic has been given by them.[1]

Chronoamperometry (constant potential) was chosen because selectivity is a function of the driving force applied on the catalyst and as such is more representative of catalyst behaviour. While chronopotentiometry is easier to carry out in practice due to the difficulty of determining the instantaneous current (the time representative of when the gases are injected into the GC) in chronoamperometry for FE calculations, it was decided that because the catalyst studied has not been reported before in literature, it is necessary to elucidate potential-specific FE.

Characterization was carried out both before and after synthesis to compare the catalyst structure and determine the changes that occurred during catalysis. Catalyst change is important as reconstruction or reduction of the catalyst plays a key role in determining the composition and structure of catalyst that is active for CO_2 reduction. Very often the initial composition or structure is not the active phase during CO_2 reduction, especially for chalcogenide-derived catalysts as the chalcogen atoms usually dissolve in solution when a reducing potential is applied. Standard techniques for characterization are used, with XRD for phase identification, SEM for morphology, EDX for elemental composition analysis and XPS for elemental composition and oxidation state analysis.

3.2 Synthesis methods

Two different synthesis methods were used in this study. Both are solution-processing methods and primarily differ in their use of polar (solvothermal) or organic (heat-up colloidal) solvents.

3.2.1 Solvothermal synthesis

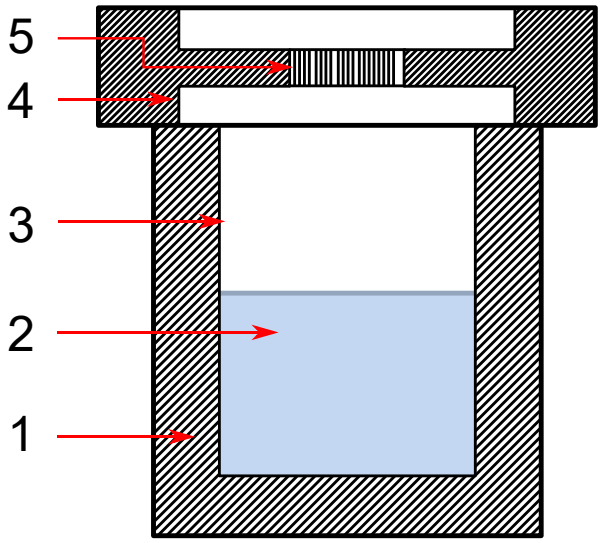

Figure 3.1: Schematic of solvothermal autoclave, taken from Wikipedia. (1) stainless steel autoclave (2) precursor solution (3) Teflon liner (4) stainless steel lid (5) spring

The first is solvothermal synthesis. Solvothermal synthesis involves the reaction of precursors in a solvent incompletely filled in an inert PTFE liner, which is placed in a steel autoclave to withstand high pressures present in the reaction vessel. The vessel is heated near or above the boiling point of the solvent to facilitate the decomposition of the sulfur source.[2] If the reaction is carried out above the boiling point of the solvent, the fixed volume of the autoclave ensures that the solvent stays liquid in supercritical state which allows for the formation and growth of nanoparticles.

Solvent choice is critical in solvothermal synthesis, where non-water solvents with high boiling points were chosen. This is to ensure that the reaction can be carried out safely at high temperatures and that reaction intermediates are not hydrolyzed while reacting to enable the formation of ternary sulfides. Solvents can favour thermodynamically stable

structures if they interact minimally with metal ion precursors or favour metastable structures if they form complexes with the metal ions. Ethylene glycol was used when zinc blende or cubic-derived phases were desired,[3] while ethylenediamine was used when wurtzite or hexagonal-derived phases were desired due to its amine complexing ability.[4] Thiourea was used as the sulfur source.

Stoichiometric amounts of copper(II) and another metal precursor is mixed in ethylene glycol or ethylenediamine until they dissolve, after which thiourea is added. The separate addition of metal precursor and thiourea is to prevent undesired reaction products before they dissolve. The mixture is then placed in a Teflon-lined steel autoclave and placed in an oven where the temperature is set between 120°C to 200°C for several hours for the formation of nanoparticles. The solution is then cooled to room temperature naturally, centrifuged and washed by ethanol, water and IPA before drying in an oven.

3.2.2 Heat-up colloidal synthesis

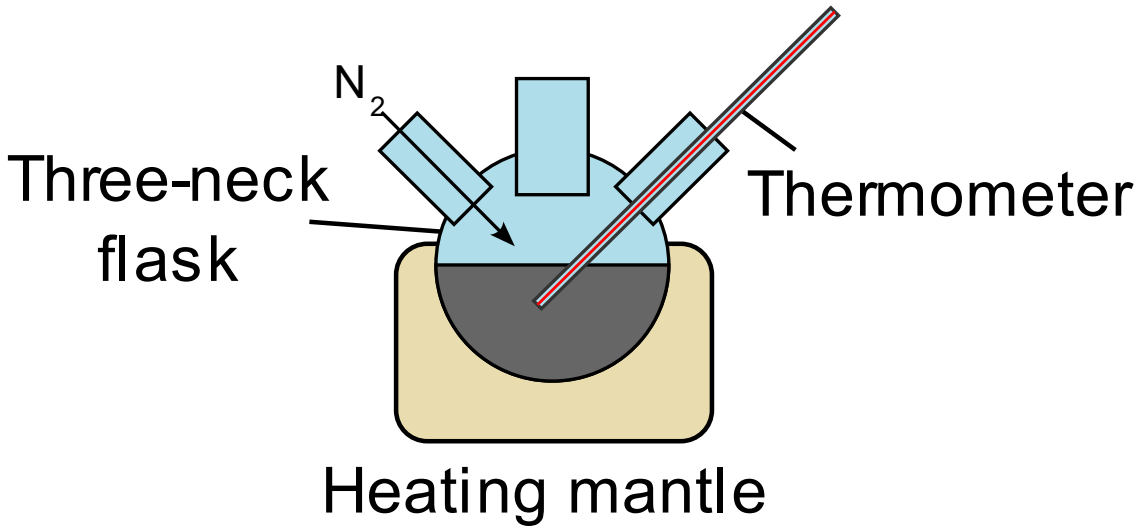

Figure 3.2: Schematic of heating mantle and three-neck flask for heat-up synthesis.

The second is heat-up colloidal synthesis. This involves the use of organic solvents with organic coordinating ligands such as oleylamine or trioctylphosphine oxide for the synthesis of nanoparticles with good phase and morphology control.[5, 6] Alternatively, the coordinating ligands themselves are used as solvents, but in practice this has a downside of it being difficult to remove the ligands after synthesis. This heat-up method originated

in the hot injection method to produce monodisperse cadmium chalcogenide quantum dots where reactants were separately heated and then injected, but where such accurate control is not necessary, heat-up synthesis is safer and more scalable.[5]

1-Octadecene was chosen as solvent for easier washing of nanoparticles and oleylamine was chosen as coordinating agent as oleylamine is less toxic than trioctylphosphine oxide.[6] 1-Dodecanethiol was used as the sulfur source due to its complexing ability which allows for more accurate phase control.[7]

Stoichiometric amounts of copper(II) and another metal precursor together with 1-dodecanethiol is mixed in 1-octadecene and oleylamine in a three-neck flask, with the solution heated to 150°C for 30 minutes under nitrogen flow to degas moisture and oxygen before being heated to between 220°C to 250°C for about an hour for the formation of nanoparticles. The solution is then cooled to room temperature naturally, centrifuged, washed in hexane:ethanol mixtures for the removal of organic solvents and coordinating agents and then washed in ethanol and IPA before drying in an oven.

3.2.3 Chapter-specific details

3.2.3.1 Chapter 4

Metal precursors used for (In, Sn, Sb, Ga, Ge, Ag, Co, Fe) are $InCl_3$, $Sn(OAc)_4$, $Sb(OAc)_3$, $Ga(NO_3)_3$, $GeBr_2$, $Ag(NO_3)$, $Fe(acac)_2$ and $Co(acac)_2$.

- For Cu_2SnS_3, 2.5mmol of copper(II) acetylacetonate, 1.25mmol of tin(IV) acetate were used.
- For $Cu_{12}Sb_4S_{13}$, 3.75mmol of copper(II) acetylacetonate, 1.25mmol of antimony(III) acetate were used.
- For $CuGaS_2$, 2mmol of copper(II) acetylacetonate, 2mmol of gallium nitrate were used.
- For Cu_2GeS_3, 2.5mmol of copper(II) acetylacetonate, 1.25mmol of germanium(II) bromide were used.
- For CuAgS, 2mmol of copper(II) acetylacetonate, 2mmol of silver nitrate were used.

- For $CuFeS_2$, 2mmol of copper(II) acetylacetonate, 2mmol of iron(III) acetylacetonate were used.
- For $CuCo_2S_4$, 1mmol of copper(II) acetylacetonate, 2mmol of cobalt(II) acetylacetonate were used.

These salts were dissolved in 24ml of 1-octadecene and mixed with 3ml of oleylamine and 3ml of dodecanethiol. The mixture was then heated to 150°C for 30 minutes to degas water and oxygen then heated to 250°C for 1h for the formation of nanoparticles. Solutions were cooled naturally and centrifuged and washed according to the heat-up synthesis procedure described in methods.

$CuInS_2$ and Cu_3BiS_3 were synthesized via solvothermal reaction.

- 0.4mmol of copper(II) chloride dihydrate, 0.4mmol of indium(III) chloride were dissolved in 50ml of ethylene glycol and 0.9mmol of thiourea was then added. The mixture was then transferred to a 120ml PTFE-lined steel autoclave, placed in an oven and heated at 180°C for 24h.
- 4.5mmol of copper(II) chloride dihydrate, 1.5mmol of bismuth nitrate were dissolved in 60mol of ethylenediamine and 5mmol of thiourea was then added. The mixture was then transferred to a 120ml PTFE-lined steel autoclave, placed in an oven and heated at 180°C for 15h.

The solution was cooled naturally and centrifuged and washed according to the solvothermal synthesis procedure described in methods.

3.2.3.2 Chapter 5

Three Cu-Sb-S phases were synthesized following a paper by Ramasamy et al who managed to synthesize all four Cu-Sb-S phases.[7] As heat-up method with no hot injection was used, it was difficult to synthesize pure phase of famatinite (Cu_3SbS_4) and hence it was not included among the samples.

1. For Cu_3SbS_3, 3.75mmol of copper(II) acetylacetonate, 1.25mmol of antimony(III) acetate, 3ml of 1-dodecanethiol and 3ml of oleylamine were dissolved in 24ml of 1-octadecene in a 250ml three-neck flask and the mixture degassed under flowing

nitrogen for 30 min at 150°C for 30min. The mixture was then heated to 220°C for 1h for the formation of nanoparticles.

2. For $Cu_{12}Sb_4S_{13}$, 3.75mmol of copper(II) acetylacetonate, 1.25mmol of antimony(III) acetate, 3ml of 1-dodecanethiol and 3ml of oleylamine were dissolved in 24ml of 1-octadecene in a 250ml three-neck flask and the mixture degassed under flowing nitrogen for 30 min at 150°C for 30min. The mixture was then heated to 260°C for 1h for the formation of nanoparticles.
3. For $CuSbS_2$, 2mmol of copper(II) acetylacetonate, 2mmol of antimony(III) acetate, 3ml of 1-dodecanethiol and 3ml of oleylamine were dissolved in 24ml of 1-octadecene in a 250ml three-neck flask and the mixture degassed under flowing nitrogen for 30 min at 150°C for 30min. The mixture was then heated to 250°C for 1h for the formation of nanoparticles.

The resulting solutions are then topped up to 45ml with ethanol, sonicated and centrifuged at 10000rpm for 5 min. Then, the nanoparticles are centrifuged in ethanol for the removal of polar impurities. Subsequently, the nanoparticles are centrifuged three times with a hexane/ethanol mixture in 25:20, 15:30 and 5:40 ml ratios for the removal of organic impurities.

The $CuSbS_2$ powder is additionally immersed in 0.5M NaOH for 30min and centrifuged to etch Sb_2S_3 impurities, followed by centrifugation in deionized water to remove remaining NaOH.

Finally, the nanoparticles are centrifuged in isopropyl alcohol and dried in an oven at 70°C for an hour.

3.2.3.3 Chapter 6

- For Bi 0% sample, 3.75mmol of copper(II) acetylacetonate, 1.25mmol of antimony(III) acetate were used.
- For Bi 33% sample, 3.75mmol of copper(II) acetylacetonate, 0.417mmol of antimony(III) acetate and 0.833mmol of bismuth nitrate were used.

- For Bi 66% sample, 3.75mmol of copper(II) acetylacetonate, 0.833mmol of antimony(III) acetate and 0.417mmol of bismuth nitrate were used.

These salts were mixed in a three-neck flask and the nanoparticles were synthesized according to the heat-up procedure at 250°C for 1h as described in the methods chapter.

The Bi 100% sample was synthesized by solvothermal route. 4.5mmol of copper(II) chloride, 1.5mmol of bismuth nitrate were dissolved in 60ml of ethylenediamine. 10mmol of Thiourea was then added and dissolved and the mixture transferred to a Teflon-lined steel autoclave and heated to 180°C for 15h according to the solvothermal procedure as described in the methods chapter.

3.3 Electrochemical testing methods

Electrochemical testing methods include the electrochemical cell, the electrochemical workstation and the product analysis methods. These will be covered in the following subsections.

3.3.1 Gas diffusion electrode flow cell

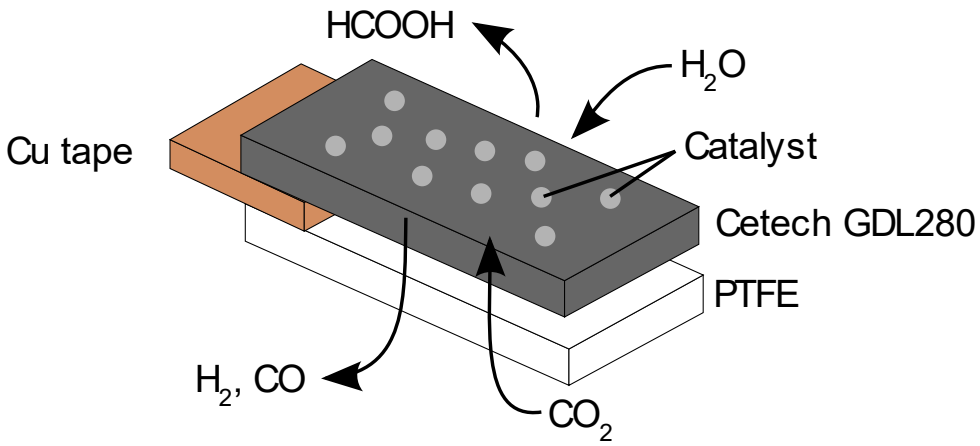

Figure 3.3: Schematic of gas diffusion electrode

27 mg of catalyst was dispersed in 2 mL of ethanol with 50 µL of Nafion ionomer solution (5%) and sonicated for 30 min. The prepared catalyst ink was then airbrushed with an airbrush gun (Paasche) onto a 6cm by 6cm CeTech (CT) GDL280 carbon paper.

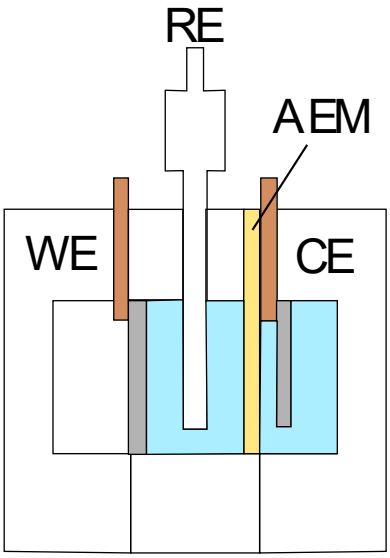

Figure 3.4: Schematic of three-compartment flow cell

The electrochemical measurements were carried out in a three-compartment flow cell, with an anion exchange membrane (Fumasep FAA-3-pk-130) and nickel foam clamped between the catholyte and anolyte compartments and carbon paper with catalyst ink clamped between the gas and catholyte compartments. The geometric area of the working electrode was 1cm2. The reference electrode placed in the catholyte compartment was an AgCl electrode filled with 3M KCl.

In electrochemical CO_2 reduction, three types of cells are commonly used: H-cell, flow cell and membrane electrolyte assembly (MEA).[1, 8] These differ on two points; whether the CO_2 gas is bubbled into the electrolyte (aqueous form) or supplied in gaseous form to the catalyst (via gas diffusion electrode), and whether the water is in liquid form or gaseous form. These can be summarized below:

Table 3.1: Comparison of H-cell, flow cell and MEA

	H-cell	**Flow cell**	**MEA**
Figure 3.5: Three kinds of electrochemical CO_2RR cell, taken from [1]. *No permission is required for thesis purposes.*	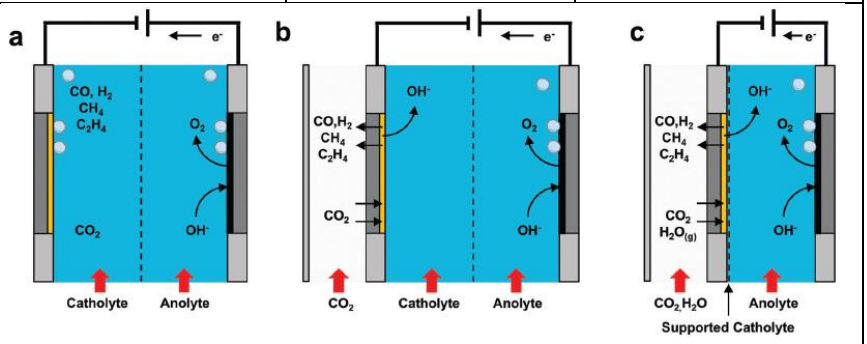		
CO_2 gas	Bubbled (aqueous)	Gaseous (GDE)	Gaseous (GDE)
Water	Liquid	Liquid	Gaseous or from anode

As the H-cell suffers from depletion of CO_2 at higher current densities, it is not desirable for electrochemical CO_2 reduction as most publications now test electrochemical CO_2RR at high current densities exceeding 100mA/cm2. While the MEA is the most advanced form of electrochemical CO_2 cell, there are difficulties associated when water is supplied in gaseous form (i.e. steam) or from the anode as the gas diffusion layer has to be tightly compressed against the ion exchange membrane for water to be supplied from the anode. As such, the flow cell was chosen for our experiments.

Electrochemical CO_2 reduction can be run in alkaline (KOH solution), slightly alkaline ($KHCO_3$ solution) or acidic (phosphate or sulfate solution). These provide different pH environments for the catalyst environment. While acidic solutions reduce bicarbonate formation on the gas diffusion layer and reduce CO_2 crossover to the anode, they typically enhance the competing hydrogen evolution reaction (HER).[9] At the other extreme, alkaline solutions suppress HER and methane formation, thus increasing electrochemical CO_2RR efficiency; however, excessively high alkalinity may inhibit CO formation and promote formate instead.[10] As $KHCO_3$ is the most commonly used electrolyte with good pH buffering capability for electrochemical CO_2 reduction,[11] it was chosen as the electrolyte for our study with its concentration fixed at 1M.

3.3.2 Chronoamperometry

Chronoamperometry experiments were carried out with an Autolab PGSTAT204.

Electrode measurements was first compensated for 80% of iR drop with solution resistance measured using electrochemical impedance spectroscopy (EIS). The resulting voltage was then converted to the RHE scale using the formula:

$$E_{RHE} = E_{Ag/AgCl} + 0.197 + 0.0591 \times pH$$

Here $E_{Ag/AgCl}$ is the working potential, ${E^0}_{Ag/gCl} = 0.197\text{V}$ is the standard potential of the Ag/AgCl reference electrode at 25°C vs SHE and $0.0591 \times pH$ is the pH dependent conversion between the SHE and RHE scales.

3.3.3 Gas flow control and gas products detection

An Alicat MC-100SCCM-D mass flow controller was used to control the flow of CO_2 to the gas inlet. A mass flow of 40sccm was used for all experiments. Gas products were quantified with a gas chromatograph (Shimadzu Nexis GC-2030) equipped with a thermal conductivity detector (TCD) and flame ionization detector (FID) with an optional methanizer setting.

The gas chromatograph consists of three key components: the carrier gas (in this case Argon), the column and the detector. First, the sample gas is injected into the carrier gas, and the resulting mixture then moves through the column. Different component gases in the sample, such as hydrogen, CO, etc move through the column at different rates due to the interaction forces between the column and the component gases. These gases then get detected by the detector at different times. A TCD is sensitive to all gases but only at higher concentrations as it measures the thermal conductivity change when gases pass through, while an FID more sensitive but can only detect hydrocarbon samples which can be burned in a hydrogen flame.[12] As such, for low concentrations of CO, a methanizer can be added before the FID to convert the CO to CH_4 to be detected by the FID.

3.3.4 Electrolyte flow control and liquid products detection

25ml of catholyte and 25ml of anolyte were used, pumped at a rate of 28.5ml/min. Liquid products were quantified with a liquid chromatograph (Shimadzu LC-2030) equipped with a UV detector and a refractive index detector (RID).

The liquid chromatograph consists of three key components: the mobile phase (in this case 2mM H_2SO_4), the stationary phase (column) and the detector. First, the sample liquid is injected into the mobile phase, and the resulting mixture then moves through the stationary phase. Different component liquids in the sample, such as $HCOO^-$, C_2H_5OH, etc move through the stationary phase at different rates due to the interaction forces between the stationary phase and the component liquids. These liquids then get detected by the detector at different times. An RID is sensitive to all liquids but only at higher concentrations as it measures the refractive index change when gases pass through, while a UV detector is more sensitive but can only detect UV-absorbent liquids.

3.3.5 Electrochemical impedance spectroscopy (EIS)

Electrochemical impedance spectroscopy was used to determine the solution resistance (R_S).

From Ohm's law, the resistance is obtained as a function of voltage and current:

$$R = \frac{V}{I}$$

However, this is only valid for an ideal resistor. The most commonly used model for an electrode in a real electrochemical cell is the simplified Randles cell. This includes two resistors and a capacitor in parallel to the charge transfer resistance (R_{ct}).

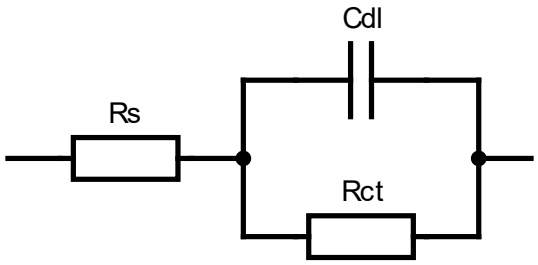

Figure 3.6: Circuit diagram of simplified Randles cell

The equivalent measure of "resistance" of such a circuit is the impedance (Z), which unlike resistance is a function of frequency of the voltage and current signals. In EIS, an AC voltage excitation signal is applied, which generates a current with the same frequency but with a phase shift when compared to the voltage signal:

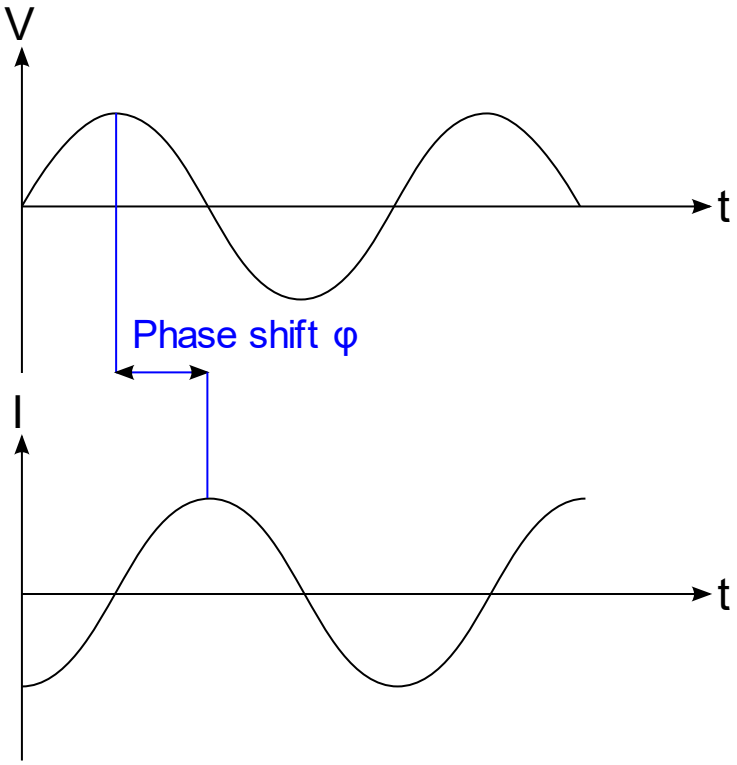

Figure 3.7: Phase shift of current with respect to voltage

The resulting impedance is a function of the voltage and current just like in Ohm's law:

$$Z = \frac{V_0 \sin(\omega t)}{I_0 \sin(\omega t + \varphi)} = Z_0 \frac{\sin(\omega t)}{\sin(\omega t + \varphi)}$$

Where V_0 and I_0 are the amplitudes of the voltage and current function respectively and ω is the frequency. As a result, the impedance has an magnitude (Z_0) and a phase shift (φ).

However, impedance actually has real and complex component, where the real component represents resistance and the complex component represents reactance which is related to the phase shift φ. To take this into account, impedance can be rewritten with real and complex components, using Euler's relationship:

$$Z = \frac{V_0 e^{j\omega t}}{I_0 e^{j(\omega t+\varphi)}} = \frac{V_0}{I_0} e^{j\varphi} = Z_0 e^{j\varphi} = Z' + Z''$$

The resulting Argand diagram is known as the Nyquist plot, which is a plot of Z'' against Z'. The Nyquist plot is a semicircle, where the high frequency Z'-intercept represents R_s. Other values such as R_{ct} and C_{dl} can be obtained as in the following figure:

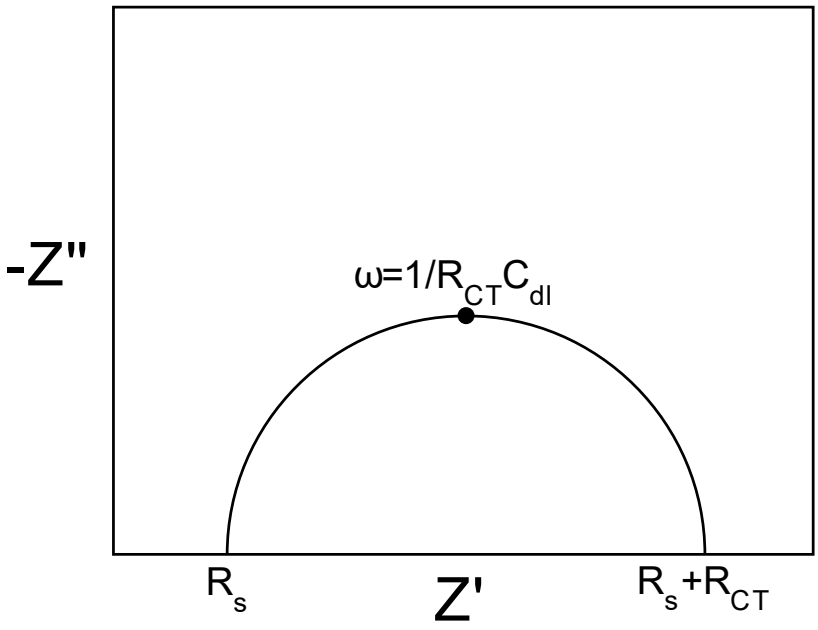

Figure 3.8: Nyquist plot for simplified Randles cell

3.3.6 Cyclic voltammetry (CV)

In cyclic voltammetry, a moving potential sweep is applied, which scans the potential range in one direction (cathodic or anodic), then reversed and scanned in the opposite direction. Typical cyclic voltammegrams (in this case scanned in the cathodic, then anodic direction) is as shown:

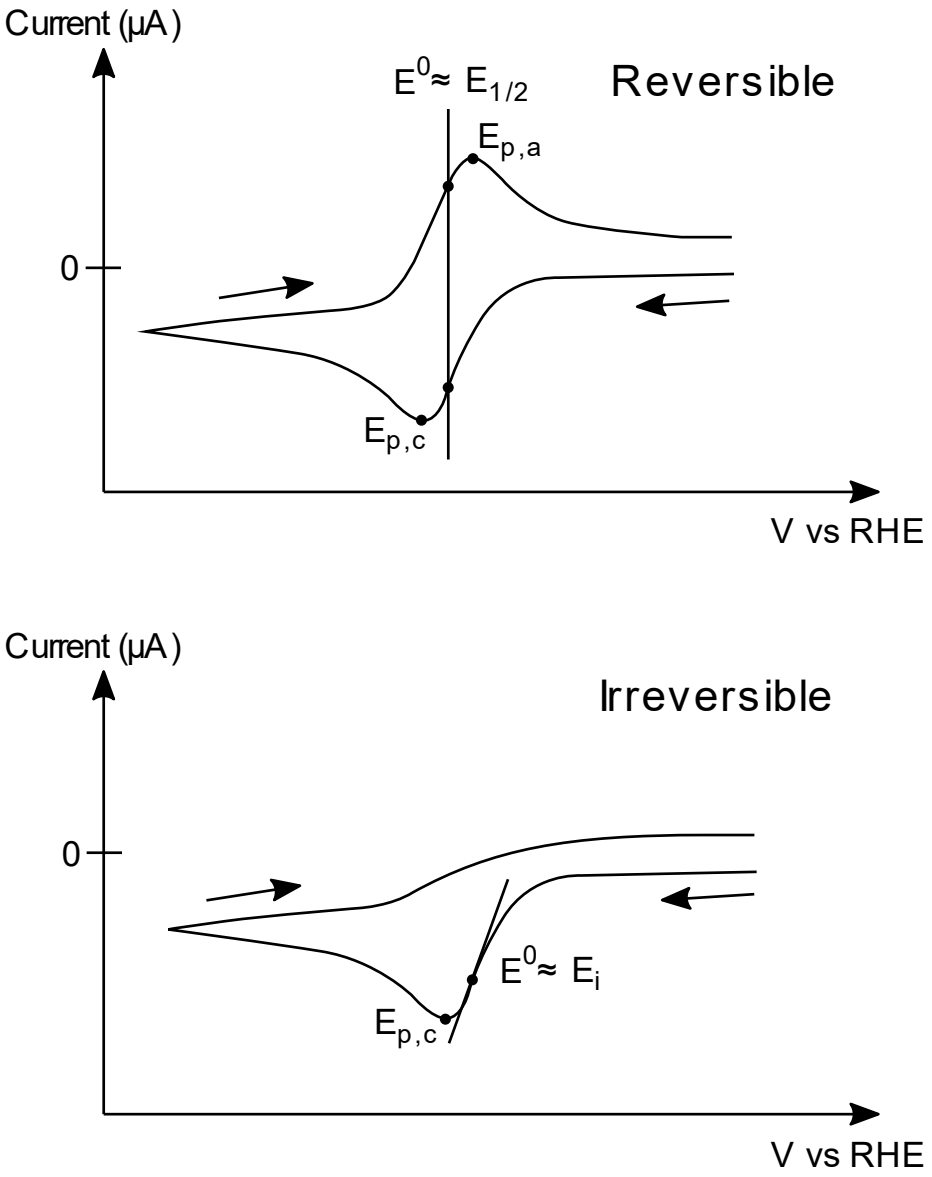

Figure 3.9: CVs for reversible and irreversible reactions

In the reversible case, as the potential is scanned towards the potential of a reversible electrochemical reaction, the current increases in the negative direction as the cathodic electrochemical reaction happens:

$$A^+ + e^- \rightarrow A$$

At the redox potential of the reaction E^0, the two species have equal concentration: $[A^+]=[A]$. Then, at the cathodic peak of the reaction, the current increases as the reaction proceeds faster, now limited by the diffusion rate of the reacting species. As the potential

is scanned towards even more cathodic potentials, the reaction slows down due to the diffusion rate limitation.

As the potential is scanned back in the anodic direction, the reverse reaction happens:

$$A \rightarrow A^{+} + e^{-}$$

Again, the two species have equal concentration at E^0, which reaches a peak as the reaction rate increases, followed by a decrease as diffusion rate limitations set in.

As can be seen, the redox potential does not occur at either of the peaks, unlike commonly assumed in certain papers. Instead, it occurs along the ascending portion of the peak. In the reversible case, this occurs at approximately the potential at midpoint of the two peaks, $E_{1/2}$. A similar consideration also applies in the irreversible case, where the reduction potential occurs approximately at the inflection point of the ascending portion of the peak, E_i. Reviews on CV for the reversible and irreversible cases have been provided by Elgrishi et al[13] and Espinoza et al[14] respectively.

3.4 Characterization methods

3.4.1 XRD

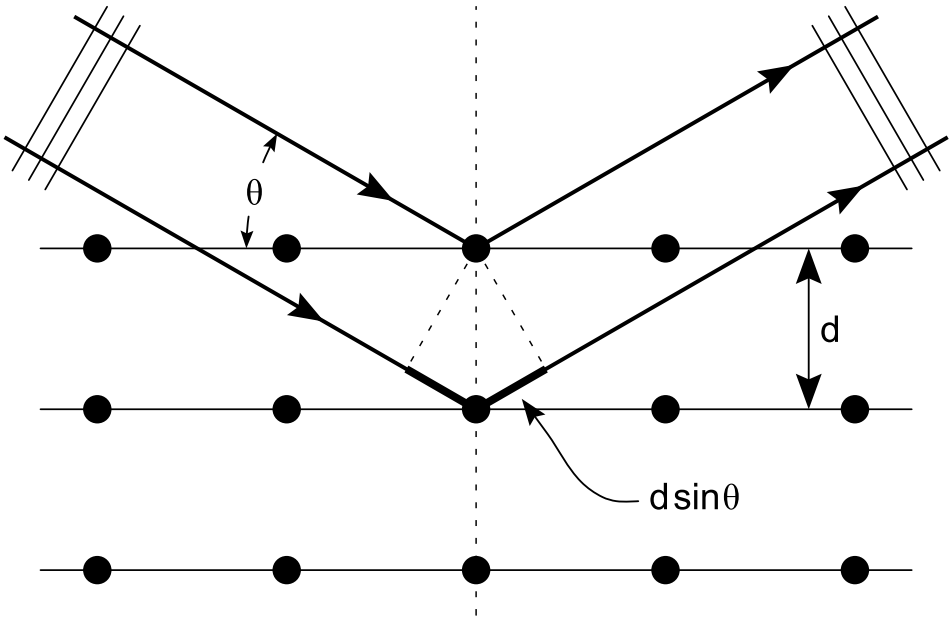

Figure 3.10: Crystal lattice and Bragg's law (Image taken from Wikipedia)

X-ray diffraction (XRD) works by using the crystal of the material as a diffraction grating. This is possible because the wavelength of the incoming X-rays are within the same order of magnitude as the interplanar lattice spacing of the crystal. When monochromatic X-ray beam hits the sample, the X-rays are reflected and the outgoing x-rays interfere. Constructive (in-phase) interference of the outgoing X-rays by an integer factor of the wavelength create constructive interference, giving rise to characteristic peaks in the XRD pattern. The incident angle where these peaks form are related to the spacing of the crystallographic planes by Bragg's Law:

$$2\mathrm{d}\ \sin\theta\ =\ \mathrm{n}\lambda, \mathrm{n}\ =\ 1, 2, 3, \ldots$$

Where d is the interplanar lattice spacing, θ is the incident angle of the X-rays and λ is the wavelength of the X-ray.

As the symmetry of the crystal decreases, the number of symmetrically distinct planes increases (more distinct values of d), resulting in a larger number of peaks seen in the XRD pattern. Every material has a unique characteristic XRD pattern by virtue of the unique interplanar spacings. In this report, the data were collected using a Panalytical X'Pert Pro with Cu-Kα radiation operated at 40kV and 30mA.

3.4.2 FE-SEM

In field emission scanning electron microscopy (FE-SEM), the electrons serve as the probing medium for high-resolution image. The use of electrons, which have the wavelength $\lambda = \frac{h}{mv}$ by the de Broglie equation, results in magnifications that can go as high as a few hundreds of thousands (100,000x). This is due to the much smaller wavelength of electrons in an SEM compared to visible light.

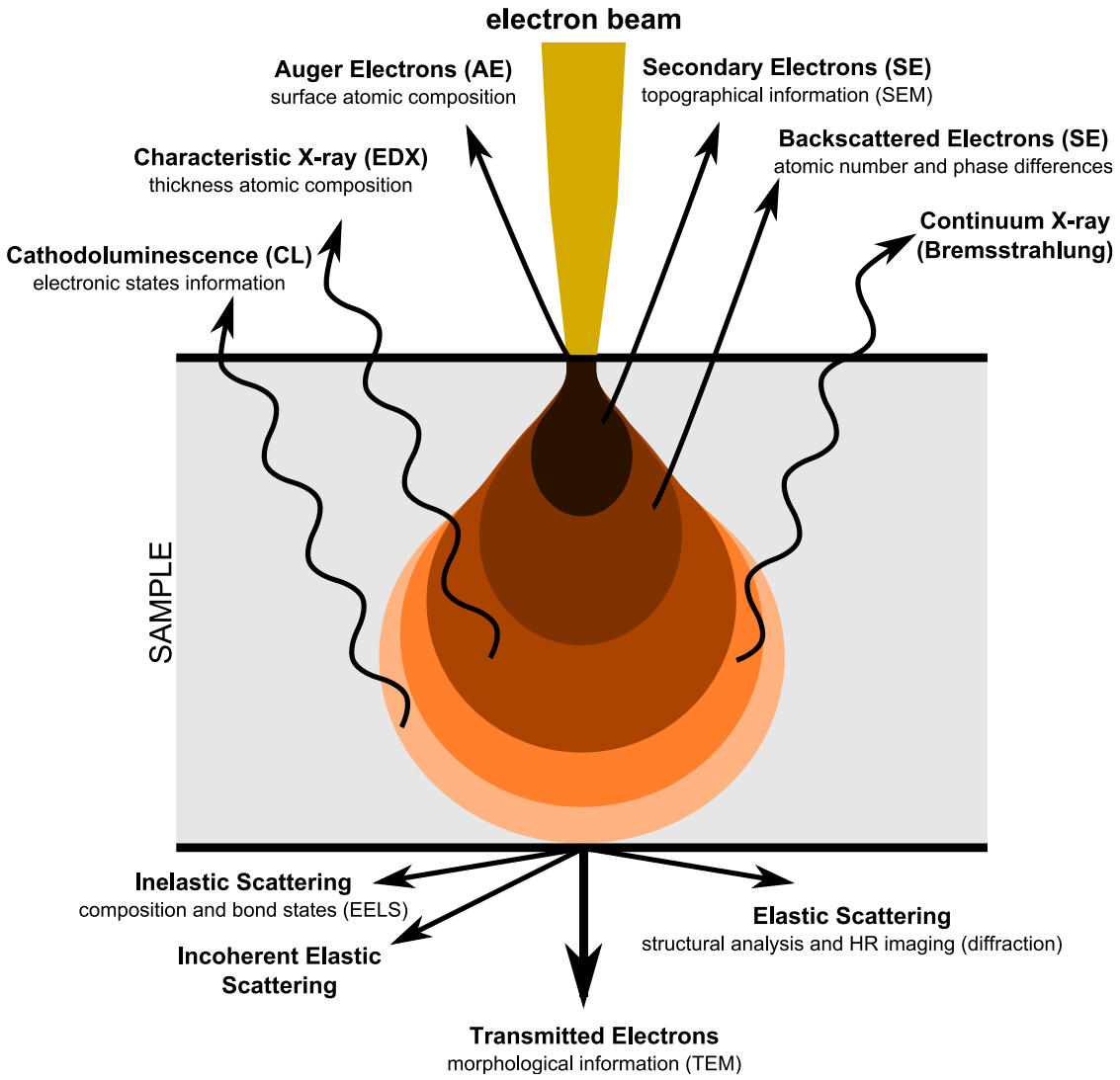

Figure 3.11: Electron interaction with matter (Image taken from Wikipedia)

As the electron beam is scanned across the sample, several types of images can be obtained. The secondary electron image can be obtained from electrons that are ejected from the surface of the sample and it is used to obtain surface morphology. The backscattered electron image is obtained when the incoming electrons are scattered back upwards by the nuclei of the sample when a higher accelerating voltage is used, and gives information about the phase composition of the sample. The X-rays that are emitted when an electron in a higher energy orbital relaxes into the vacancy formed by a knocked-out electron are used in Energy-Dispersive X-ray spectroscopy (EDX) to obtain elemental composition of the sample.

The SEM images used in this report are taken from a JEOL JSM-7600F.

3.4.3 TEM

Transmission electron microscopy (TEM) is the next step up in electron microscopy above FE-SEM, where the electrons are accelerated with higher energy (100-300kV as opposed to 0-30kV for FE-SEM) through a very thin (<100nm) sample, which results in electrons passing through the sample while interacting with it, giving crucial information about the atomic arrangement in the sample. This can show the crystal grain size, existence of amorphous regions in the sample and even the measurement of the d-spacing of the crystals by using fast-fourier transform (FFT) and its inverse to obtain clean lattice fringes for measurement.

Furthermore, selected area electron diffraction (SAED) can be performed on the sample which gives information similar to XRD, but on a specific region of the sample. This is because the de Broglie wavelength of electrons at the high accelerating voltage of the TEM is smaller than the interatomic spacing, resulting in electrons being diffracted by the crystal lattice which acts as a diffraction grating. As samples are commonly composed of many crystals in different orientations, this results in a ring diffraction pattern which can then be analyzed to get the phases and d-spacings of crystallites in the sample.

TEM analysis can be of particular importance in relating the catalyst morphology to its performance. It can reveal the origin of increased surface area, and in the case of catalyst reconstruction, in-situ TEM can show the evolution of the catalyst that results in increased surface area.[15, 16]

In this report, transmission electron microscopy (TEM) was carried out using a JEOL 2100F.

3.4.4 EDX

In Energy-dispersive X-ray spectroscopy (EDX), electrons from the SEM are used to knock out electrons from the core levels of the atoms. This creates a vacancy, which can be filled by an electron in a higher energy level:

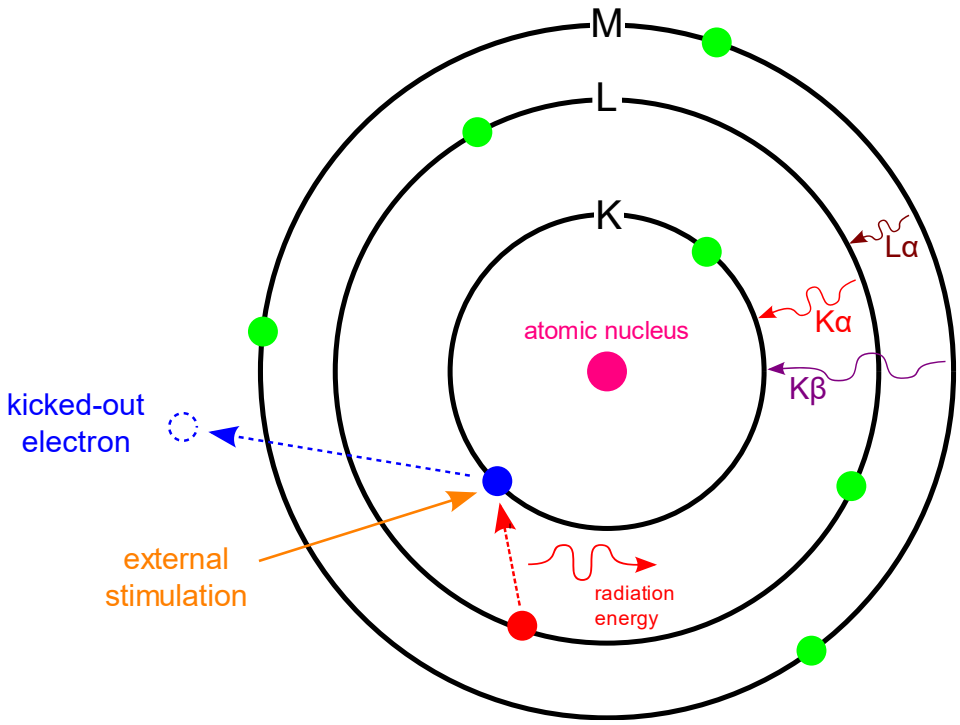

Figure 3.12: X-rays from electronic transitions (Image taken from Wikipedia)

As the energy gap between the two energy levels are discrete, this results in X-rays being emitted having characteristic energies which correspond to the difference between the higher and lower energy levels when the electron relaxes. These characteristic energies are specific to the elements in question, which is why EDX is used to probe elemental composition of the sample. EDX is a bulk (1-3µm) characterization technique.

In this report, EDX analysis was carried out using a JEOL JSM-7600F equipped with an INCA - XAct 10mm^2 X-ray detector.

3.4.5 XPS

X-ray photoelectron spectroscopy (XPS) relies on the photoelectric effect and the characteristic binding energy levels of the atoms to identify the elements and oxidation

state. As only photogenerated electrons from the surface layer can escape to be detected, XPS is a surface (1-10nm) characterization technique.

In XPS, the surface of the material is irradiated with a monochromatic X-ray beam. This causes electrons to be photoemitted with a specific kinetic energy. The relationship between the binding energy, incoming X-ray photon energy and the kinetic energy are given below:

$$E_{binding} = hf - E_{kinetic} - \varphi$$

Where hf is the energy of the incident photon and φ is the work function of the material, which is the energy loss when the photoelectron leaves the surface of the material and can be corrected by the XPS instrument. The instrument detects the kinetic energy of the photoelectron and, after correcting for the work function and substituting the known incident photon energy, outputs the binding energy spectrum of the electrons. The binding energies which correspond to the detected photoelectron binding energies of the material show up as peaks.

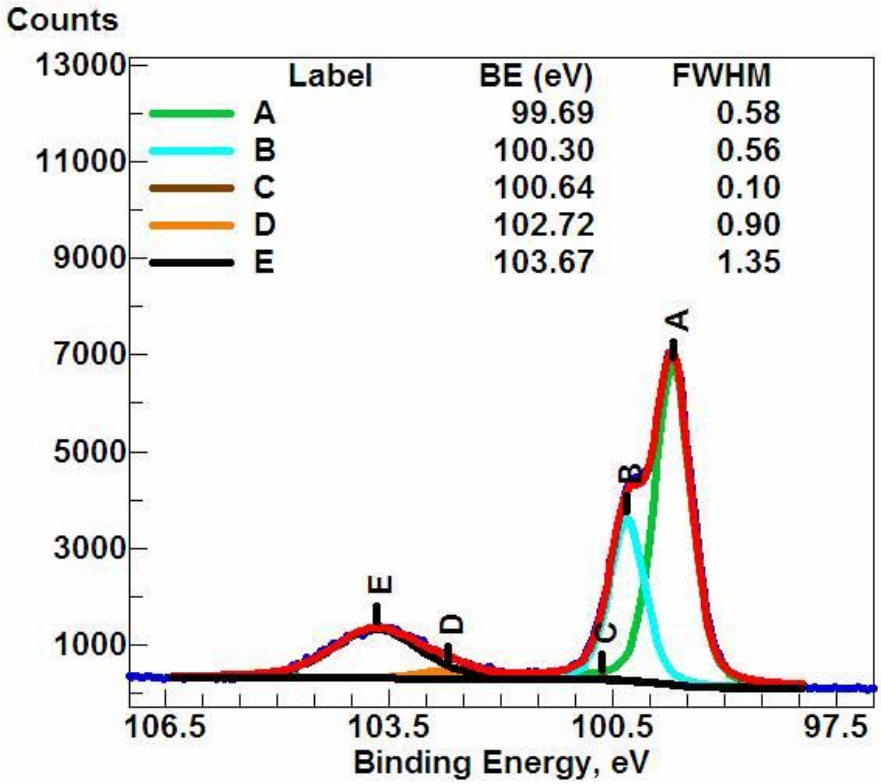

Figure 3.13: XPS example spectrum (Image taken from Wikipedia)

The binding energy of the electron is determined by the electron orbital of the element as well as its chemical environment. In an electron-withdrawing environment or higher oxidation state, the atom acquires a positive charge which makes the pull of the nucleus on the electrons stronger, resulting in higher binding energies. In an electron-donating environment or lower oxidation state, the reverse happens. This results in a complicated peak structure for each elemental orbital which can be deconvoluted by simulation into smaller peaks which represent the specific functional groups or oxidation states of the element on the material.

In this report, the data were collected using a Kratos AXIS Supra.

References

[1] T. Burdyny and W. A. Smith, "CO2 reduction on gas-diffusion electrodes and why catalytic performance must be assessed at commercially-relevant conditions," *Energy & Environmental Science,* 10.1039/C8EE03134G vol. 12, no. 5, pp. 1442-1453, 2019, doi: 10.1039/C8EE03134G.

[2] G. Demazeau, "Review. Solvothermal Processes: Definition, Key Factors Governing the Involved Chemical Reactions and New Trends," *Zeitschrift für Naturforschung B,* vol. 65, no. 8, pp. 999-1006, 2010, doi: doi:10.1515/znb-2010-0805.

[3] F. Long *et al.*, "Solvothermal synthesis, nanocrystal print and photoelectrochemical properties of CuInS2 thin film," *Materials Letters,* vol. 64, no. 2, pp. 195-198, 2010/01/31/ 2010, doi: https://doi.org/10.1016/j.matlet.2009.10.044.

[4] J. C. W. Ho *et al.*, "Optical and Electrical Properties of Wurtzite Copper Indium Sulfide Nanoflakes," *Materials Express,* vol. 2, no. 4, pp. 344-350, // 2012, doi: 10.1166/mex.2012.1091.

[5] S. G. Kwon and T. Hyeon, "Formation Mechanisms of Uniform Nanocrystals via Hot-Injection and Heat-Up Methods," *Small,* vol. 7, no. 19, pp. 2685-2702, 2011, doi: https://doi-org.remotexs.ntu.edu.sg/10.1002/smll.201002022.

[6] C. de Mello Donegá, P. Liljeroth, and D. Vanmaekelbergh, "Physicochemical Evaluation of the Hot-Injection Method, a Synthesis Route for Monodisperse Nanocrystals," *Small,* vol. 1, no. 12, pp. 1152-1162, 2005, doi: https://doi.org/10.1002/smll.200500239.

[7] K. Ramasamy, H. Sims, W. H. Butler, and A. Gupta, "Selective Nanocrystal Synthesis and Calculated Electronic Structure of All Four Phases of Copper–Antimony–Sulfide," *Chemistry of Materials,* vol. 26, no. 9, pp. 2891-2899, 2014/05/13 2014, doi: 10.1021/cm5005642.

[8] D. M. Weekes, D. A. Salvatore, A. Reyes, A. Huang, and C. P. Berlinguette, "Electrolytic CO2 Reduction in a Flow Cell," *Accounts of Chemical Research,* vol. 51, no. 4, pp. 910-918, 2018/04/17 2018, doi: 10.1021/acs.accounts.8b00010.

[9] Y. Xie *et al.*, "High carbon utilization in CO2 reduction to multi-carbon products in acidic media," *Nature Catalysis,* vol. 5, no. 6, pp. 564-570, 2022/06/01 2022, doi: 10.1038/s41929-022-00788-1.

[10] A. S. Varela, "The importance of pH in controlling the selectivity of the electrochemical CO2 reduction," *Current Opinion in Green and Sustainable Chemistry,* vol. 26, p. 100371, 2020/12/01/ 2020, doi: https://doi.org/10.1016/j.cogsc.2020.100371.

[11] G. Marcandalli, M. C. O. Monteiro, A. Goyal, and M. T. M. Koper, "Electrolyte Effects on CO2 Electrochemical Reduction to CO," *Accounts of Chemical Research,* vol. 55, no. 14, pp. 1900-1911, 2022/07/19 2022, doi: 10.1021/acs.accounts.2c00080.

[12] J. E. Pander Iii, D. Ren, and B. S. Yeo, "Practices for the collection and reporting of electrocatalytic performance and mechanistic information for the CO2 reduction reaction," *Catalysis Science & Technology,* 10.1039/C7CY01785E vol. 7, no. 24, pp. 5820-5832, 2017, doi: 10.1039/C7CY01785E.

[13] N. Elgrishi, K. J. Rountree, B. D. McCarthy, E. S. Rountree, T. T. Eisenhart, and J. L. Dempsey, "A Practical Beginner's Guide to Cyclic Voltammetry," *Journal of Chemical Education,* vol. 95, no. 2, pp. 197-206, 2018/02/13 2018, doi: 10.1021/acs.jchemed.7b00361.

[14] E. M. Espinoza, J. A. Clark, J. Soliman, J. B. Derr, M. Morales, and V. I. Vullev, "Practical Aspects of Cyclic Voltammetry: How to Estimate Reduction Potentials When Irreversibility Prevails," *Journal of The Electrochemical Society,* vol. 166, no. 5, pp. H3175-H3187, 2019, doi: 10.1149/2.0241905jes.

[15] C. W. Li, J. Ciston, and M. W. Kanan, "Electroreduction of carbon monoxide to liquid fuel on oxide-derived nanocrystalline copper," *Nature,* vol. 508, no. 7497, pp. 504-507, 2014/04/01 2014, doi: 10.1038/nature13249.

[16] X. Wang *et al.*, "Morphology and mechanism of highly selective Cu(II) oxide nanosheet catalysts for carbon dioxide electroreduction," *Nature Communications,* vol. 12, no. 1, p. 794, 2021/02/04 2021, doi: 10.1038/s41467-021-20961-7.

Chapter 4 Investigation on Cu-M-S as catalyst for CO_2 reduction

In this chapter, Cu-M-S with nine metals M=In, Sn, Sb, Bi, Ga, Ge, Ag, Co, Fe are screened to identify a sulfide-derived catalyst that has high selectivity for electrochemical CO_2 reduction. It is found that Cu-Sb-S produces CO with Faradaic efficiency of above 70%. Some of the catalysts (where M=Sb, Bi, Ag) reduce in the presence of applied voltage, while most of the other catalysts do not. Cu-Sb-S/Se sulfoselenide is then synthesized and its electrochemical CO_2 reduction behaviour measured. It is found that the sulfoselenide Cu-Sb-S/Se produces more H_2 than the sulfide Cu-Sb-S, but the electrochemical CO_2 performances are otherwise very similar. This chapter concludes with Cu-Sb-S as worthy of further study.

4.1 Introduction

As discussed in chapters 1 and 2, copper bimetallic chalcogenides (Cu-M-S) are potential candidates for CO_2RR. Several studies have reported the activity of copper bimetallic alloys, such as the work of Takanabe and co-workers, who reported both Cu-In and Cu-Sn catalysts to be selective for electrochemical CO_2 reduction to CO.[1, 2] Copper sulfide-derived catalysts has also been reported, such as the work by Perez-Ramirez and co-workers who demonstrated its selectivity for electrochemical CO_2 reduction to $HCOO^-$.[3] Given the different selectivity behaviour of Cu-In, Cu-Sn and possibly other copper-based catalysts toward CO, there is a possibility that sulfur can improve their selectivity according to the covalency-aided mechanism outlined by Kim and co-workers.[4] Hence, Cu-M-S derived catalysts could be a good strategy to improve the selectivity of CO or reduced products. Given the lack of studies in this area, screening of second metal is warranted to explore the materials space.

The choice of second metal is crucial to control the selectivity. Generally, (In, Sn, Sb) alloys with Cu all produce CO as their major product.[1, 2, 5] Other choices of second metal are also included to expand the screening to candidates that have the possibility of producing reduced products. (Ga, Ge) if added in minute amounts to form an alloy with Cu it may be able to promote reduced products.[6] Ag is also very frequently reported in literature in “alloys” with Cu (although it is strictly speaking eutectic with Cu on the phase diagram).[7] (Fe, Co) are rarely reported in literature as they mainly produce H_2, but some reports suggest a slight increase in methane selectivity.[8] Nonetheless, in this chapter sulfide-derived materials from all three of these categories are considered in testing their CO_2 reduction behaviour. Bi mixes with Cu to produce $HCOO^-$.[9] This was detailed in Chapter 2.

Chalcogenides (sulfides and selenides) have been reported to contribute to CO_2 reduction selectivities in different ways. Perez-Ramirez and co-workers tested both copper sulfide-derived and copper selenide-derived catalyst in their work.[10] While both produced mainly $HCOO^-$, the selenide demonstrated increased H_2 and CO production. In contrast, He et al tested CdS/Se system, and found that CdS produces CO but CdSe produces H_2.[11]

The two contrasting studies, with copper chalcogenide-derived catalysts promoting HCOOH while CdS/Se catalysts producing CO, could be due to contrasting mechanisms of promoting *H binding for $HCOO^-$ or *COOH binding for CO via the covalency-aided mechanism. The covalency-aided mechanism could result in improvement of CO selectivity.

In this chapter, Cu-M-S with 9 metals M=(In, Sn, Sb, Bi, Ga, Ge, Ag, Co, Fe) were tested. The best performing sulfide-derived catalyst(s) are then selected and tested by replacing some sulfur with selenium. This way, the ternary chalcogenide-derived category is screened to find catalysts with surprising selectivities or otherwise elucidate trends in reduction behaviour and selectivity.

4.2 Second metal trials results and discussion

4.2.1 Crystal structure of Cu-M-S

4.2.1.1 Chalcopyrite phases

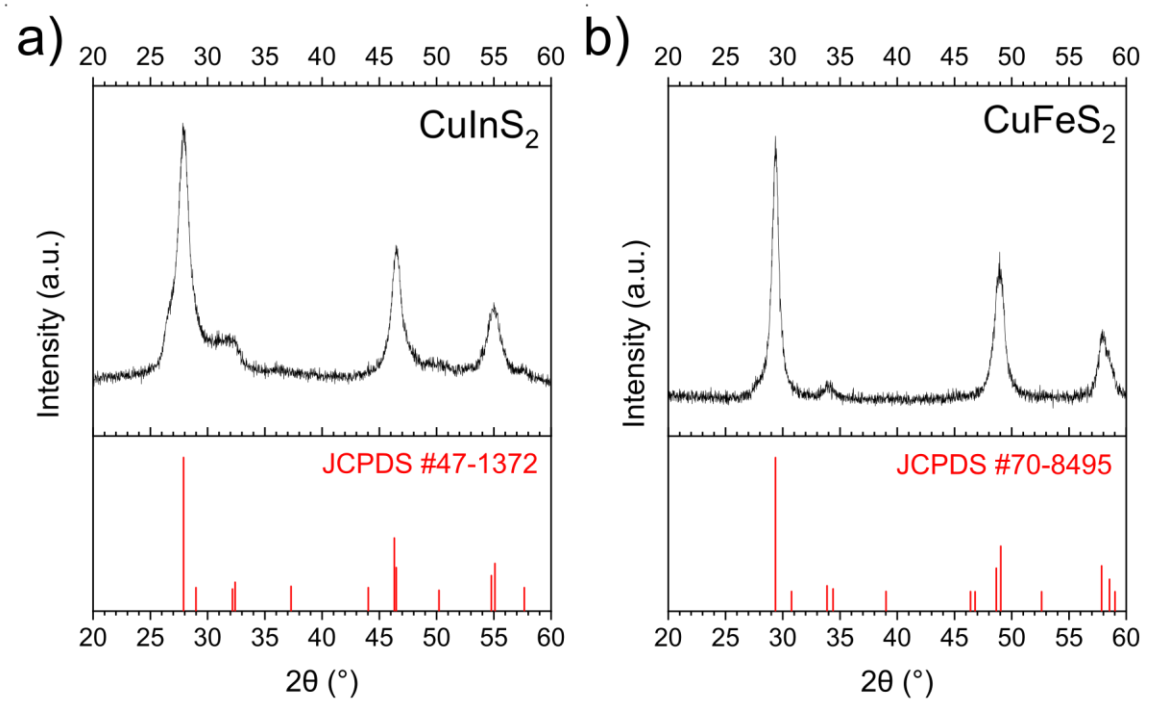

Figure 4.1: XRD of synthesized powder samples $CuInS_2$ and $CuFeS_2$

$CuInS_2$ was prepared by solvothermal synthesis in ethylene glycol and $CuFeS_2$ was

prepared by heat-up method. As shown in Figure 4.1, both sulfides exhibited a pure chalcopyrite (zinc blende-derived) structure with three characteristic peaks at approximately 28°, 46° and 55°. The produced sulfide does not exhibit any prominent impurities in the XRD structure.

4.2.1.2 Zinc blende-derived phases and Wurtzite phases

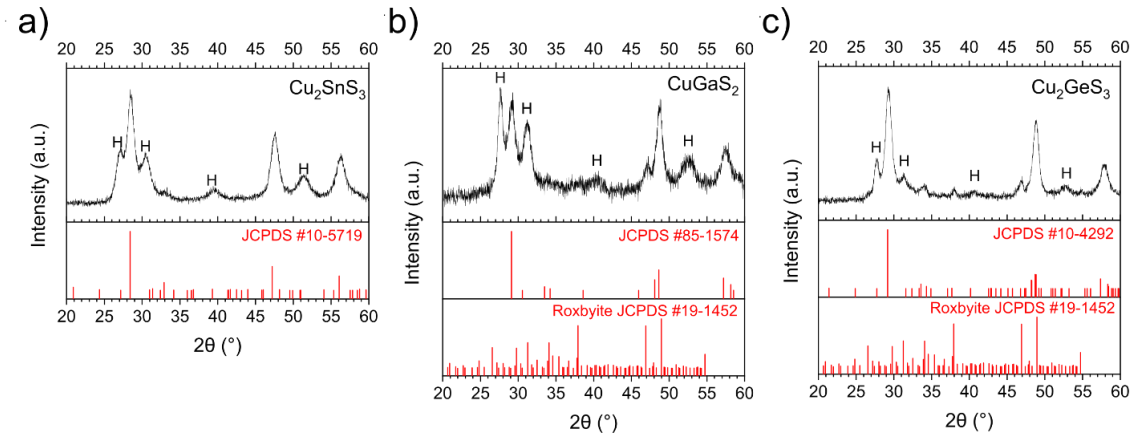

Figure 4.2: XRD of synthesized powder samples (a) Cu_2SnS_3, (b) $CuGaS_2$ and (c) Cu_2GeS_3. H refers to the additional wurtzite peaks not found in the zinc blende-derived structures.

As Cu_2SnS_3, $CuGaS_2$ and Cu_2GeS_3 were produced using the heat-up method with dodecanethiol as both sulfur source and structure-directing agent, the synthesized sulfides are a mixture of zinc blende-derived and wurtzite structures (as dodecanethiol prefers hexagonal structure), where there are four additional wurtzite peaks labelled as H in the XRD graphs in Figure 4.2. Other than this mixture, Cu_2SnS_3 appears to be pure, while $CuGaS_2$ and Cu_2Ge_3 show additional Cu_xS roxbyite (again a hexagonal structure) impurity.

4.2.1.3 Table of phases

The zinc blende-derived and wurtzite structures found in the XRDs are tabulated in Table 4.1:

Table 4.1: Crystal structures derived from zinc blende and wurtzite that were found in the XRD images. Images for cubic, tetragonal and hexagonal were obtained from Wikipedia.

	Zinc blende	**Zinc blende-derived**		**Wurtzite**
	Cubic	**Tetragonal (chalcopyrite)**	**Monoclinic**	**Hexagonal**
Image	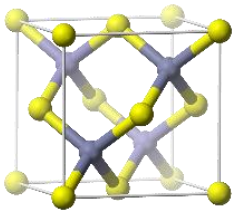	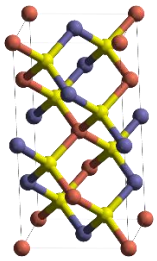	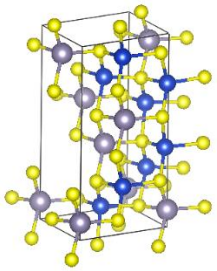	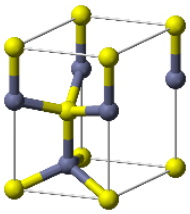
$CuInS_2$		Y	N	N
$CuFeS_2$		Y	N	N
Cu_2SnS_3		N	Y	Y
$CuGaS_2$		Y	N	Y
Cu_2GeS_3		N	Y	Y

4.2.1.4 Other phases

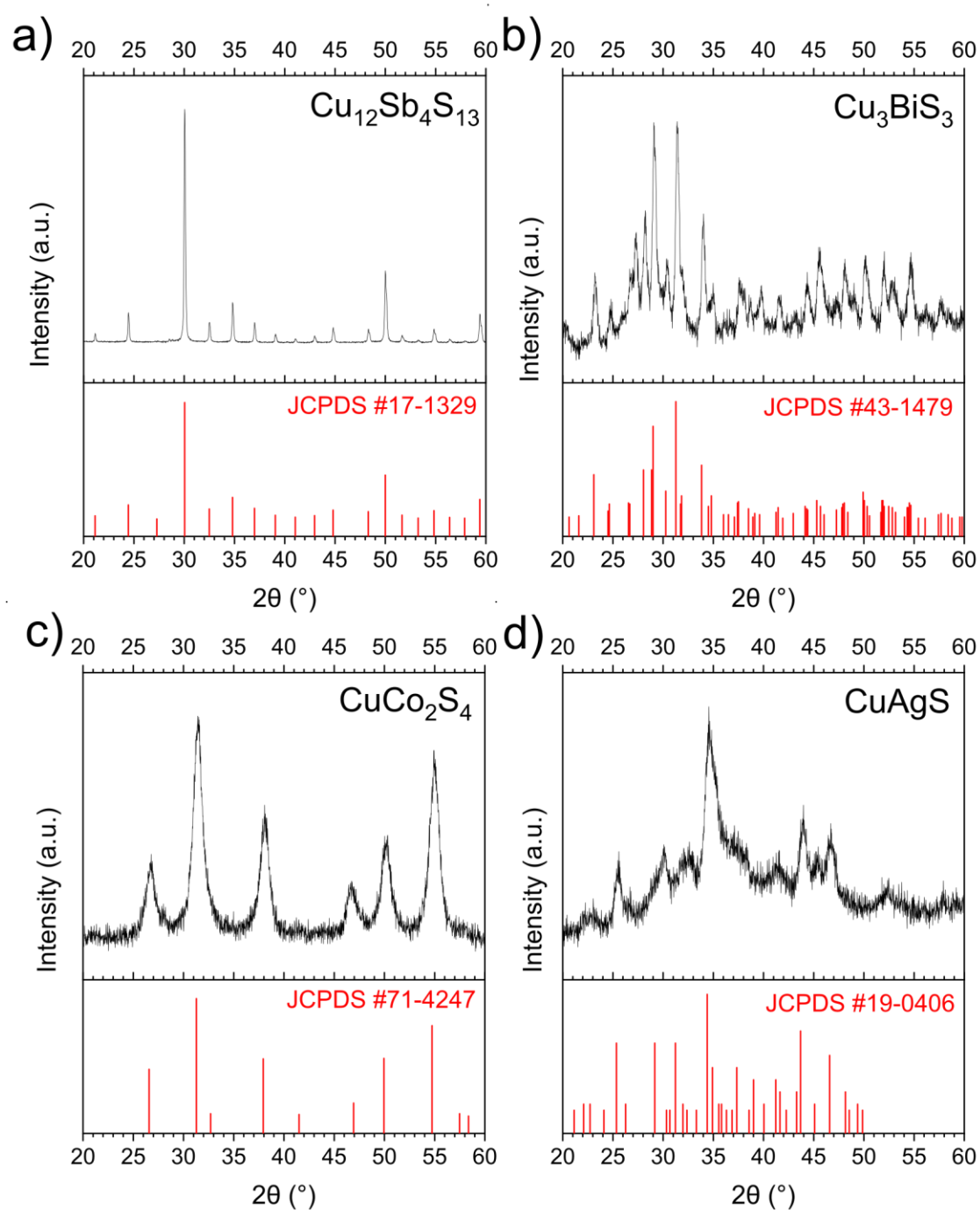

Figure 4.3: XRD of synthesized powder samples (a) $Cu_{12}Sb_4S_{13}$, (b) Cu_3BiS_3, (c) $CuCo_2S_4$ and (d) CuAgS

In Figure 4.3, $Cu_{12}Sb_4S_{13}$, Cu_3BiS_3, $CuCo_2S_4$ and CuAgS, unlike the other sulfides discussed so far, do not adopt zinc blende-derived nor wurtzite-derived phases and have unique structures of their own. All four of them appear to be pure phase. Cu-Sb-S nonetheless does also seem exhibit a cubic-hexagonal duality, with $Cu_{12}Sb_4S_{13}$ (tetrahedrite)

being of the cubic-derived type and Cu_3SbS_3 (skinnerite) being of the hexagonal-derived type (distorted into orthorhombic), but with a different bonding pattern than zinc blende or wurtzite which thus confers them more complicated XRD patterns.

4.2.2 CO_2RR reduction behaviour

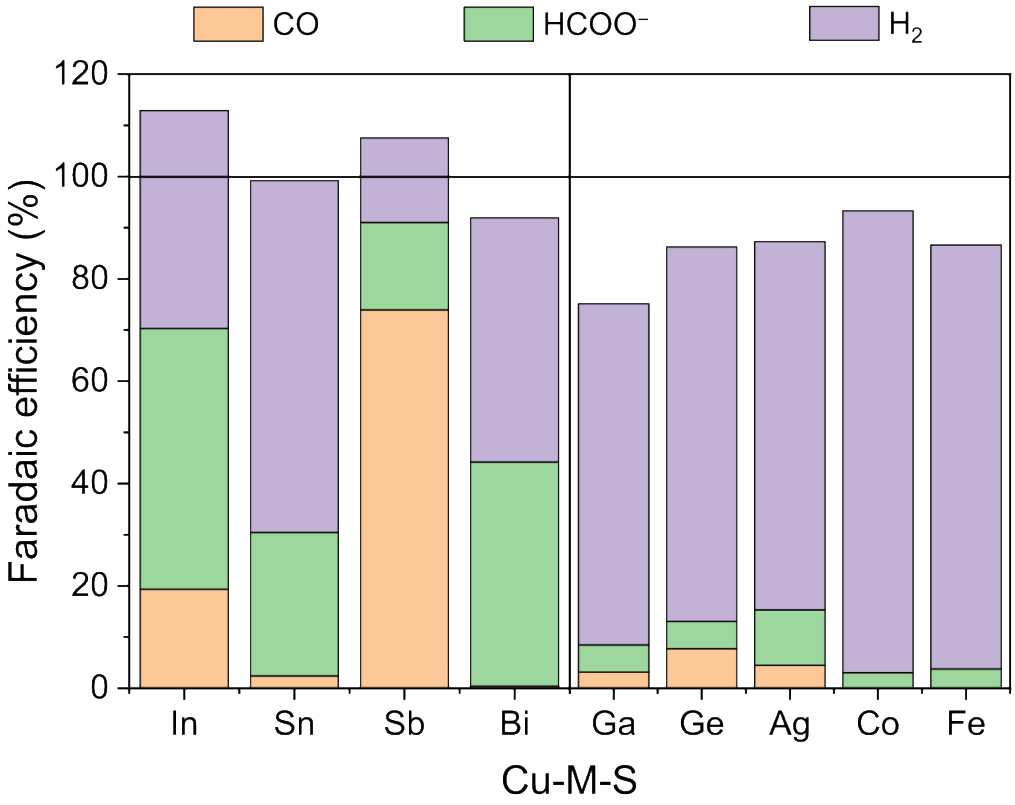

Figure 4.4: Electrochemical CO_2 reduction behaviour of the nine Cu-M-S samples

As can be seen in Figure 4.4, the results can be split into two sets. The first set is (In, Sn, Sb, Bi) which produce either $HCOO^-$ or CO and the second set is (Ga, Ge, Ag, Co, Fe) which produce nearly entirely H_2. As Cu-In, Cu-Sn and Cu-Sb alloys (without sulfur) all produce CO as their major product, the fact that Cu-In-S and Cu-Sn-S do not, hints at a difference in their sulfides that cause this change in behavour. H_2 and $HCOO^-$ were the major products on Cu-In-S and Cu-Sn-S (Figure 4.4), while CO was mainly observed on Cu-Sb-S.

4.2.3 Catalyst reduction

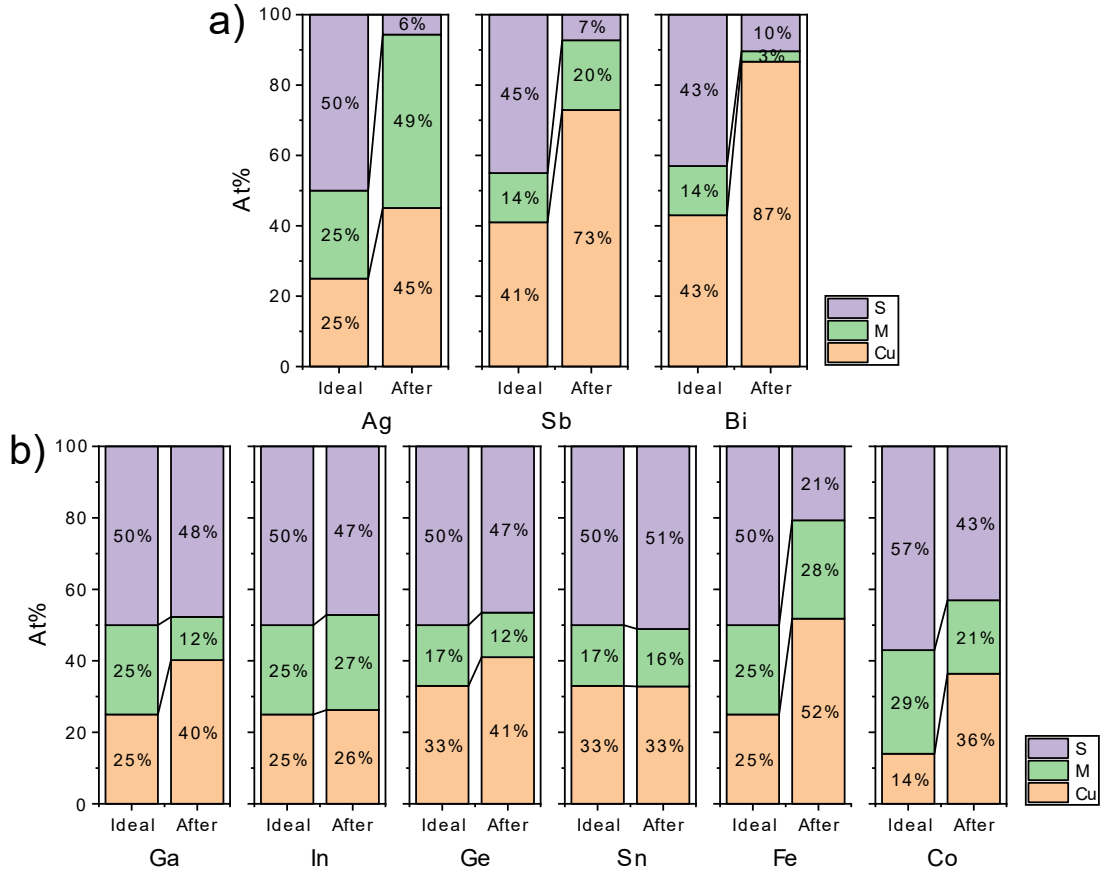

Figure 4.5: EDX plot of the nine Cu-M-S samples (a) Samples where the sulfide reduced (b) Samples where the sulfide did not reduce or reduced partially

As can be seen in Figure 4.5, these can be split into two categories. Cu-M-S with M elements in Groups 11 and 15 (Cu-Ag-S, Cu-Sb-S and Cu-Bi-S) experience a reduction of the parent sulfide with most of the sulfur becoming removed, while all other samples Cu-(Ga, In, Ge, Sn, Fe, Co)-S exhibit either no reduction or partial reduction of the sulfide. Comparing with post-reduction XRD in Figure A.1, Cu-Sb-S and Cu-Bi-S show reduction to an amorphous Cu-like phase with a broad hump at 41-47°, Cu-Ge-S retains its parent phase but has some Cu formation, while Cu-In-S, Cu-Sn-S and Cu-Co-S largely retain their parent sulfide phases.

It can be seen that for the sulfides that reduce, the main product can be H_2, CO or $HCOO^-$. However, for the sulfides that do not reduce or reduce partially, H_2 and $HCOO^-$ are the

main products. It is thus likely that CO is suppressed to some degree in the presence of excess sulfur, while $HCOO^-$ can be promoted in the presence of excess sulfur which corroborates with existing literature where CuS_x is tuned away from CO (and C_{2+} products) to $HCOO^-$ due to the presence of sulfur as compared to Cu.[3, 12, 13]

4.2.4 Comparison with literature

There is a difference in behaviour of these sulfide-derived catalysts with respect to CuS_x. While the amount of remnant sulfur in CuS_x is small, on the order of 1-10%, the product selectivity has been seen to be tuned completely away from CO and reduced products towards $HCOO^-$.[3] This is in contrast to the Cu-In-S-derived catalyst, where even with most of the sulfur remaining it is still able to achieve about 20% Faradaic efficiency of CO. Moreover, Cu-Sb-S-derived catalyst is able to achieve about 75% Faradaic efficiency for CO with similar levels of sulfur (about 7%) as CuS_x catalysts. Thus, the sensitivity of these bimetallic sulfide-derived catalysts to sulfur seems to be lower than for copper sulfide-derived catalysts. The lower selectivity of Cu-In-S compared to Cu-Sb-S could very well be due to the non-reduction of the former sulfide vs the reduction of the latter, but more work needs to be done to probe the surface of Cu-In-S via XPS to determine the amount of sulfur that remains on the surface. It is possible that while sulfur remains in the bulk (as measured by EDX), it may be relatively lower on the surface (which can be measured by XPS).

In all of these catalysts, because the main group element does not bind well with carbon, copper acts as the main active sites for CO_2 reduction to CO. Thus, it is remarkable that CO can be produced as the only other sulfide-derived catalyst with substantial and replicable CO selectivity is CdS.[11, 14]

Comparing the post-reduction EDX results to the standard reduction potentials of the second metal elements[15] (Notes: SbO^+ is taken because Sb^{3+} data is unavailable. Co is omitted as the oxidation state of Co in thiospinel $CuCo_2S_4$ is +2.5[16]. Cu is included in the list because it is present in Cu-M-S):

- $Ga^{3+} + 3e^- \rightleftharpoons \mathrm{Ga(s)}$: -0.549V

- $In^{3+} + 3e^- \rightleftharpoons \mathrm{In(s)}$: -0.338V
- $Fe^{3+} + 3e^- \rightleftharpoons \mathrm{Fe(s)}$: -0.037V
- $Sn^{4+} + 4e^- \rightleftharpoons \mathrm{Sn(s)}$: 0.021V
- $Ge^{4+} + 4e^- \rightleftharpoons \mathrm{Ge(s)}$: 0.124V
- $SbO^+ + 2H^+ + 3e^- \rightleftharpoons \mathrm{Sb(s)} + H_2O$: 0.2V
- $Bi^{3+} + 3e^- \rightleftharpoons \mathrm{Bi(s)}$: 0.308V
- $Cu^+ + e^- \rightleftharpoons \mathrm{Cu(s)}$: 0.521V
- $Ag^+ + e^- \rightleftharpoons \mathrm{Ag(s)}$: 0.799V

It can be seen that the second elements that result in the reduction of the parent bimetallic sulfides (Sb, Bi, Ag), have more positive reduction potentials than the ones that do not reduce (Ga, In, Fe, Sn, Ge), which is consistent with the post-reduction EDX results. The potentials are shifted more negative in the sulfide as compared to the ion,[17] for instance comparing Ag^+ and Ag_2S:[15]

- $Ag^+ + e^- \rightleftharpoons \mathrm{Ag(s)}$: 0.799V
- $Ag_2S(s) + 2e^- \rightleftharpoons \mathrm{2Ag(s)} + S^{2-}$: -0.691V

Thus, all potentials in the original list should be considered shifted in the negative direction in the Cu-M-S sulfides and while some sulfides reduction potentials are more negative than the applied potential to reduce and thus stay as sulfides, others like Cu-Sb-S, Cu-Bi-S and Cu-Ag-S, are less negative than the applied potentials, allowing them to be reduced. If -0.69V vs SHE is converted to RHE at pH of about 8.2, it is -0.2V, which is less negative than the experimentally applied voltage of -1V. This implies that Ag_2S would also be reduced under the conditions applied.

4.3 Investigation on the role of chalcogen on Cu-Sb-X

4.3.1 Powder characterization

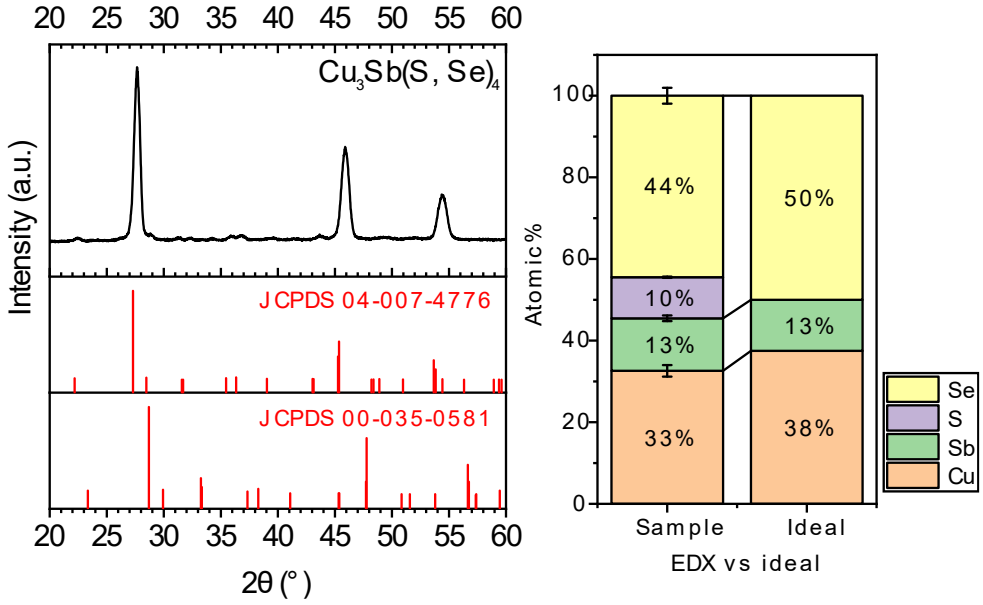

Figure 4.6: (a) XRD and (b) EDX of powder samples of $Cu_3Sb(S, Se)_4$

$Cu_3Sb(S,Se)_4$ was synthesized by heat-up method in a similar manner to Cu-Sb-S, with selenium dissolved in dodecanethiol and oleylamine as selenium source. XRD in Figure 4.6 showed that tetragonal $Cu_3Sb(S, Se)_4$ was formed, while EDX showed a slight doping of S with Se:S ratio of 4.4:1.

4.3.2 CO_2RR reduction behaviour

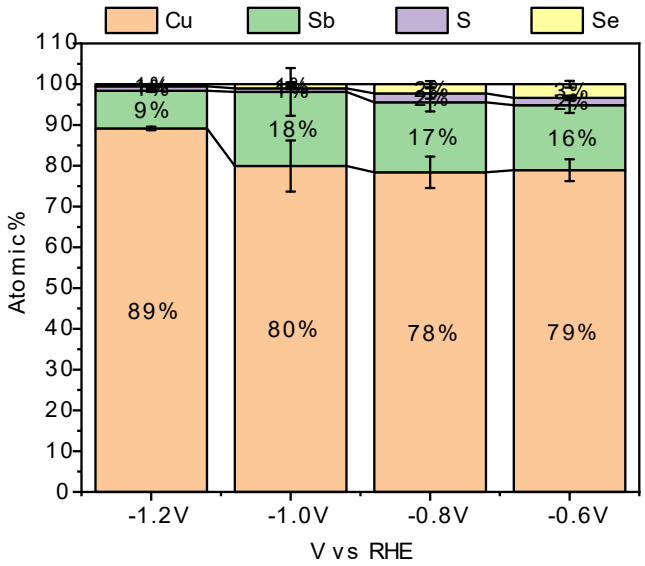

Figure 4.7: EDX of Cu-Sb-S/Se on carbon paper after electrochemical CO_2 reduction at different voltages

EDX was taken after CO_2 reduction for 45 minutes, and it was found that just like Cu-Sb-S, Cu-Sb-S/Se also reduced. However, as can be seen in Figure 4.7, the amount of S and Se remaining was very similar even though the initial amount of selenium was much higher than the sulfur. It was found that as voltage increases, less sulfur and selenium remained which is expected as these are more prone to reduction as voltage becomes more negative. However, surprisingly at -1.2V, the amount of Cu increases and amount of Sb decreases. This has important consequences for selectivity as can be seen in the CO_2RR performance below.

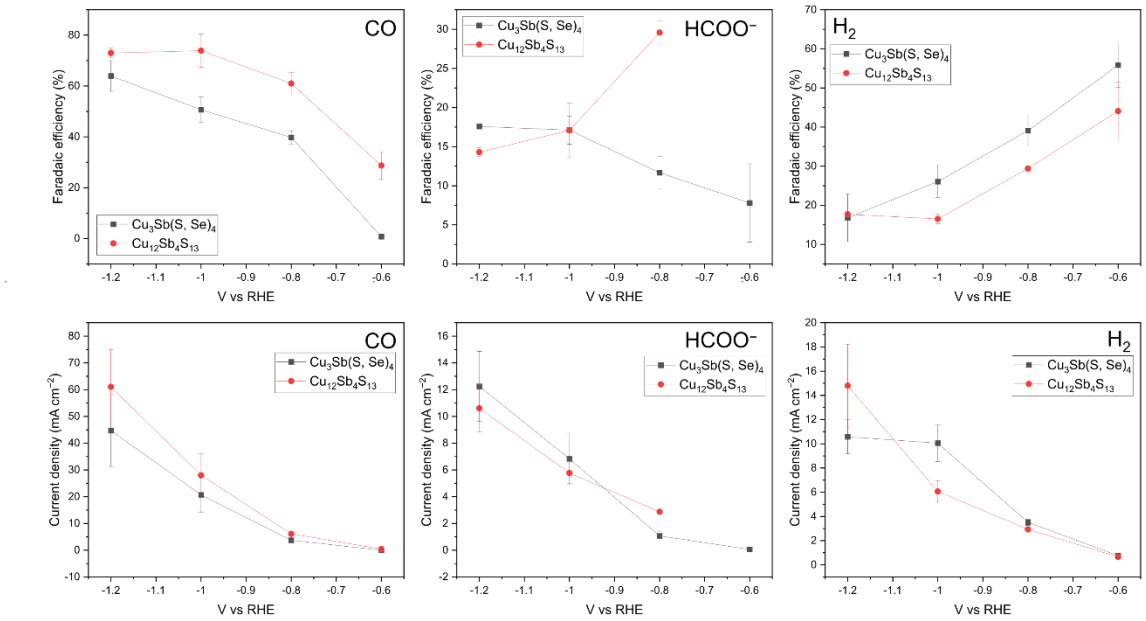

Figure 4.8: Electrochemical CO_2 reduction results of Cu-Sb-S/Se and Cu-Sb-S

When the samples were reduced between -0.6V and -1.2V vs RHE, it was found that on average the CO FE of the sulfoselenide is lower than the sulfide, while that of H_2 is higher (Figure 4.8). However, at -1.2V vs RHE, the current density of H_2 drops, which resulted in a decrease in FE of H_2 and an increase in FE for $HCOO^-$ and CO. This can be correlated to the decrease in Sb, indicating that Sb plays a role in the formation of H_2. This matches well with the DFT findings (in Appendix B) which found that both the C-binding site for CO and O-binding site for $HCOO^-$ is on Cu. It is also likely that S or Se plays a role in the binding of *H likely together with Sb.

4.3.3 Comparison with literature

It is instructive to compare our results with the results on the Cu-S/Se and Cd-S/Se systems which were carried out by López's group and Zeng's group respectively.[10, 11]

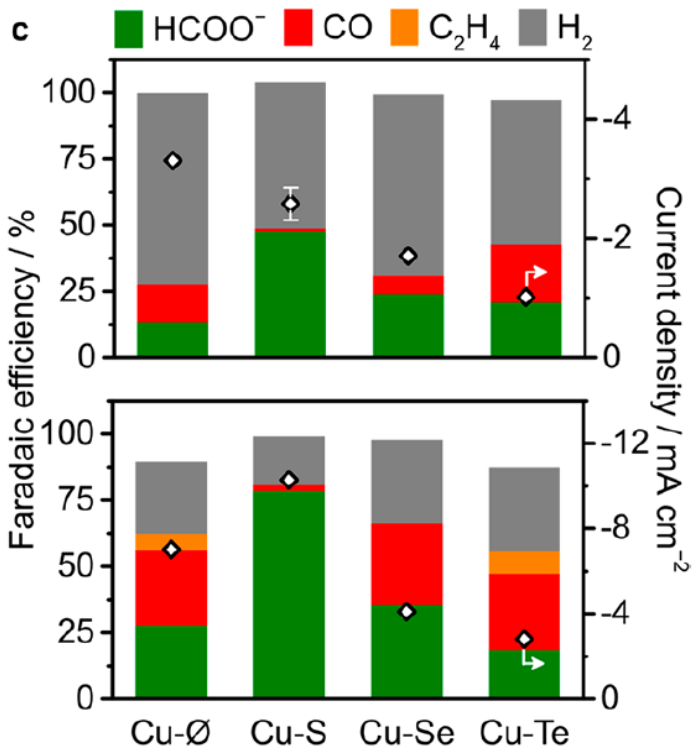

Figure 4.9: Electrochemical CO_2 reduction results of CuSx, CuSex and CuTex catalysts reported by [10]. *No permission is required for thesis purposes.*

On the CuSSe system, López's group found that the system reduces with only a few atomic percent of sulfur or selenium, which is very similar to our Cu-Sb-S/Se system. As sulfur is replaced with selenium in the Cu-S/Se, the $HCOO^-$ FE decreases and the H_2 and CO FE increases. However, the study in this chapter obtained a different trend, with a decrease in CO FE, an increase in H_2 FE, and potential-dependent variation in the $HCOO^-$ FE (decreasing at smaller applied voltage but increasing at larger applied voltage) when selenium was introduced into the system.

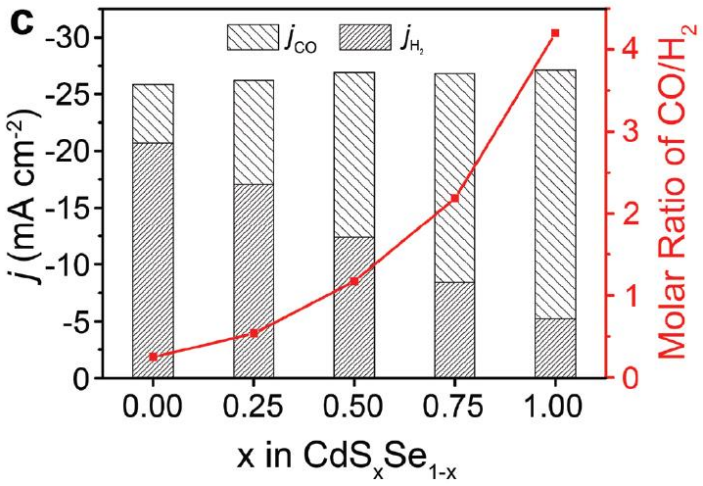

Figure 4.10: Electrochemical CO_2 reduction results of CdSxSe1-x. Reproduced with permission from [11]

Indeed, the results of Cu-Sb-S/Se, despite containing Cu, is more similar to the results obtained on the Cd-S/Se system by Zeng's group. While Zeng's group did not investigate whether the cadmium chalcogenides reduced after electrochemical CO_2 reduction, they obtained a decrease in CO FE and an increase in H_2 FE with decreasing amounts of sulfur and increasing amounts of selenium. Li's group in their study of CdS used XPS to show that the CdS in their system was not reduced after electrochemical CO_2 reduction. This indicates that CdS is stable within the range of -0.7 to -1.1 V vs RHE, which corroborates with the standard reduction potential of Cd^{2+}:

- $Cd^{2+} + 2e^- \rightleftharpoons \mathrm{Cd(s)}$: -0.4V

This is unlike the Cu-Sb-S/Se system which easily reduces, hence making the system more similar to Cu-S/Se with respect to reduction behaviour.

Thus, the Cu-Sb-S/Se system shares its reduction behaviour with Cu-S/Se, but its electrochemical CO_2 reduction behaviour is more similar with that of Cd-S/Se. Whether this has any implications on the differences in role of bulk sulfide/selenide on one hand and doped sulfur/selenium on the other warrants further experimental and computational investigation.

4.4 Conclusion

In summary, Cu-M-S samples with different M (In, Sn, Sb, Bi, Ga, Ge, Ag, Co, Fe) were synthesized and the production of correct sulfide phases via XRD were verified. These

were then tested as catalysts for electrochemical CO_2 reduction. It was found that only main group elements of period 5 and below (In, Sn, Sb, Bi) are active for electrochemical CO_2 reduction, with the rest (Ga, Ge, Ag, Co, Fe) producing hydrogen as the overwhelmingly dominant product. EDX measurements after reduction showed that when elements in Groups 11 and 15 (Ag, Sb, Bi) were used as the second M, the sulfides were reduced when voltage was applied while elements in other groups showed partial or no reduction of the sulfide. As Cu-Sb-S is the only catalyst to produce CO as the main CO_2RR product, Sb was chosen as the second element for the second part of trial tests to see if sulfoselenide Cu-Sb-S/Se outperforms sulfide Cu-Sb-S. It was found that Cu-Sb-S/Se produces more hydrogen than Cu-Sb-S, which we attribute to Se interacting with Sb to promote *H binding. Considering the results, Cu-Sb-S was for further investigation, which is reported in Chapter 5 of this thesis. The Cu-Sb-S system comprises four phases, skinnerite Cu_3SbS_3, tetrahedrite $Cu_{12}Sb_4S_{13}$, chalcostibite $CuSbS_2$ and famatinite Cu_3SbS_4. The first three phases are included in further study in chapter 5, with in-depth characterization of XRD, SEM, EDX, XPS before and after reduction as well as Tafel, CV and other analyses.

References

[1] S. Rasul, D. H. Anjum, A. Jedidi, Y. Minenkov, L. Cavallo, and K. Takanabe, "A Highly Selective Copper–Indium Bimetallic Electrocatalyst for the Electrochemical Reduction of Aqueous CO2 to CO," *Angewandte Chemie International Edition,* vol. 54, no. 7, pp. 2146-2150, 2015, doi: https://doi.org/10.1002/anie.201410233.

[2] S. Sarfraz, A. T. Garcia-Esparza, A. Jedidi, L. Cavallo, and K. Takanabe, "Cu–Sn Bimetallic Catalyst for Selective Aqueous Electroreduction of CO2 to CO," *ACS Catalysis,* vol. 6, no. 5, pp. 2842-2851, 2016/05/06 2016, doi: 10.1021/acscatal.6b00269.

[3] T. Shinagawa, G. O. Larrazábal, A. J. Martín, F. Krumeich, and J. Pérez-Ramírez, "Sulfur-Modified Copper Catalysts for the Electrochemical Reduction of Carbon Dioxide to Formate," *ACS Catalysis,* vol. 8, no. 2, pp. 837-844, 2018/02/02 2018, doi: 10.1021/acscatal.7b03161.

[4] H.-K. Lim, H. Shin, W. A. Goddard, Y. J. Hwang, B. K. Min, and H. Kim, "Embedding Covalency into Metal Catalysts for Efficient Electrochemical Conversion of CO2," *Journal of the American Chemical Society,* vol. 136, no. 32, pp. 11355-11361, 2014/08/13 2014, doi: 10.1021/ja503782w.

[5] Y. Lai, R. J. R. Jones, Y. Wang, L. Zhou, M. H. Richter, and J. Gregoire, "The sensitivity of Cu for electrochemical carbon dioxide reduction to hydrocarbons as revealed by high throughput experiments," *Journal of Materials Chemistry A,* 10.1039/C9TA10111J vol. 7, no. 47, pp. 26785-26790, 2019, doi: 10.1039/C9TA10111J.

[6] V. Okatenko *et al.*, "Alloying as a Strategy to Boost the Stability of Copper Nanocatalysts during the Electrochemical CO2 Reduction Reaction," *Journal of the American Chemical Society,* vol. 145, no. 9, pp. 5370-5383, 2023/03/08 2023, doi: 10.1021/jacs.2c13437.

[7] T. T. H. Hoang *et al.*, "Nanoporous Copper–Silver Alloys by Additive-Controlled Electrodeposition for the Selective Electroreduction of CO2 to Ethylene and Ethanol," *Journal of the American Chemical Society,* vol. 140, no. 17, pp. 5791-5797, 2018/05/02 2018, doi: 10.1021/jacs.8b01868.

[8] B. Kim *et al.*, "Trace-Level Cobalt Dopants Enhance CO2 Electroreduction and Ethylene Formation on Copper," *ACS Energy Letters,* vol. 8, no. 8, pp. 3356-3364, 2023/08/11 2023, doi: 10.1021/acsenergylett.3c00418.

[9] L. Jia *et al.*, "Copper-Bismuth Bimetallic Microspheres for Selective Electrocatalytic Reduction of CO2 to Formate," *Chinese Journal of Chemistry,* vol. 37, no. 5, pp. 497-500, 2019, doi: https://doi.org/10.1002/cjoc.201900010.

[10] R. García-Muelas, F. Dattila, T. Shinagawa, A. J. Martín, J. Pérez-Ramírez, and N. López, "Origin of the Selective Electroreduction of Carbon Dioxide to Formate by Chalcogen Modified Copper," *The Journal of Physical Chemistry Letters,* vol. 9, no. 24, pp. 7153-7159, 2018/12/20 2018, doi: 10.1021/acs.jpclett.8b03212.

[11] R. He *et al.*, "Achieving the Widest Range of Syngas Proportions at High Current Density over Cadmium Sulfoselenide Nanorods in CO2 Electroreduction," *Advanced Materials,* vol. 30, no. 7, p. 1705872, 2018, doi: https://doi.org/10.1002/adma.201705872.

[12] Y. Huang, Y. Deng, A. D. Handoko, G. K. L. Goh, and B. S. Yeo, "Rational Design of Sulfur-Doped Copper Catalysts for the Selective Electroreduction of Carbon Dioxide to Formate," *ChemSusChem,* vol. 11, no. 1, pp. 320-326, 2018, doi: https://doi.org/10.1002/cssc.201701314.

[13] W. Luc *et al.*, "SO2-Induced Selectivity Change in CO2 Electroreduction," *Journal of the American Chemical Society,* vol. 141, no. 25, pp. 9902-9909, 2019/06/26 2019, doi: 10.1021/jacs.9b03215.

[14] Y. H. Li *et al.*, "Simple Cadmium Sulfide Compound with Stable 95 % Selectivity for Carbon Dioxide Electroreduction in Aqueous Medium," *ChemSusChem,* vol. 11, no. 9, pp. 1421-1425, 2018, doi: https://doi.org/10.1002/cssc.201800372.

[15] P. Vanysek, "Electrochemical series," *CRC handbook of chemistry and physics,* vol. 8, pp. 8-33, 2000.

[16] R. A. Pattrick, V. S. Coker, C. I. Pearce, N. D. Telling, and G. van der Laan, "The oxidation state of copper and cobalt in carrollite, CuCo2S4," *The Canadian Mineralogist,* vol. 46, no. 5, pp. 1317-1322, 2008.

[17] S. Licht, "Aqueous Solubilities, Solubility Products and Standard Oxidation‐Reduction Potentials of the Metal Sulfides," *Journal of The Electrochemical Society,* vol. 135, no. 12, p. 2971, 1988/12/01 1988, doi: 10.1149/1.2095471.

Chapter 5* Covalency-aided electrochemical CO_2 reduction to CO on sulfide-derived Cu–Sb

*p-block dopants like sulfur have been shown to break scaling relations in electrocatalytic CO_2 reduction reaction (CO_2RR) by providing alternative binding sites with altered *CO binding energy. However, most sulfur derived catalysts reported to date tend to produce formate or hydrogen during CO_2RR by shifting the reaction pathway away from C-bound intermediates. In this chapter, highly selective CO production on bimetallic Cu-Sb-S derived catalyst was discovered. The high CO selectivity is in contrast with the individual control samples of CuSx and SbSx that demonstrate preference towards formate product. Interestingly, different starting phase and atomic ratio of Cu-Sb-S affects the CO_2RR selectivity. Post-catalysis characterization coupled with DFT calculations indicate that the key enabler towards CO formation is the substitution of Sb sites with sulfur that improves *COOH binding relative to *CO, breaking scaling relations and facilitating subsequent CO(g) formation. The highest CO production of FECO = 80.5% was observed on tetrahedrite Cu-Sb-S-derived sample at -1.0 V RHE with 37.6 mA/cm2 geometric partial current density.*

*This section published substantially as ***J. Mater. Chem. A***, 2024,**12**, 1840-1851, DOI: 10.1039/D3TA04777F (No written permission is required from Royal Society of Chemistry for thesis purpose.)

5.1 Introduction

Most sulfide-derived catalysts so far have tended to produce $HCOO^-$ as their main electrochemical CO_2 reduction product. This can most prominently be seen in CuS-derived catalysts, where the selectivity switches from CO and reduced products to $HCOO^-$.[1-5] This is attributed to the weakening of *CO binding by remnant surface sulfur which then favours the other products that do not rely on C-bound intermediates, namely $HCOO^-$ and H_2.[6-8]

However, as Kim et al has reported in a computational study on AgS-derived catalyst, sulfur also strengthens *COOH binding on weaker *CO-binding elements, which can result in increased CO selectivity.[9] This requires also that the amount of sulfur doping be minute enough that *H coverage does not increase substantially to favour H_2 or $HCOO^-$.[3, 7, 10]

As an alternative to sulfide-doped monometallics, bimetallics with strong and weak *CO-binding metals were considered. Cu-In, Cu-Sn and Cu-Sb were considered as there are many stoichiometric ternary starting phases that can be exploited to control the sulfur doping amount and doping content can be reduced as sulfur may only be stable on certain sites.[11-13] Thus Cu-In-S, Cu-Sn-S and Cu-Sb-S were chosen and preliminarily tried for electrochemical CO_2 reduction. As only Cu-Sb-S was reduced from its parent sulfide (Figure B.1), it was selected as the subject of this study as an S-doped bimetallic. Cu–Sb–S is also a suitable system as there are multiple stoichiometric phases that can be exploited to modulate the elemental ratio of the catalyst. Three Cu–Sb–S phases, skinnerite (SK; Cu_3SbS_3), tetrahedrite (TH; $Cu_{12}Sb_4S_{13}$), and chalcostibite (CS; $CuSbS_2$) were included in this study.

In this chapter, highly selective CO production on bimetallic Cu-Sb-S derived catalyst was discovered. The high CO selectivity is in contrast with the individual control samples of CuS_x and SbS_x that demonstrate preference towards $HCOO^-$. Different starting phase and atomic ratio of Cu-Sb-S affects the CO_2RR selectivity. Post-catalysis characterization

coupled with DFT calculations indicate that the key enabler towards CO formation is the substitution of Sb sites with sulfur that improves *COOH binding relative to *CO, breaking scaling relations and facilitating subsequent CO(g) formation. The highest CO production of FE_{CO} = 80.5% was observed on tetrahedrite Cu-Sb-S-derived sample at -1.0 V RHE with 37.6 mA/cm^2 geometric partial current density.

5.2 Results and discussion

5.2.1 Characterization of Cu-Sb-S phases

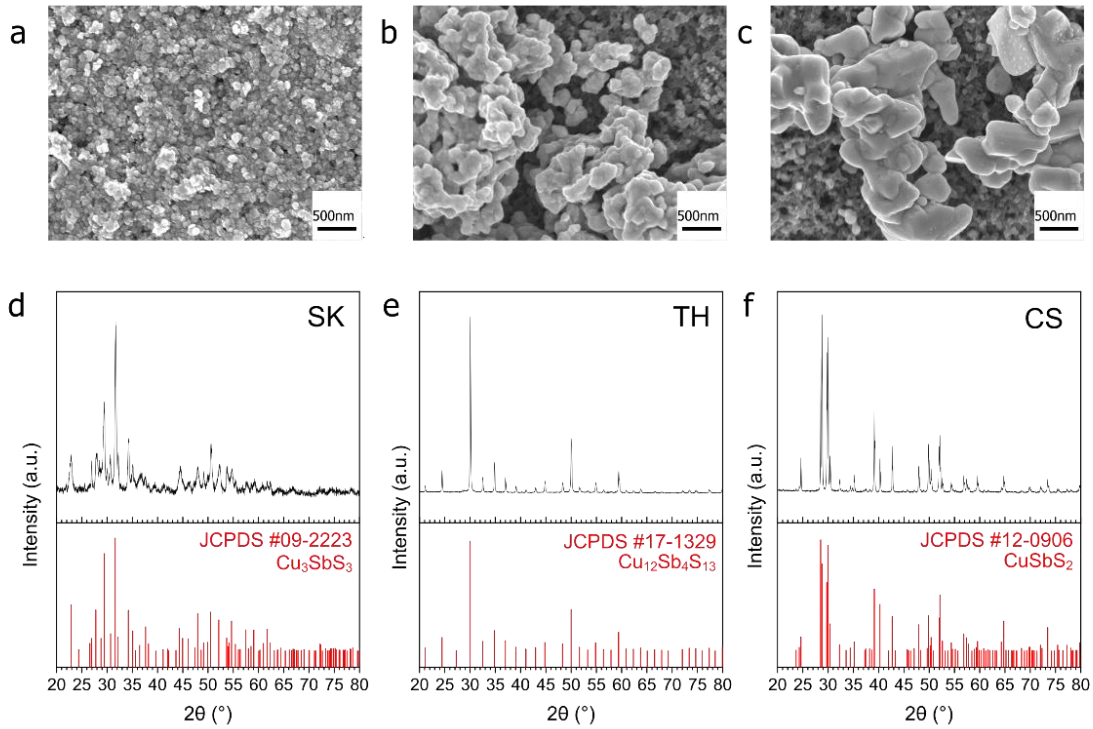

Figure 5.1: XRD and SEM characterization of the samples before reduction. (a–c) SEM images of the samples SK (a), TH (b) and CS (c) sprayed on carbon paper. (d–f) XRD images of powder samples SK (d), TH (e) and CS (f).

XRD characterization confirms the identity of the respective phases (Figure 5.1D-F). Field emission scanning electron microscopy (FE-SEM) showed distinct morphologies with particle size in the order of SK<TH<CS (Figure 5.1A-C and Figure B.2). In terms of length, SK showed nanoplates on the order of tens of nm, TH showed agglomerated particles about 100nm, while CS has the largest particle size at about 500nm to 1µm.

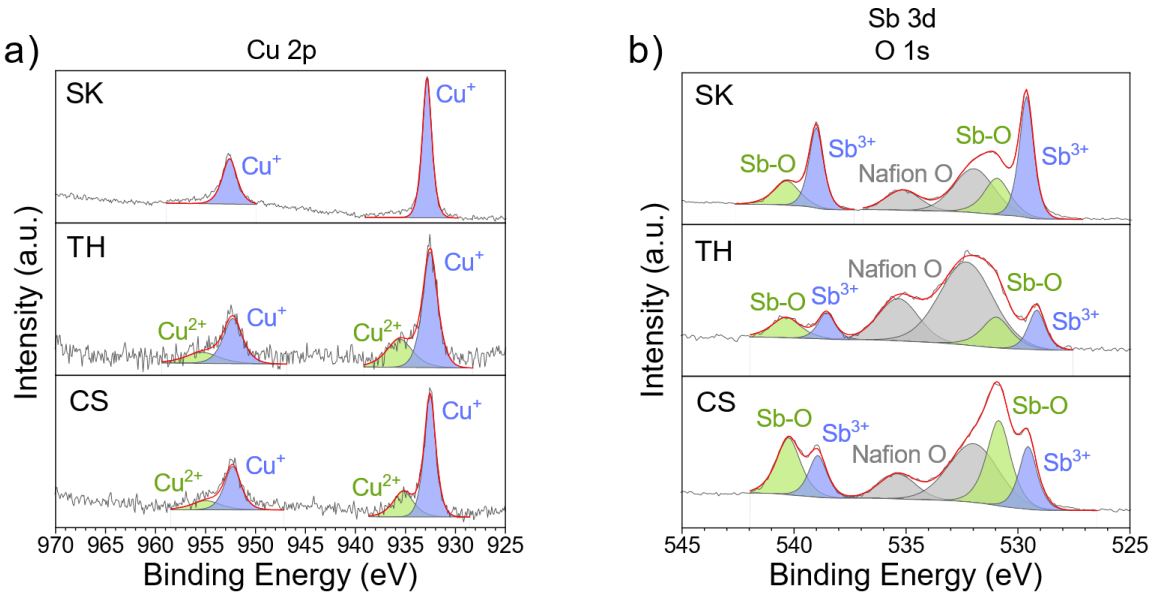

Figure 5.2: XPS peaks of the three catalyst samples on carbon paper before reduction. a) Cu 2p peaks b) Sb 3d and O 1s peaks.

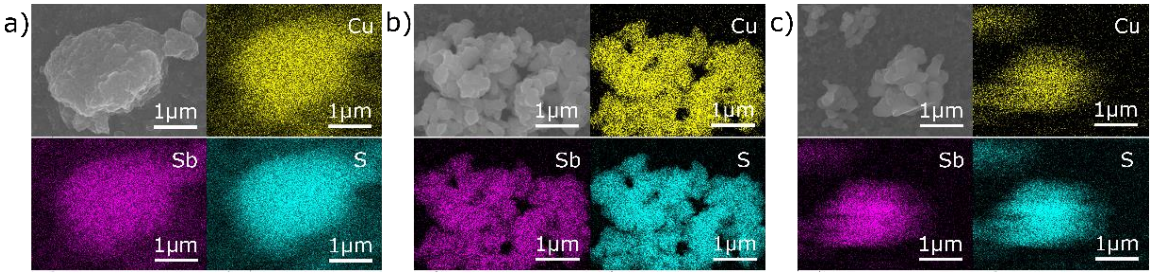

Figure 5.3: EDX mapping of the three catalyst samples on carbon paper before reduction. a) SK b) TH c) CS.

The elemental composition of the samples using energy-dispersive X-ray spectroscopy (EDX) and X-ray photoelectron spectroscopy (XPS) (Figures 5.2, 5.3, and 5.4) were then analysed. The elemental composition of the samples before reduction is close to the stoichiometric ratios, thus confirming the successful synthesis of Cu-Sb-S catalysts. XPS analysis showed two distinct species of Cu, Sb, and S each which originate in the catalyst. The two Cu species were attributed to major Cu^{+} and minor Cu^{2+} (due to surface oxidation), the two Sb species to major Sb^{3+} and minor Sb-O (due to surface oxidation), and the two S species to S^{2-} and adsorbed dodecanethiol (the sulfur source used for synthesis).[14, 15]

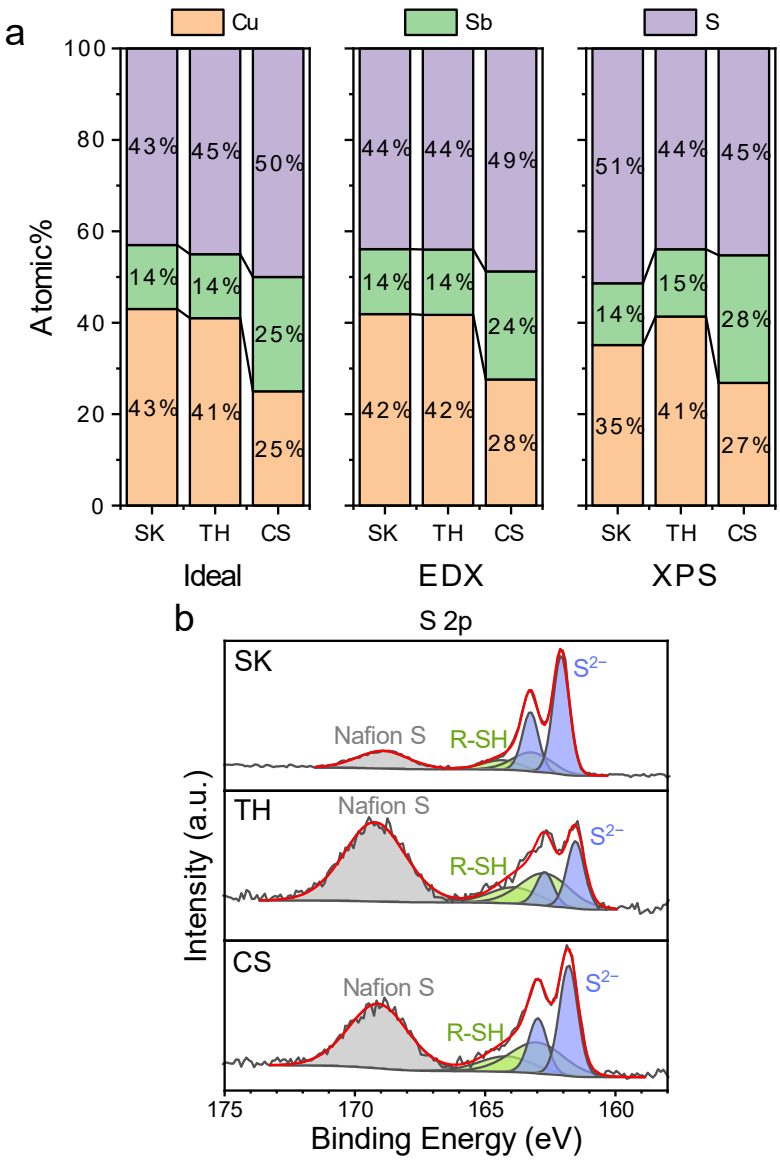

Figure 5.4: EDX and XPS characterization of the samples before reduction. (a) elemental composition of samples on carbon paper. (b) XPS S 2p peaks of the samples on carbon paper.

5.2.2 Electrochemical performance of Cu-Sb-S phases

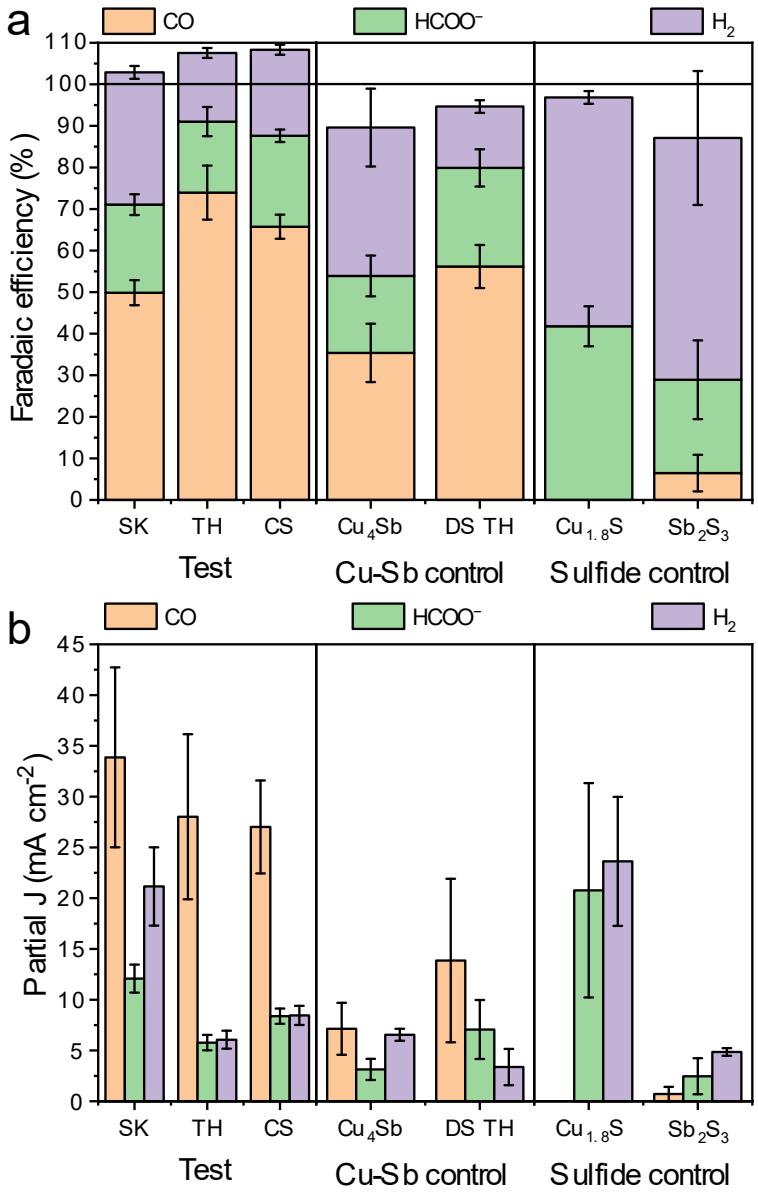

Figure 5.5: Electrochemical CO_2RR performance of the test vs. control (Cu–Sb or sulfide) samples at −1.0 V vs. RHE. Data for (a) faradaic efficiency and (b) current density. The electrolyte used was 1 M $KHCO_3$. For the test samples, data were collected from three individual experiments each, and the error bars represent the standard deviation.

The synthesized Cu-Sb-S phases were tested as catalysts by airbrushing the catalyst ink onto a GDE and testing it in a three-compartment flow cell with 1 M $KHCO_3$ electrolyte. It was found that all Cu-Sb-S catalysts (SK, TH, CS) produced a substantial amount of CO (FE_{CO} ≈50-70%) at −1.0 V (Figure 5.5). This is in contrast with the pure metal sulfide control samples of $Cu_{1.8}S$ and Sb_2S_3 (characterisation in Figure B.3), where $HCOO^-$ is the

dominant product as also seen in Figure 5.5, in line with the literature.[1-3] While the CuSb alloy also produces a fair amount of CO (FE_{CO} ≈40%), Cu-Sb-S catalysts significantly outperforms CuSb alloy in terms of CO production, hence the S chalcogen may be responsible in boosting the catalysis activity.

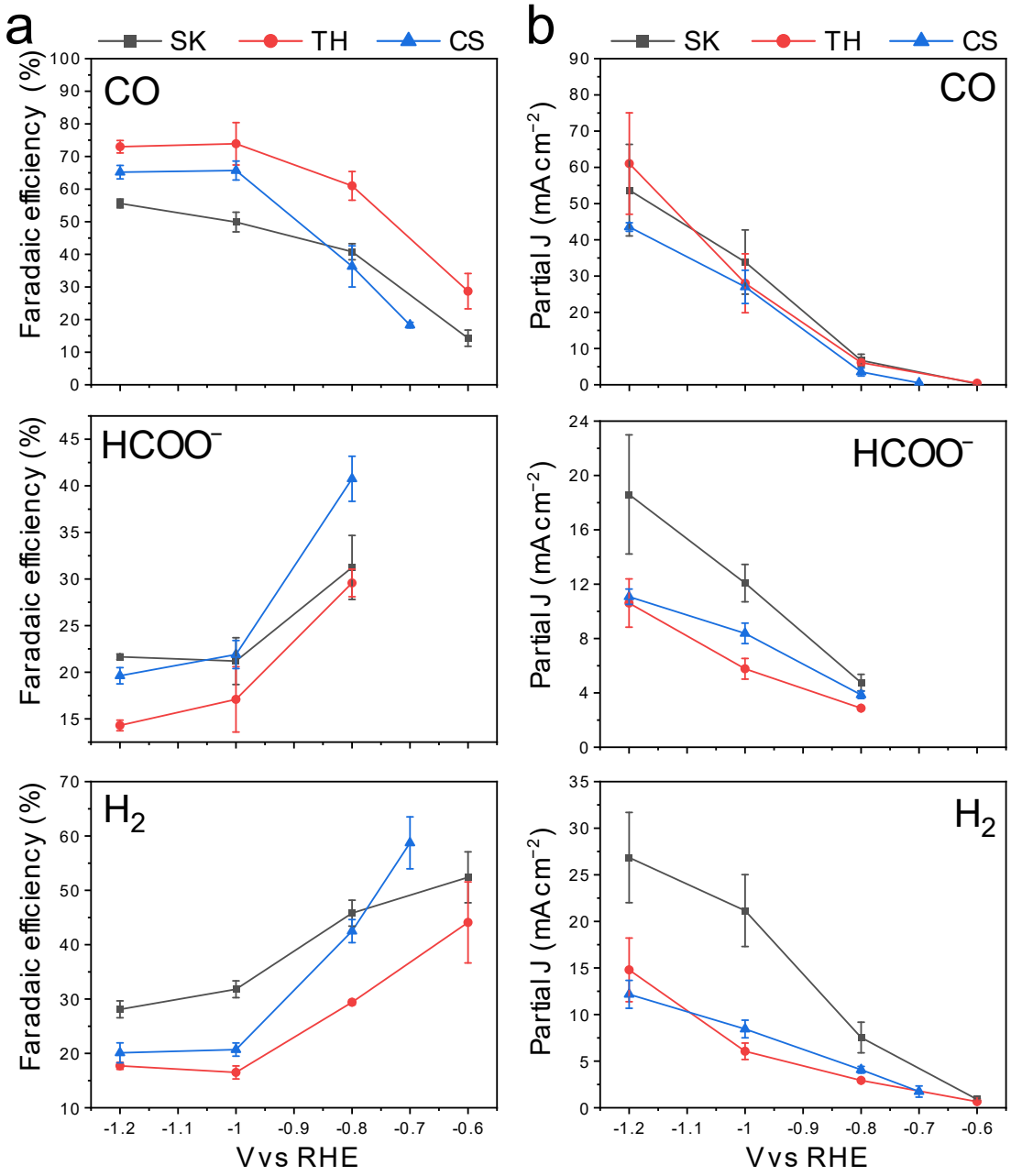

Figure 5.6: Electrochemical CO_2RR performance of catalysts. Data for (a) faradaic efficiency and (b) current density. The electrolyte used was 1 M $KHCO_3$. Data were collected from three individual experiments each, and the error bars represent the standard deviation. The data are displayed for CO, $HCOO^-$ and H_2.

The Cu-Sb-S catalysts were then tested for CO_2 reduction in a wider potential range, from the onset potential to −1.2 V. The full electrochemical CO_2RR results are shown in Figure 5.6. It was found that FE_{CO} increases with more cathodic potentials and reach maximums of between 60 to 80% at a potential of −1.0 to −1.2 V. These high efficiencies contrast with FE_{H2} and FE_{HCOO-}, which decreased at more cathodic potentials to <30% each at −1.0 to −1.2 V. Constant current CO_2RR measurement at 200 mA cm^{-2} was also performed where the catalysts retain >60% Faradaic efficiency (Figure B.4).

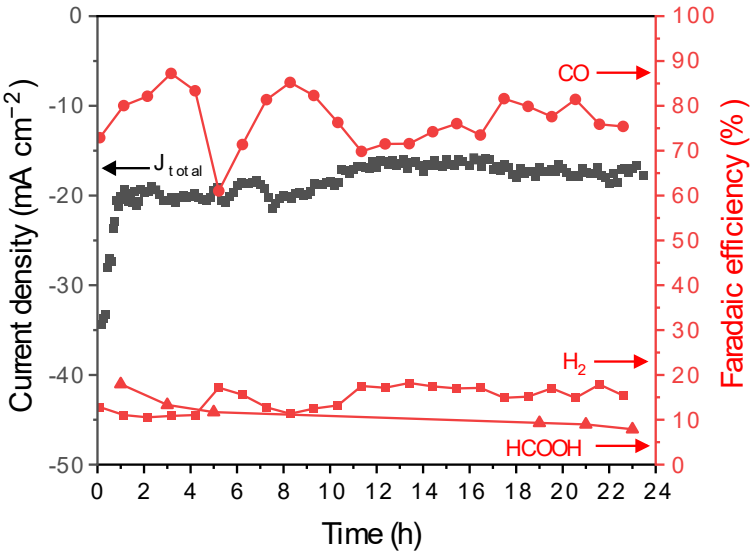

Figure 5.7: Stability test of TH sample done for 24 hours at -1V vs RHE.

The TH catalyst demonstrated good stability in the range of 24 h, with stable FE_{CO} in the 60−80% range (Figure 5.7). A maximum FE_{CO} of 80.5% at an applied voltage of −1.0 V was obtained for the TH sample, which is comparable with the literature maximums FE_{CO} of 80-95% for Cu-Sb materials (Table 5.1).

Table 5.1: Benchmarking against other similar catalysts in literature

Catalyst	Electrolyte	Potential (V vs. RHE)	CO partial current density (mA/cm^2)	CO_2RR main product	Reference
Cu-Sb catalysts					
CuO-Sb_2O_3/CB Nanocomposites (Cu:Sb of 10:1)	0.1 M $KHCO_3$	−0.8	4.5	CO	[16]
Sb-modified Cu (galvanic displaced)	0.1 M $KHCO_3$	−1.1	4.5	CO	[17]
Cu_2Sb decorated Cu nanowire arrays	0.1 M $KHCO_3$	−0.9	6	CO	[18]
Sb-doped Cu/Cu_2O catalyst	0.1 M $KHCO_3$	−0.9	6.3	CO	[19]
Cu-Sb_2O_3	0.1 M KCl	−0.99	6.7	CO	[20]
Sb-Cu_2O derived bimetallic catalyst	0.1 M $KHCO_3$	−0.8 to − 1.2	37.3 to 74.0	CO	[21]
Single atom Sb on Cu	0.5 M $KHCO_3$	−0.97	150	CO	[22]
Sulfide-derived Cu-Sb catalyst					
S-derived Cu-Sb	1 M $KHCO_3$	−1.0	37.6	CO	This work
Other sulfide-derived catalysts					
S-modified Cu	0.1 M $KHCO_3$	−0.8	Trace	$HCOO^-$	[1]
CdS nanorods	0.1 M $KHCO_3$	−1.2	27.1	CO	[23]

It is noted however, that the literature reports of Cu-Sb are not pristine (deposited on Cu nanowires)[18] or not well-mixed (galvanic-displaced or composites)[16, 17] may not be accurate sulfur-free reference standards to compare the study's samples against. It may be that if both structural control and sulfur doping are simultaneously engineered, an even better Cu-Sb-based catalyst performance can be achieved. The best-performing TH had a geometric partial current density of CO of about 37.6 mA cm^{-2} at −1.0 V in 1 M $KHCO_3$ GDE flow cell, which is approximately seven times that of literature values of ~5 mA cm^{-2} at the same voltage in 0.1 M $KHCO_3$ H-type cells (Table 5.1). This is partially due to a difference in cell type (GDE flow cell vs H-cell) and electrolyte concentration, thus the increase in current density due only to the catalyst would be smaller. Current densities of

$HCOO^-$ and H_2 at −1.0V for the TH catalyst were 5.7 mA cm^{-2} and 6.0 mA cm^{-2} respectively.

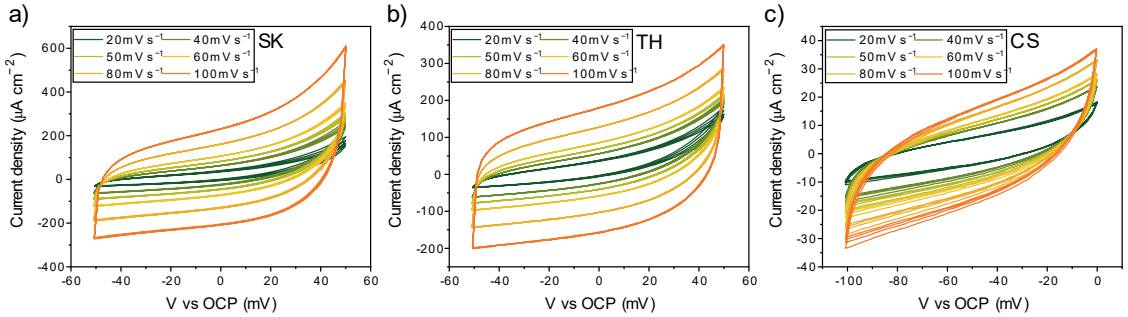

Figure 5.8: Cyclic voltammograms of the three catalyst samples done in non-Faradaic region for determination of electrochemically active surface area (ECSA). Catalysts were pre-reduced at 55mA/cm^2 prior to the test which was done on a 3mm diameter glassy carbon electrode.

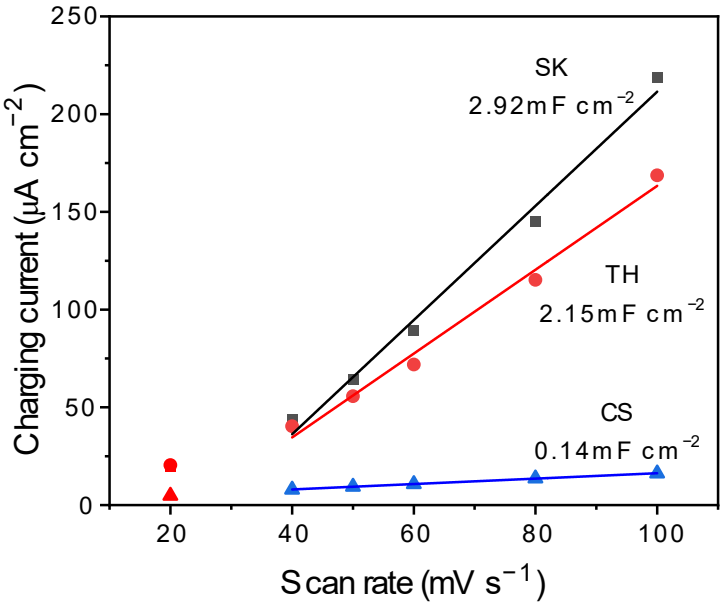

Figure 5.9: Charging current densities plotted against scan rate with double layer capacitance indicated for the three Cu-Sb-S catalysts. Catalysts were pre-reduced at 55mA/cm^2 prior to the test which was done on a 3mm diameter glassy carbon electrode.

The onset potential for CO formation is −0.6 V for the Cu:Sb 3:1 phases (SK and TH) and −0.7 V for the Cu:Sb 1:1 phase (CS). Electrochemically active surface area (ECSA) measurements were performed on the samples at -1.0 V (Figures 5.8 and 5.9), which shows that SK and TH have similar total current densities when normalized to the active surface

area. The double layer capacitance showed SK>TH>>CS, which is approximately in the reverse order compared to the particle size seen in FE-SEM.

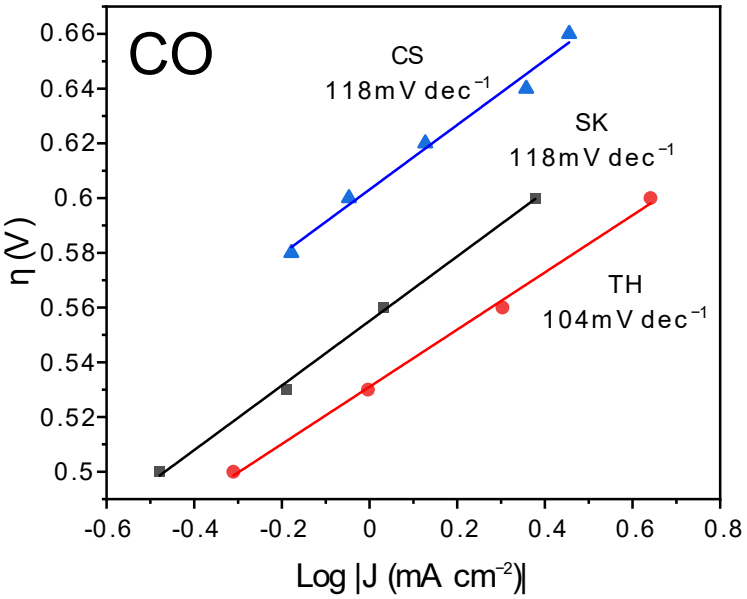

Figure 5.10: CO Tafel slopes of the catalysts. Catalysts were pre-reduced for 5 min at −1.0 V vs. RHE prior to the experiment.

To investigate the kinetics of the reaction, Tafel slopes of the current density readings were plotted in Figure 5.10. The best performing TH catalyst had a lower Tafel slope of 104 mV/dec compared to the other two catalysts which each registered 118 mV/dec. According to the literature, an ideal Tafel slope of 120 mV/dec corresponds to an electron transfer step as the rate-determining step: $* + CO_2 + e^- \rightarrow {}^*CO_2{}^-$.[24] Conversely, an ideal Tafel slope of 60 mV/dec corresponds to a protonation step as the rate-determining step: ${}^*CO_2{}^- + H^+ \rightarrow {}^*COOH$. Based on the Tafel slopes, it is possible that although the electron transfer step is the main rate-determining step, some reaction sites on the TH sample might have better kinetics with the protonation step as the rate-determining step, resulting in better CO Faradaic efficiency.

5.2.3 Post-reduction characterization and remnant sulfur

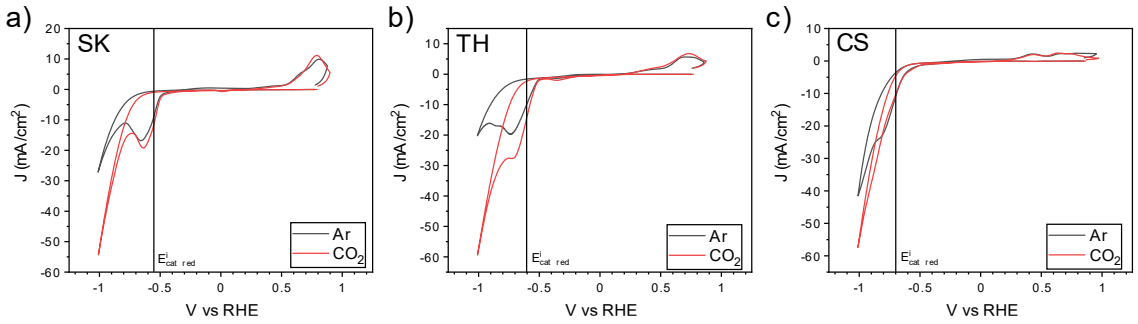

Figure 5.11: Cyclic voltammograms of the three catalyst samples done in Ar and CO_2, with the catalyst reduction potential, which was obtained from the inflection point of the derivative, indicated.

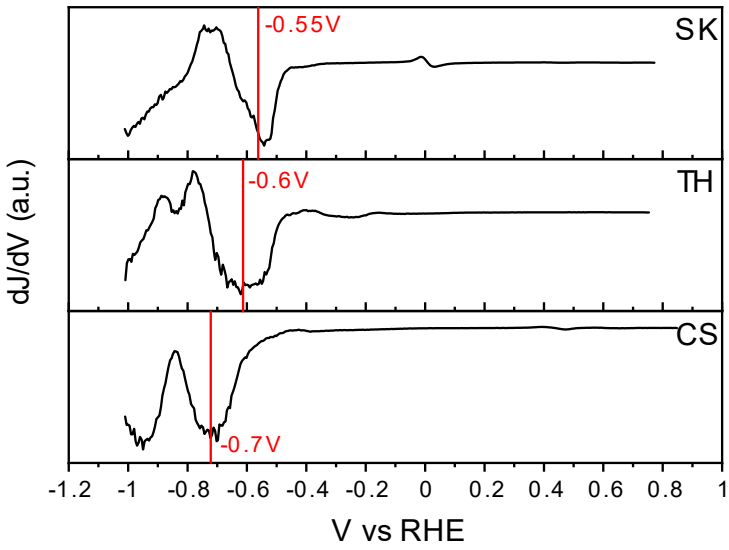

Figure 5.12: Derivative of cyclic voltammograms of the three catalyst samples with the value of the catalyst reduction potential indicated.

CV scans were performed on the three Cu-Sb-S phases to determine the reduction potential of these samples (Figure 5.11). From the inflection point of the cathodic going CV first derivative,[25, 26] the reduction potentials of the samples (−0.55, −0.60, and −0.70 V for SK, TH, and CS respectively, Figure 5.12) were determined to be the same or more positive than the CO_2RR to CO onset (between -0.6 to -0.7 V, Figure 5.6), indicating that CO_2RR to CO occurs after the reduction process of the sulfide phases.

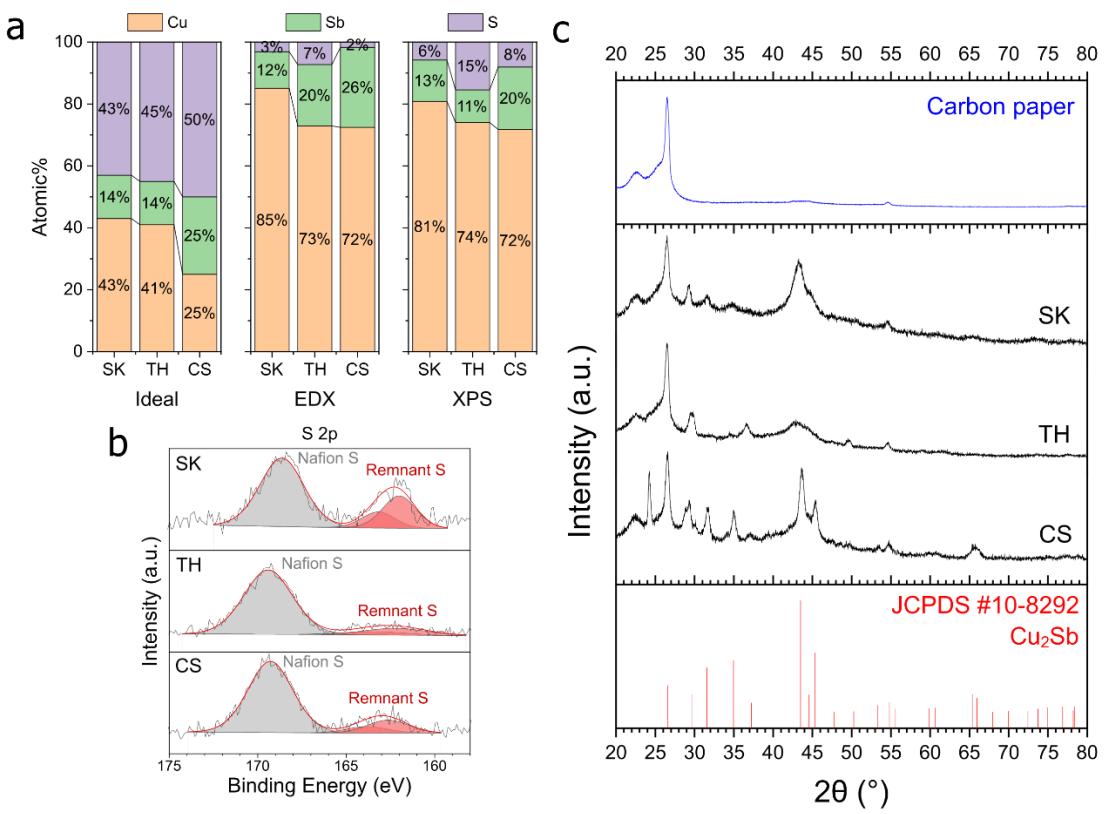

Figure 5.13: EDX, XPS and XRD characterization of the samples after reduction. (a) Elemental composition of the samples on carbon paper. (b) XPS S 2p peaks of the samples on carbon paper. (c) XRD image of the samples with 9× loading on carbon paper. The reference peaks are that of Cu_2Sb.

The observation that sulfide reduction occurs before CO_2RR onset is corroborated by EDX and XPS analyses post-reduction at −1.0 V (Figure 5.13). Drastic decrease in the S at% was observed on all samples. Interestingly, only a small Sb at% decrease was detected. One reason for this could be because Sb forms a stable alloy with Cu, thus it is not as easily leached compared to S. This proposition is supported by further ICP measurements of the electrolytes collected post reduction, showing that Sb had been leached at similar rate with Cu (Table B.1), possibly due to surface reconstruction.[27]

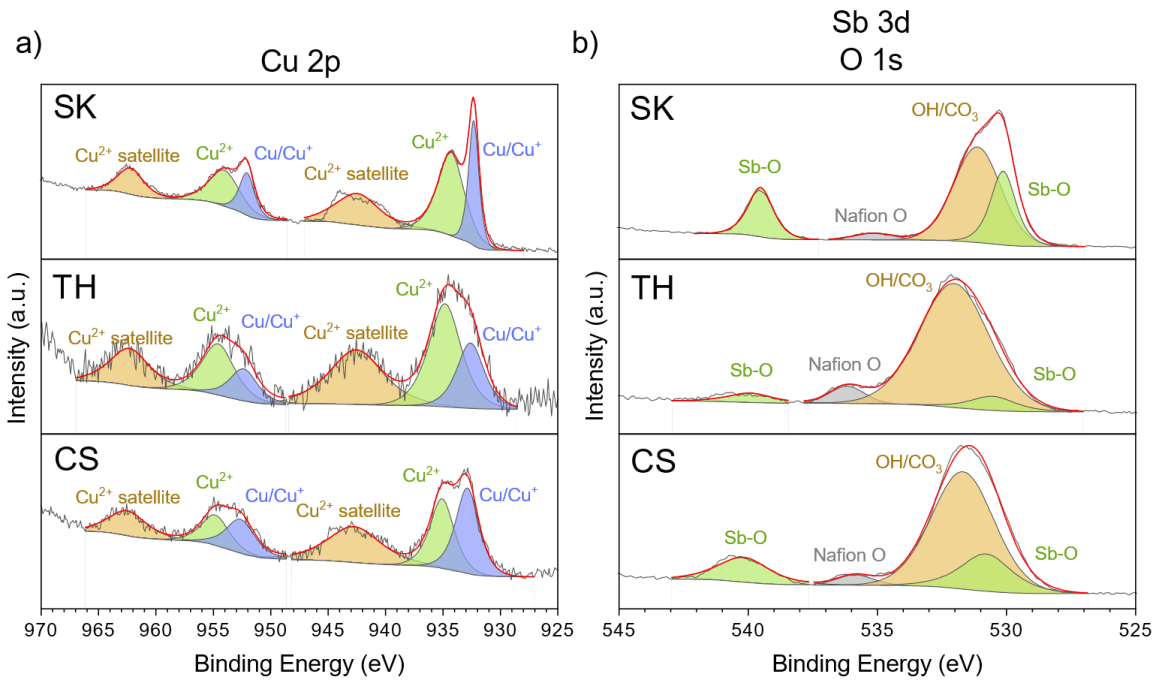

Figure 5.14: XPS peaks of the three catalyst samples on carbon paper after reduction at -1V vs RHE. a) Cu 2p peaks b) Sb 3d and O 1s peaks

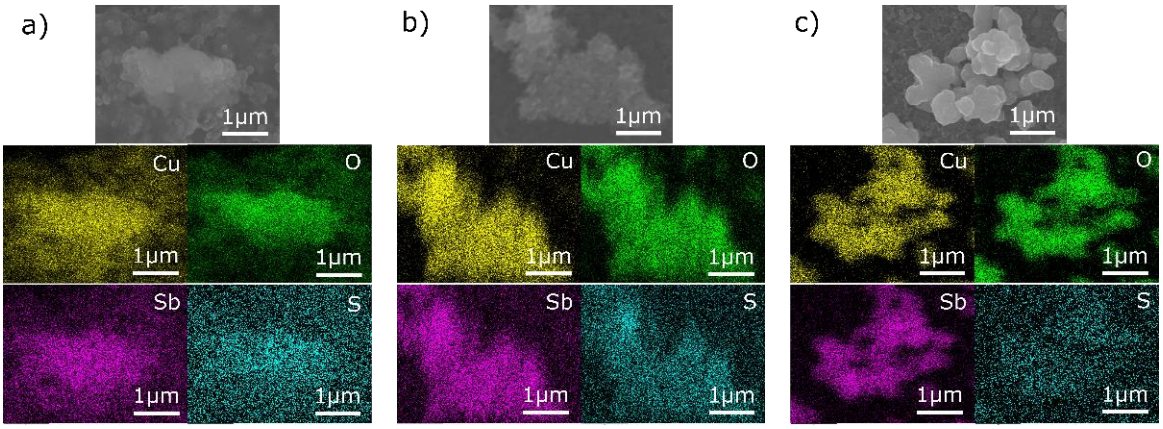

Figure 5.15: EDX mapping of the three catalyst samples on carbon paper after reduction at -1V vs RHE. a) SK b) TH c) CS

Post catalysis XPS (Figure 5.14) showed that Cu^{2+} satellite peaks appeared and the oxidized Cu^{2+} and Sb-O peaks are noticeably enlarged, while the original Sb^{3+} peaks at approx. 529.5 eV completely disappeared. The presence of oxidized Cu and Sb are likely due to surface reoxidation as the XPS measurements were done ex-situ. O presence in EDX and XPS most likely originated from catalyst re-oxidation post-electrolysis (Figures 5.14 and 5.15). O was excluded in the elemental composition analysis due to the large variation of oxygen content between samples.

As a result of the drastic decrease of sulfur content in the catalysts after electrochemical reduction, the active phase of the catalysts should thus be regarded as Cu-Sb alloys with remnant sulfur atoms as defects. XRD results (Figure 5.13c) also showed that the dominant crystalline phase present after reduction was Cu_2Sb, supporting the assignment of this phase as the active surface during electrochemical CO_2RR.

Taking the XRD data together with EDX and XPS in Figure 5.13, the S and Sb amounts appear to be correlated to the crystallinity/crystallite size of the samples. CS sample with higher Sb composition showed much smaller full-width half maximum (FWHM) peaks compared to SK and TH. TH also shows particularly broad Cu_2Sb peaks, which is proposed to be linked to much higher S content. Post-reduction selected area electron diffraction (SAED, Figure B.5) results showed very diffuse peaks that correspond to the XRD data. SEM micrographs of the catalysts after reduction showed no major changes on micrometre scale (Figure B.6), while TEM images of the catalysts after reduction (Figure B.7) showed small crystallite size on the order of a few nm that corroborates the XRD findings above.

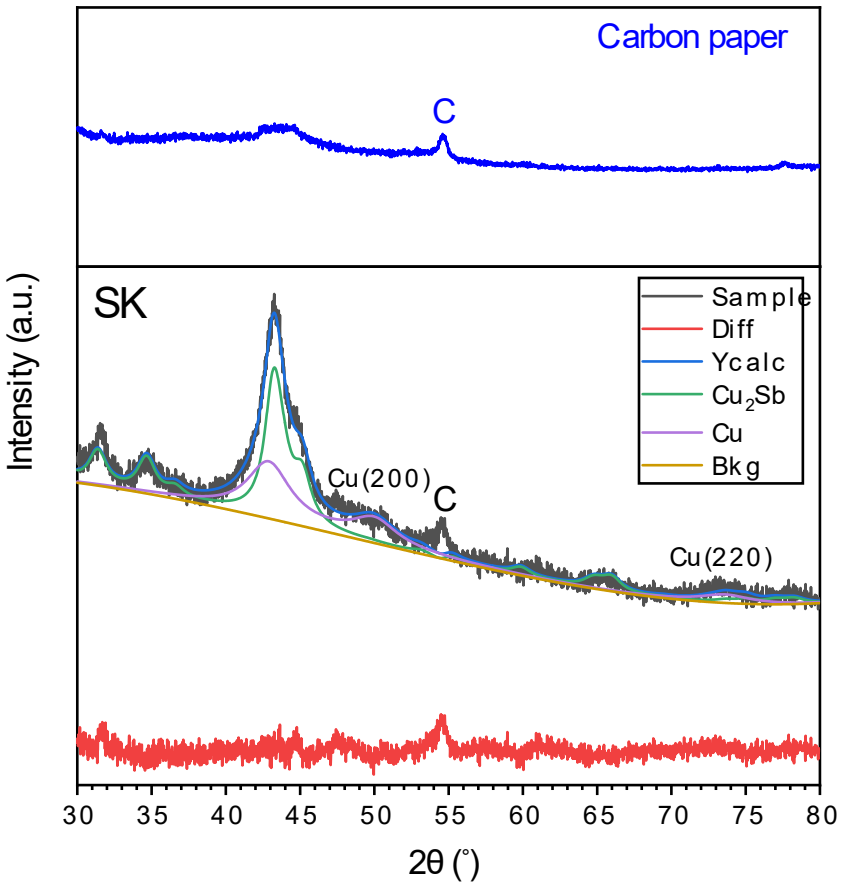

Figure 5.16: Rietveld refinement of the SK sample after reduction at -1V vs RHE for 9x loading. The peak labelled C is attributable to carbon paper. The refinement was done from 30° to 80° to exclude the carbon peak at 26.5° as well as a peak we could not identify as either Sb or Sb_2O_4.

Table 5.2: Parameters used in Rietveld refinement of SK sample after reduction at -1V vs RHE for 9x loading.

Phase	Wt%	a (Å)	c (Å)	Cry size (nm)	Rexp	Rwp	Rp	GOF
Cu_2Sb	35.951	3.9925005	6.1525887	4.750	2.50	3.42	2.61	1.37
Cu	64.049	3.6298331		1.762				

Rietveld refinement of SK detected phase segregation of Cu_2Sb and Cu (Figure 5.16 and Table 5.2). It is posited that the SK sample contains a mixture of S-doped Cu-Sb region and S-doped Cu rich region as predicted by the phase diagram (Figure 5.17). As S-doped Cu has been shown to prefer $HCOO^-$ and H_2 production in literature, [1-5] it is expected that SK phase shows lower CO. Conversely, TH and CS catalysts composition are closer to the Cu_2Sb alloy region, which imply lower S-doped Cu content. Thus, a lower Cu

amount may be advantageous to avoid Cu phase segregation and thus suppress H_2 and $HCOO^-$. This is supported by the control experiments on $Cu_{1.8}S$ that shows majority H_2 and $HCOO^-$ product (Figure 5.5a).

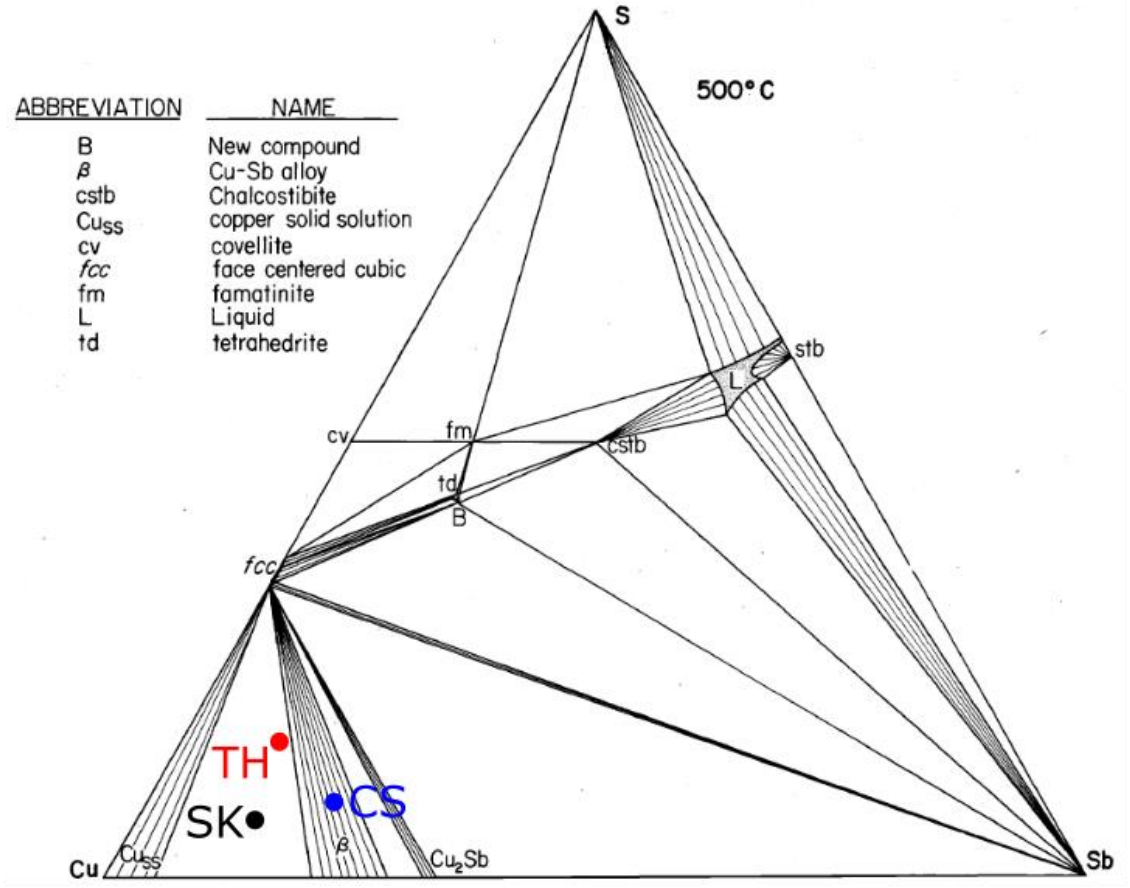

Figure 5.17: Elemental composition of samples after reduction plotted on Cu-Sb-S phase diagram taken from Skinner et al.[28] *No permission is required for thesis purposes.*

5.3 DFT calculations

Density Functional Theory (DFT) provides a theoretical framework for understanding the structure-activity relations of Cu-Sb-S. This information can help guide the design of experiments and catalysts for CO_2 reduction and improve our understanding of how these materials work. We first determine the stability of sulfur atoms in the parent phases, i.e., tetrahedrite (TH), chalcostibite (CS), and skinnerite (SK) and identify the likely contributors for improved catalytic performance.

Post-electrochemical characterisation showed significant removal of sulfur in the three parent phases. The TH phase retains the largest amount of S (7% from EDX; 15% from XPS), which is about double of that in SK (3% from EDX; 16% from XPS) and in CS (2% from EDX; 8% from XPS). The energy penalty to form a sulfur vacancy was then calculated according to equation B.1 (**Appendix Section B.2.2**) in primitive cells of bulk TH, CS and SK. This energy penalty reflects the likelihood of sulfur being retained in the structures. It was found that the energy penalty trends as TH (5.46 eV) > CS (5.33 eV) > SK (5.23 eV) with the sulfur being most strongly bound in the TH phase. This trend is consistent with the experiments wherein the TH phase retains the highest percentage of sulfur after electrochemical tests.

Characterization studies after electrochemical testing indicated that the active phase during 2e$^-$-CO_2RR is tetragonal Cu_2Sb of space group *P*4/nmm. The Cu_2Sb primitive cell lattice parameters were calculated ($a = b = 3.98$ Å$, c = 6.09$ Å$, \alpha = \beta = \gamma = 90°$) and good agreement with literature values was obtained ($a = b = 4.00$ Å$, c = 6.10$ Å$, \alpha = \beta = \gamma = 90°$).[29] Surface energies calculated for various Cu_2Sb facets presented in Table B.4 indicate that (100) surface is the lowest energy facet. To simulate the catalytic active phases of Cu-Sb-S having low sulfur content, nine active site motifs were considered (Figure B.8) based on pristine Cu_2Sb(100), with sulfur adatoms and substitutionally doped sulfur in the topmost and next atomic layer.

Due to possibilities of S-removal, three active site motifs with copper and antimony vacancies at the Cu1, Cu2 and Sb1 sites were also considered (Figure B.8a). Hence, the stability of sulfur-decorated and vacancy surface motifs were first investigated (**Appendix Section B.2.2**). It was found that the S_{Cu3}@Cu_2Sb(100) is not likely to be stable during operating conditions (Table B.2) and hence will not be considered further.

Then, the adsorption of the four key intermediates were tested: *H, *COOH, HCOO* and *CO involved in the 2e-CO_2RR (additional details in **Appendix section B.2.4**). By comparing the adsorption energies on all surfaces against those on Cu_2Sb(100) (Table B.3), seven surfaces (S_{Cu3}@Cu_2Sb(100), S_{Cu3Sb}@Cu_2Sb(100), S_{Cu1}/Cu_2Sb(100),

S_{Cu2}/Cu_2Sb(100), S_{Sb1}/Cu_2Sb(100), S_{Sb2}/Cu_2Sb(100), V_{Cu2}/Cu_2Sb(100)) bind CO* less strongly than both Cu (111) and Cu_2Sb (100). It has been demonstrated that CO_2RR catalysts that are selective towards the $2e^-$ products experimentally possess a *CO binding energy that is weaker than that on Cu(111).[30] The weaker binding of *CO on the seven surfaces will promote *CO desorption rather than further reduction to *CHO or *COH. Since the CS, SK, and TH samples showed a high selectivity towards the 2e-CO2RR products even at a more negative applied voltage of -1.2 V, these seven active site motifs are more likely to be present in the catalytic active Cu-Sb-S phases.

Table 5.3: Selectivity metrics at an operating voltage of −1.0 V. A negative (positive) value of DR1G − DR2G favours CO (formate) formation. The DR3G is used as a descriptor to define surface hydrogenation. A negative DR3G value favours surface hydrogenation

Surface Structure	$\Delta_{R1}G$ / eV	$\Delta_{R2}G$ / eV	$\Delta_{R1}G$ - $\Delta_{R2}G$ / eV	$\Delta_{R3}G$ / eV
Cu(111)	-0.42	-0.28	-0.15	-1.17
Cu_2Sb(100), reference	-0.34	0.14	-0.48	-1.05
S_{Cu3}@Cu_2Sb(100)	-0.30	0.36	-0.66	-0.92
S_{Cu3Sb}@Cu_2Sb(100)	-0.15	0.24	-0.39	-0.86
S_{Cu1}/Cu_2Sb(100)	-0.04	0.32	-0.36	-0.78
S_{Cu2}/Cu_2Sb(100)	-0.27	0.38	-0.65	-0.91
S_{Sb1}/Cu_2Sb(100)	-0.23	0.15	-0.38	-0.94
V_{Cu2}/Cu_2Sb(100)	-0.25	0.33	-0.58	-1.08
S_{Sb2}/Cu_2Sb(100)	-0.71	-0.15	-0.56	-0.99

With the remaining seven active site motifs, the selectivity analysis towards CO or HCOOH formation similar to that adopted by Tang et al was employed[31] (additional details in **Appendix Section B.2.5)**. Essentially, a motif that provides a larger driving force for *COOH formation ($\Delta_{R1}G$ in Equation B.1) than for HCOO* ($\Delta_{R2}G$ in Equation B.2) is selective towards the CO pathway. If the converse is true, the active site is more selective towards HCOOH. Another important consideration is the availability of H* for the formation of HCOO*. This availability of H* is given by Equation B.3. One can thus use $\Delta_{R1}G - \Delta_{R2}G$ as a descriptor: a negative (positive) value indicates a larger driving force for the CO (HCOOH) pathway. The values for $\Delta_{R1}G$, $\Delta_{R2}G$, $\Delta_{R1}G - \Delta_{R2}G$ and $\Delta_{R3}G$ for

the seven relevant active site motifs are in Table 5.3 while the values for all site motifs considered in this work are in Table B.6.

At the operating potential of -1.0 V, all seven Cu_2Sb-based motifs indicate that the formation of *COOH is thermodynamically favourable. It was found that $Cu_2Sb(100)$ is more selective towards CO formation as compared to Cu(111) due to a more negative $\Delta_{R1}G - \Delta_{R2}G$ value. $\Delta_{R1}G - \Delta_{R2}G$ values on the other seven motifs are negative, indicating that the CO pathway is thermodynamic favoured. In fact, $\Delta_{R1}G - \Delta_{R2}G$ values are more negative than $Cu_2Sb(100)$ on $S_{Cu3}@Cu_2Sb(100)$, $S_{Cu2}/Cu_2Sb(100)$, $V_{Cu2}/Cu_2Sb(100)$ and $S_{Sb2}/Cu_2Sb(100)$. The higher CO selectivity in Cu_2Sb-based motifs can be ascribed to a weaker H* adsorption, that leads to a more positive $\Delta_{R2}G$ value and thus a more negative $\Delta_{R1}G - \Delta_{R2}G$ value. One finds that H* adsorption is 0.12 eV weaker on $Cu_2Sb(100)$ than on Cu(111) and this H* adsorption strength can be further modulated by the presence of sulfur. In fact, it was noticed that the presence of sulfur in the six S-decorated motifs (i.e., $S_{Cu3}@Cu_2Sb(100)$, $S_{Cu3Sb}@Cu_2Sb(100)$, $S_{Cu1}/Cu_2Sb(100)$, $S_{Cu2}/Cu_2Sb(100)$, $S_{Sb1}/Cu_2Sb(100)$, and $S_{Sb2}/Cu_2Sb(100)$) further weakens *H adsorption as compared with that on $Cu_2Sb(100)$. It is noted from adsorption data in Table B.3 that $S_{Sb2}/Cu_2Sb(100)$ binds HCOO* stronger than $Cu_2Sb(100)$ while the five others motifs with sulfur as an adatom or as a substitutional dopant in the topmost layer bind HCOO* weaker. The simultaneous weakening of H* adsorption and HCOO* in turn, results in positive $\Delta_{R2}G$ values for $S_{Cu3}@Cu_2Sb(100)$, $S_{Cu3Sb}@Cu_2Sb(100)$, $S_{Cu1}/Cu_2Sb(100)$, $S_{Cu2}/Cu_2Sb(100)$ and $S_{Sb1}/Cu_2Sb(100)$. On the other hand, the enhancement of HCOO* adsorption is greater than the weakening of *H, hence giving an overall negative $\Delta_{R2}G$ value for $S_{Sb2}/Cu_2Sb(100)$. While these seven Cu_2Sb-based motifs are all selective towards CO formation, HCOOH and H_2 were also produced in the electrochemical tests. These pathways with the Gibbs energy diagrams are rationalized in the next section.

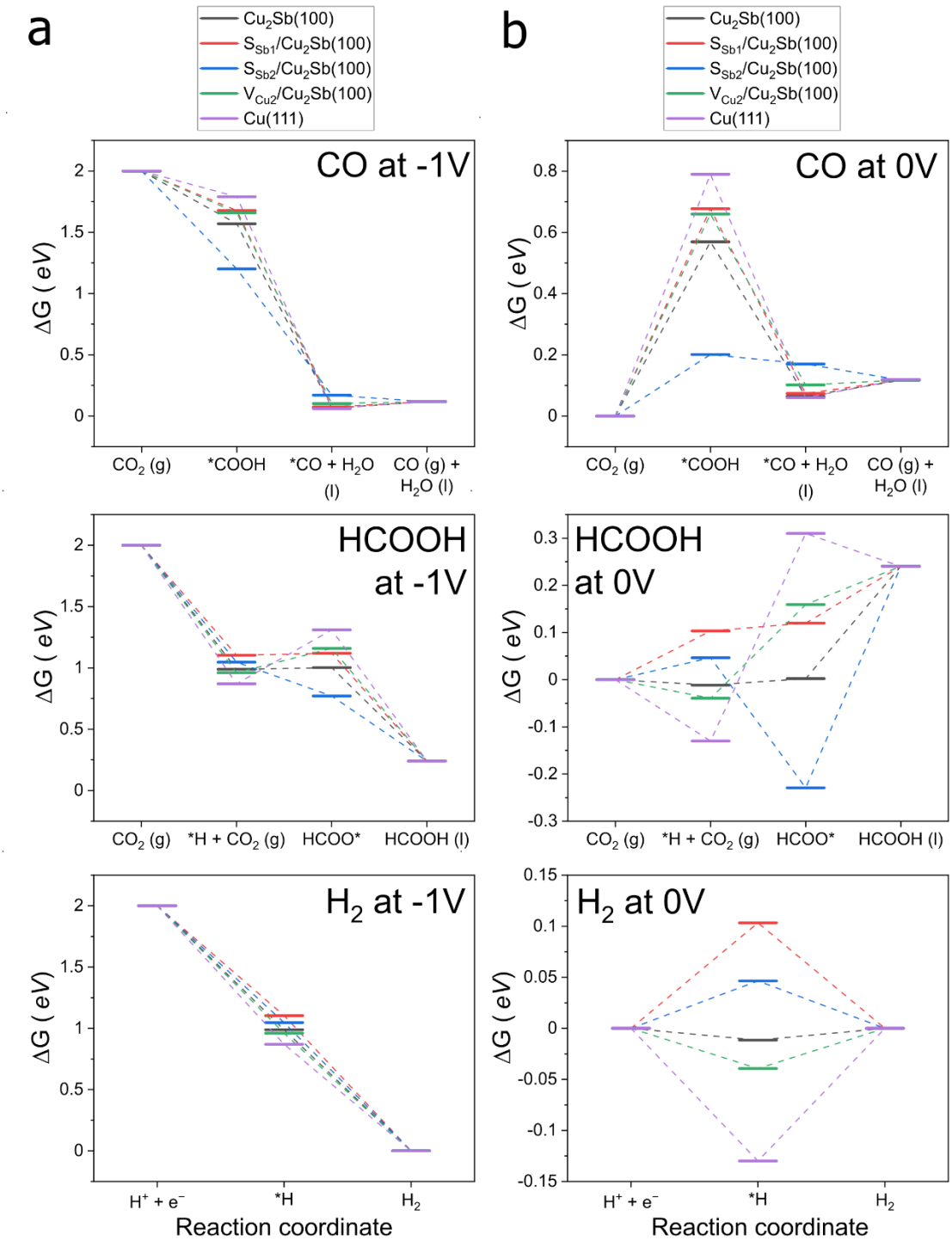

Figure 5.18: Free energy diagrams of four surface sites on $Cu_2Sb(100)$. The potentials are displayed for (a) −1.0V vs RHE to represent experimental conditions and (b) 0V vs RHE to show potential determining steps (PDS). The data are displayed for CO, HCOOH and H_2 pathways. Note that the energy level of each energy state in eV is affected by the applied potential such that they are shifted by the negative of the product of number of electrons involved (n_e) and the applied potential vs RHE (U). Hence, at an applied potential of –1.0 V vs RHE, each energy state is shifted by $+1.0n_e$ eV

From the seven sites shortlisted from the reactivity analysis, sulfur stability analysis (**Appendix Section B.2.2**) was carried out to narrow the list down further to four surface motifs that are most likely to be present throughout the electrochemical operation: pristine $Cu_2Sb(100)$, $S_{Sb1}/Cu_2Sb(100)$, $S_{Sb2}/Cu_2Sb(100)$ and $V_{Cu2}/Cu_2Sb(100)$. These four surface motifs are expected to be stable at -1.0 V and adsorbs CO* weaker than Cu(111) to form only 2e-CO_2RR products. The Gibbs energy diagrams at 0 V and -1.0 V were finally plotted to have an overview of the CO pathway (Equations B.13 – B.15), HCOOH pathway (Equations B.16 – B.18) and hydrogen evolution reaction (HER) (Equations B.19 – B.20) in Figure 7 respectively. The Gibbs energy diagrams for all the surface motifs considered at 0.0 V can be found as Figure B.9. The Gibbs energy changes for the CO, HCOOH and HER pathways at 0.0 V were tabulated in Table B.7, B.8 and B.9 respectively.

Before the CO_2RR pathways are discussed, the HER performance by different surface models were first evaluated. Pt(111) was included, which is known as the best prototypical electrocatalyst towards HER ($\Delta G(*H)$ = -0.38 eV). Although all the four surface motifs perform worse than Pt(111), the HER is exergonic at -1.0 V, which is why H_2 is always produced.

Moving to the CO pathway, it was found from the Gibbs energy diagrams at 0.0 V in Figure 7 that the potential determining step is the electrochemical hydrogenation of CO_2 to *COOH for $Cu_2Sb(100)$, S_{Sb1}, V_{Cu2} and S_{Sb2}. This is consistent with the finding for the CO Tafel slopes shown in Figure 5, with values close to 120 mV/dec for the three catalytic active phases. This Tafel slope indicates that the rate determining step is an electrochemical step, which is unlikely to be *CO desorption. At -1.0 V, the hydrogenation of CO_2 to *COOH for the four motifs is exergonic. The desorption of *CO is expected to involve an energy barrier of less than 0.10 eV that was easily overcome.

From the PEDs for the HCOOH pathway at 0.0 V, it was found that in general, the PDS for HCOOH formation is the chemical step involving hydrogenation of CO_2 to form HCOO*. The exception being $S_{Sb2}/Cu_2Sb(100)$, on which the hydrogenation of HCOO* is potential limiting. At -1.0 V, the HCOOH pathway on $S_{Sb2}/Cu_2Sb(100)$ is exergonic for all

elementary steps. This means that $S_{Sb2}/Cu_2Sb(100)$ can produce both CO and HCOOH, consistent with the negative values of $\Delta_{R1}G$ and $\Delta_{R2}G$ presented earlier. It was noted that HCOOH was always produced in the electrochemical tests at -1.0 V. It was found that the energy barrier of the potential determining step for the HCOOH pathway on pristine $Cu_2Sb(100)$, $S_{Sb1}/Cu_2Sb(100)$ and $V_{Cu2}/Cu_2Sb(100)$ surface motifs only require 0.01 eV, 0.02 eV and 0.20 eV at -1.0 V, which can be overcome at ambient conditions. Since the pristine $Cu_2Sb(100)$ surface motif should predominate in the three samples CS, SK and TH, such barrier can be overcome which explains why HCOOH was always produced in the electrochemical tests at -1.0 V just like H_2.

Overall, the computational results are consistent with the experiments, which showed a high selectivity towards the 2e-CO_2RR products even at a more negative applied voltage of -1.0 V. The results also help explain why the TH phase retains the highest percentage of sulfur after electrochemical tests, and they provide insight into the active phase and surfaces involved in the 2e-CO_2RR process.

5.4 Conclusion

In summary, sulfide-derived Cu–Sb electrocatalysts for CO_2 reduction have been studied in a GDE-based cell. Three different Cu–Sb–S phases were synthesized by a heat-up colloidal nanoparticle route which demonstrated different selectivity for the CO_2RR with CO as the main product. Based on elemental composition characterization after reduction, it is shown that these different selectivity patterns were due to the different elemental compositions when the parent phases are reduced. Less Cu minimizes phase segregation into detrimental S-doped Cu which forms $HCOO^-$ and H_2, while more sulfur disrupts crystallinity and encourages CO formation. This is seen in the TH sample having the highest residual sulfur and demonstrating the highest CO FE of about 80.5% at −1.0 V with a geometric partial current density of 37.6 mA cm^{-2}. These findings run contrary to the expectation that sulfide-derived electrocatalysts for the CO_2RR encourage $HCOO^-$, which has been the case for most of the studies in this category so far. This study challenges this assumption and could likely open the door to studies on other chalcogenides with surprising

selectivity patterns and could also point the way to engineering better catalysts to produce CO in sulfur-rich environments such as the flue gas CO_2RR.[32]

References

[1] T. Shinagawa, G. O. Larrazábal, A. J. Martín, F. Krumeich, and J. Pérez-Ramírez, "Sulfur-Modified Copper Catalysts for the Electrochemical Reduction of Carbon Dioxide to Formate," *ACS Catalysis,* vol. 8, no. 2, pp. 837-844, 2018/02/02 2018, doi: 10.1021/acscatal.7b03161.

[2] K. R. Phillips, Y. Katayama, J. Hwang, and Y. Shao-Horn, "Sulfide-Derived Copper for Electrochemical Conversion of CO2 to Formic Acid," *The Journal of Physical Chemistry Letters,* vol. 9, no. 15, pp. 4407-4412, 2018/08/02 2018, doi: 10.1021/acs.jpclett.8b01601.

[3] Y. Huang, Y. Deng, A. D. Handoko, G. K. L. Goh, and B. S. Yeo, "Rational Design of Sulfur-Doped Copper Catalysts for the Selective Electroreduction of Carbon Dioxide to Formate," *ChemSusChem,* vol. 11, no. 1, pp. 320-326, 2018, doi: https://doi.org/10.1002/cssc.201701314.

[4] W. Luc *et al.*, "SO2-Induced Selectivity Change in CO2 Electroreduction," *Journal of the American Chemical Society,* vol. 141, no. 25, pp. 9902-9909, 2019/06/26 2019, doi: 10.1021/jacs.9b03215.

[5] Y. Deng *et al.*, "On the Role of Sulfur for the Selective Electrochemical Reduction of CO2 to Formate on CuSx Catalysts," *ACS Applied Materials & Interfaces,* vol. 10, no. 34, pp. 28572-28581, 2018/08/29 2018, doi: 10.1021/acsami.8b08428.

[6] R. García-Muelas, F. Dattila, T. Shinagawa, A. J. Martín, J. Pérez-Ramírez, and N. López, "Origin of the Selective Electroreduction of Carbon Dioxide to Formate by Chalcogen Modified Copper," *The Journal of Physical Chemistry Letters,* vol. 9, no. 24, pp. 7153-7159, 2018/12/20 2018, doi: 10.1021/acs.jpclett.8b03212.

[7] M. T. Tang, H. Peng, P. S. Lamoureux, M. Bajdich, and F. Abild-Pedersen, "From electricity to fuels: Descriptors for C1 selectivity in electrochemical CO2 reduction," *Applied Catalysis B: Environmental,* vol. 279, p. 119384, 2020/12/15/ 2020, doi: https://doi.org/10.1016/j.apcatb.2020.119384.

[8] R. Kortlever, J. Shen, K. J. P. Schouten, F. Calle-Vallejo, and M. T. M. Koper, "Catalysts and Reaction Pathways for the Electrochemical Reduction of Carbon Dioxide," *The Journal of Physical Chemistry Letters,* vol. 6, no. 20, pp. 4073-4082, 2015/10/15 2015, doi: 10.1021/acs.jpclett.5b01559.

[9] H.-K. Lim, H. Shin, W. A. Goddard, Y. J. Hwang, B. K. Min, and H. Kim, "Embedding Covalency into Metal Catalysts for Efficient Electrochemical Conversion of CO2," *Journal of the American Chemical Society,* vol. 136, no. 32, pp. 11355-11361, 2014/08/13 2014, doi: 10.1021/ja503782w.

[10] X.-L. Zhang *et al.*, "Efficient acidic hydrogen evolution in proton exchange membrane electrolyzers over a sulfur-doped marcasite-type electrocatalyst," *Science Advances,* vol. 9, no. 27, p. eadh2885, 2023, doi: doi:10.1126/sciadv.adh2885.

[11] Y. Lai, R. J. R. Jones, Y. Wang, L. Zhou, M. H. Richter, and J. Gregoire, "The sensitivity of Cu for electrochemical carbon dioxide reduction to hydrocarbons as revealed by high throughput experiments," *Journal of Materials Chemistry A,* 10.1039/C9TA10111J vol. 7, no. 47, pp. 26785-26790, 2019, doi: 10.1039/C9TA10111J.

[12] S. Rasul, D. H. Anjum, A. Jedidi, Y. Minenkov, L. Cavallo, and K. Takanabe, "A Highly Selective Copper–Indium Bimetallic Electrocatalyst for the Electrochemical Reduction of Aqueous CO2 to CO," *Angewandte Chemie International Edition,* vol. 54, no. 7, pp. 2146-2150, 2015, doi: https://doi.org/10.1002/anie.201410233.

[13] S. Sarfraz, A. T. Garcia-Esparza, A. Jedidi, L. Cavallo, and K. Takanabe, "Cu–Sn Bimetallic Catalyst for Selective Aqueous Electroreduction of CO2 to CO," *ACS Catalysis,* vol. 6, no. 5, pp. 2842-2851, 2016/05/06 2016, doi: 10.1021/acscatal.6b00269.

[14] T. J. Whittles *et al.*, "Core Levels, Band Alignments, and Valence-Band States in CuSbS2 for Solar Cell Applications," *ACS Applied Materials & Interfaces,* vol. 9, no. 48, pp. 41916-41926, 2017/12/06 2017, doi: 10.1021/acsami.7b14208.

[15] C. H. M. van Oversteeg, F. E. Oropeza, J. P. Hofmann, E. J. M. Hensen, P. E. de Jongh, and C. de Mello Donega, "Water-Dispersible Copper Sulfide Nanocrystals via Ligand Exchange of 1-Dodecanethiol," *Chemistry of Materials,* vol. 31, no. 2, pp. 541-552, 2019/01/22 2019, doi: 10.1021/acs.chemmater.8b04614.

[16] Y. Li *et al.*, "Achieving Highly Selective Electrocatalytic CO2 Reduction by Tuning CuO-Sb2O3 Nanocomposites," *ACS Sustainable Chemistry & Engineering,* vol. 8, no. 12, pp. 4948-4954, 2020/03/30 2020, doi: 10.1021/acssuschemeng.0c00800.

[17] H. Li *et al.*, "Selective Reduction of CO2 to CO on an Sb-Modified Cu Electrode: Spontaneous Fabrication and Physical Insight," *ACS Catalysis,* vol. 11, no. 12, pp. 6846-6856, 2021/06/18 2021, doi: 10.1021/acscatal.1c00860.

[18] S. Mou *et al.*, "Cu2Sb decorated Cu nanowire arrays for selective electrocatalytic CO2 to CO conversion," *Nano Research,* vol. 14, no. 8, pp. 2831-2836, 2021/08/01 2021, doi: 10.1007/s12274-021-3295-1.

[19] H. Chen *et al.*, "Facile synthesis of an antimony-doped Cu/Cu2O catalyst with robust CO production in a broad range of potentials for CO2 electrochemical reduction," *Journal of Materials Chemistry A,* 10.1039/D1TA06181J vol. 9, no. 40, pp. 23234-23242, 2021, doi: 10.1039/D1TA06181J.

[20] Z. Zhang *et al.*, "Boosting carbon monoxide production during CO2 reduction reaction via Cu-Sb2O3 interface cooperation," *Journal of Colloid and Interface Science,* vol. 601, pp. 661-668, 2021/11/01/ 2021, doi: https://doi.org/10.1016/j.jcis.2021.05.118.

[21] J. Zeng *et al.*, "Novel Insights into Sb-Cu Catalysts for Electrochemical Reduction of CO2," *Applied Catalysis B: Environmental,* vol. 306, p. 121089, 2022/06/05/ 2022, doi: https://doi.org/10.1016/j.apcatb.2022.121089.

[22] J. Li *et al.*, "Selective CO2 electrolysis to CO using isolated antimony alloyed copper," *Nature Communications,* vol. 14, no. 1, p. 340, 2023/01/20 2023, doi: 10.1038/s41467-023-35960-z.

[23] R. He *et al.*, "Achieving the Widest Range of Syngas Proportions at High Current Density over Cadmium Sulfoselenide Nanorods in CO2 Electroreduction," *Advanced Materials,* vol. 30, no. 7, p. 1705872, 2018, doi: https://doi.org/10.1002/adma.201705872.

[24] C. W. Lee *et al.*, "New challenges of electrokinetic studies in investigating the reaction mechanism of electrochemical CO2 reduction," *Journal of Materials Chemistry A,* 10.1039/C8TA03480J vol. 6, no. 29, pp. 14043-14057, 2018, doi: 10.1039/C8TA03480J.

[25] E. M. Espinoza, J. A. Clark, J. Soliman, J. B. Derr, M. Morales, and V. I. Vullev, "Practical Aspects of Cyclic Voltammetry: How to Estimate Reduction Potentials When Irreversibility Prevails," *Journal of The Electrochemical Society,* vol. 166, no. 5, pp. H3175-H3187, 2019, doi: 10.1149/2.0241905jes.

[26] N. Elgrishi, K. J. Rountree, B. D. McCarthy, E. S. Rountree, T. T. Eisenhart, and J. L. Dempsey, "A Practical Beginner's Guide to Cyclic Voltammetry," *Journal of Chemical Education,* vol. 95, no. 2, pp. 197-206, 2018/02/13 2018, doi: 10.1021/acs.jchemed.7b00361.

[27] Y.-G. Kim, J. H. Baricuatro, and M. P. Soriaga, "Surface Reconstruction of Polycrystalline Cu Electrodes in Aqueous KHCO3 Electrolyte at Potentials in the Early Stages of CO2 Reduction," *Electrocatalysis,* vol. 9, no. 4, pp. 526-530, 2018/07/01 2018, doi: 10.1007/s12678-018-0469-z.

[28] B. J. Skinner, F. D. Luce, and E. Makovicky, "Studies of the Sulfosalts of Copper III; Phases and Phase Relations in the System Cu-Sb-S," *Economic Geology,* vol. 67, no. 7, pp. 924-938, 1972, doi: 10.2113/gsecongeo.67.7.924.

[29] W. B. Pearson, "The Cu2Sb and related structures," *Zeitschrift für Kristallographie - Crystalline Materials,* vol. 171, no. 1-4, pp. 23-40, 1985, doi: doi:10.1524/zkri.1985.171.14.23.

[30] K. P. Kuhl, T. Hatsukade, E. R. Cave, D. N. Abram, J. Kibsgaard, and T. F. Jaramillo, "Electrocatalytic conversion of carbon dioxide to methane and methanol on transition metal

surfaces," *Journal of the American Chemical Society,* vol. 136, no. 40, pp. 14107-13, Oct 8 2014, doi: 10.1021/ja505791r.

[31] M. T. Tang, H. Peng, P. S. Lamoureux, M. Bajdich, and F. Abild-Pedersen, "From electricity to fuels: Descriptors for C1 selectivity in electrochemical CO2 reduction," *Applied Catalysis B: Environmental,* vol. 279, 2020, doi: 10.1016/j.apcatb.2020.119384.

[32] B.-U. Choi, Y. C. Tan, H. Song, K. B. Lee, and J. Oh, "System Design Considerations for Enhancing Electroproduction of Formate from Simulated Flue Gas," *ACS Sustainable Chemistry & Engineering,* vol. 9, no. 5, pp. 2348-2357, 2021/02/08 2021, doi: 10.1021/acssuschemeng.0c08632.

Chapter 6 Elucidating the role of Bi and Sb in the product selectivity of Cu-M1-M2-S electrocatalysts

In this chapter, the $Cu_3(Sb_xBi_{1-x})S_3$ system with Sb and Bi is investigated to determine the role of the second metal in this catalyst system. While Sb alloys well with Cu to produce CO, Bi is less miscible with Cu and tunes it towards $HCOO^-$ instead. Furthermore, the production of a small amount of CH_4 and C_2H_4 when Sb is absent may be an indicator that some amount of phase segregated Cu is induced by the presence of Bi. $HCOO^-$ Faradaic efficiency peaks at 0.6Bi 0.3Sb , where the H_2 Faradaic efficiency increases in the 1Bi 0Sb sample. This coincides with a decrease in Bi content in EDX characterization post-reduction. This reveals that Bi loss in all samples is larger than Sb loss, which again could be a result of the lower miscibility of Bi with Cu.

6.1 Introduction

While the three metals in the fifth row of the periodic table (In, Sn, Sb) alloy with Cu to give CO, the sixth row (Bi) can give different results, especially if compared to Sb. Cu-Bi is known to produce $HCOO^-$ strongly,[1, 2] possibly due to Bi's inability to form an intermetallic with Cu. This means that the distribution of Bi is unlikely to be regular on the surface, while its strong preference for O-binding and $HCOO^-$ also tunes the selectivity of the Cu sites towards $HCOO^-$. While most studies find $HCOO^-$ as the main product of Cu-Bi alloys, there are also reports of CH_4 or C_2H_4 as the main product.[3, 4]

Reports on electrochemical CO_2 reduction on Cu-Bi-S include two publications on Bi–CuS nanocrystals, which reported near-unity and 85% Faradaic efficiency respectively for $HCOO^-$ production, which indicates that Cu-Bi-S could be a viable strategy for promoting $HCOO^-$ selectivity.[5, 6]

Based on this, by varying the amount of Sb and Bi, control of the selectivity of the sulfide-derived catalyst between CO vs $HCOO^-$. It is hypothesized that the post-reduction XRD of the two will be different. Specifically, while Cu forms an intermetallic alloy with Sb in the form of Cu_2Sb, this will not be true for Bi and it is expected to find two separate metals Cu and Bi. This is due to the different phase diagrams of Cu-Sb and Cu-Bi as shown in Figures 6.1 and 6.2:

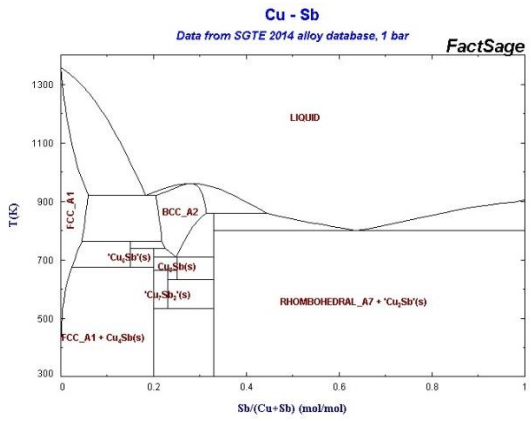

Figure 6.1: Phase diagram of Cu-Sb taken from the SGTE 2014 alloy database

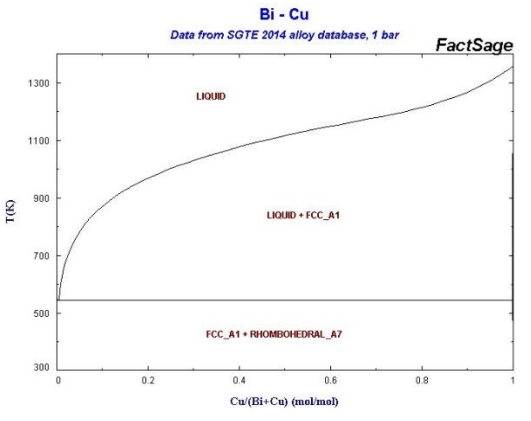

Figure 6.2: Phase diagram of Cu-Bi taken from the SGTE 2014 alloy database

Four Cu–(Sb, Bi)–S samples, 0Bi 1Sb (Cu:Sb:Bi:S of 41:14:0:45), 0.3Bi 0.6Sb (Cu:Sb:Bi:S of 43:10:5:43), 0.6Bi 0.3Sb (Cu:Sb:Bi:S of 43:5:10:43), and 1Bi 0Sb (Cu:Sb:Bi:S of 43:0:14:43) were included in this study. Precursors were mixed for synthesis according to the metal ratios indicated.

6.2 Characterization of Cu-(Sb, Bi)-S catalysts

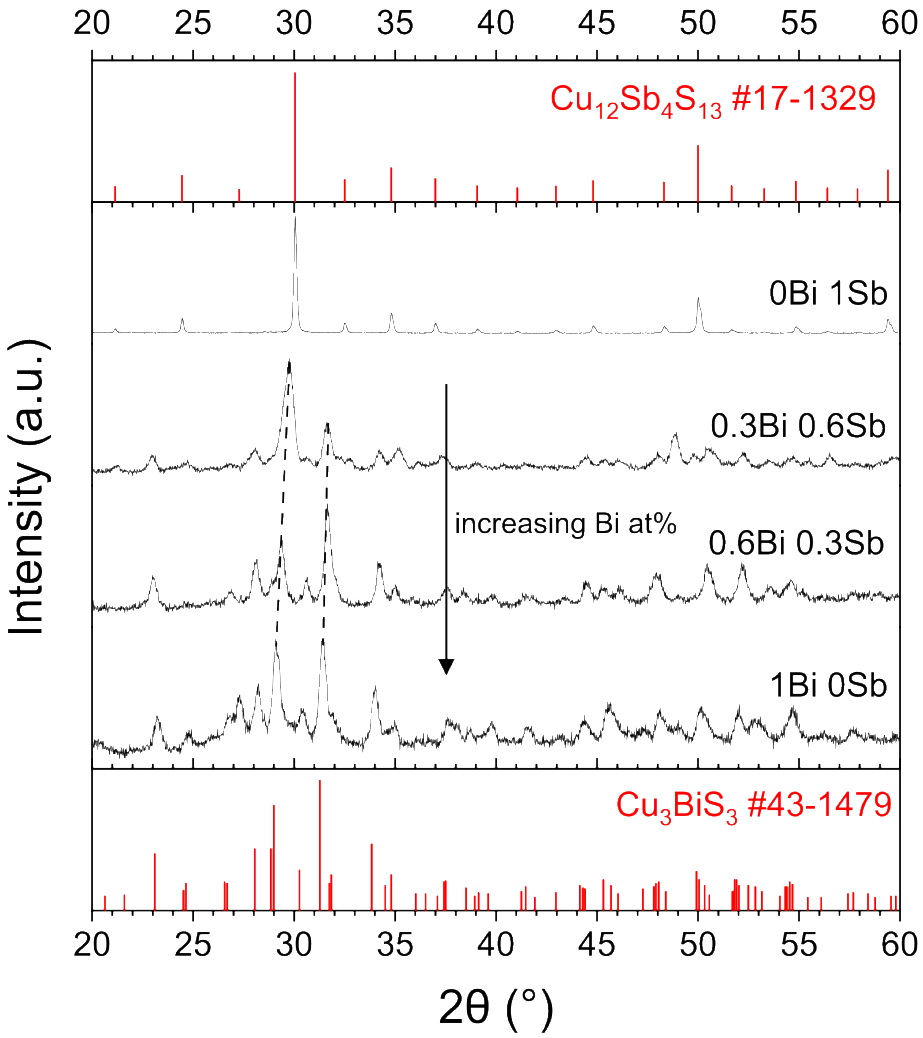

Figure 6.3: XRD plot of the four Cu-Sb/Bi powder samples

As can be seen from the XRDs in Figure 6.3, the 0Bi 1Sb and 1Bi 0Sb samples have XRD

structures that are entirely of their respective sulfides (tetrahedrite $Cu_{12}Sb_4S_{13}$ and wittichenite Cu_3BiS_3 respectively), while the samples with both Sb and Bi (0.3Bi 0.6Sb and 0.6Bi 0.3Sb) have structures that are intermediate of the two, which are possibly mixed phase. The two main peaks between 28° to 32° show a progressive shift towards a lower angle as more Bi is added as Bi has a larger ionic radius compared to Sb, which increases the d spacing and thus decreases 2θ according to the equation $d = \frac{\lambda}{2 \sin \theta}$.

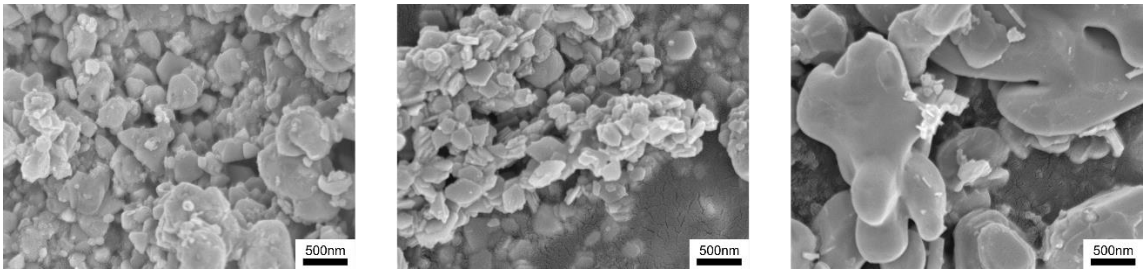

Figure 6.4: SEM images of (a) 0.3Bi 0.6Sb, (b) 0.6Bi 0.3Sb and (c) 1Bi 0Sb powder samples

SEM images of the samples are shown in Figure 6.4. The morphology of the 0.3Bi 0.6Sb sample features rock-like particles the size of about 400nm, while the 0.6Bi 0.3Sb sample shows flat disks also of about 400nm. However, the 1Bi 0Sb sample has very large particles about 1um or above, due to the long duration of the solvothermal synthesis.

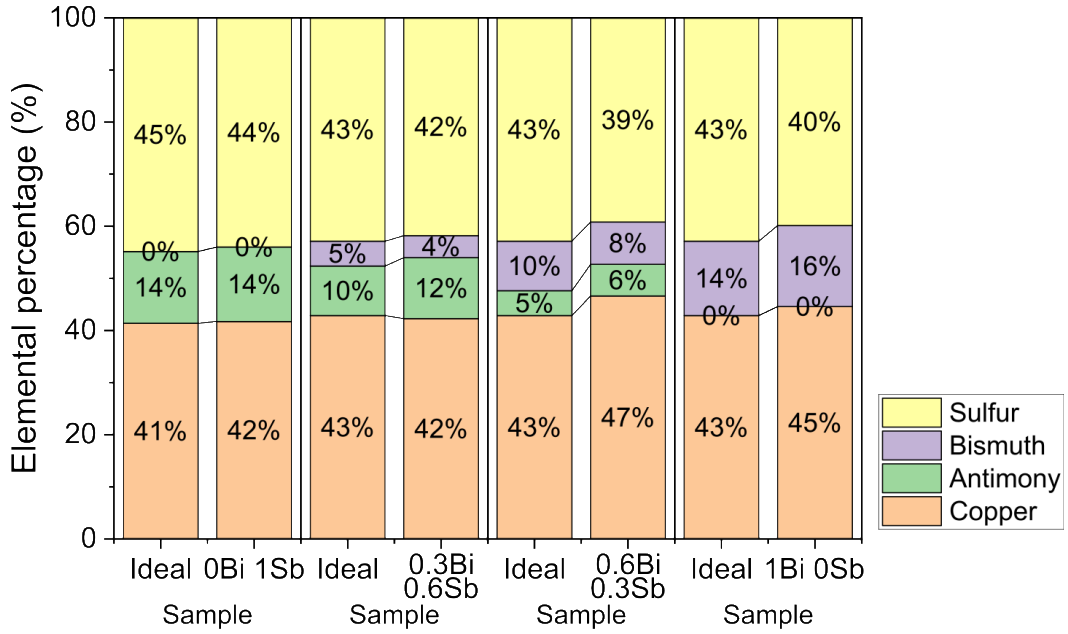

Figure 6.5: EDX ratios of the four Cu-Sb/Bi-S powder samples

The measured EDX elemental ratios of the samples in Figure 6.5 confirm that the Sb-Bi ratio in the samples are approximately according to the stoichiometry of the precursor metal salt ratios, thus confirming successful synthesis of the Cu-(Sb, Bi)-S catalysts.

6.3 Electrochemical performance of Cu-(Sb, Bi)-S catalysts

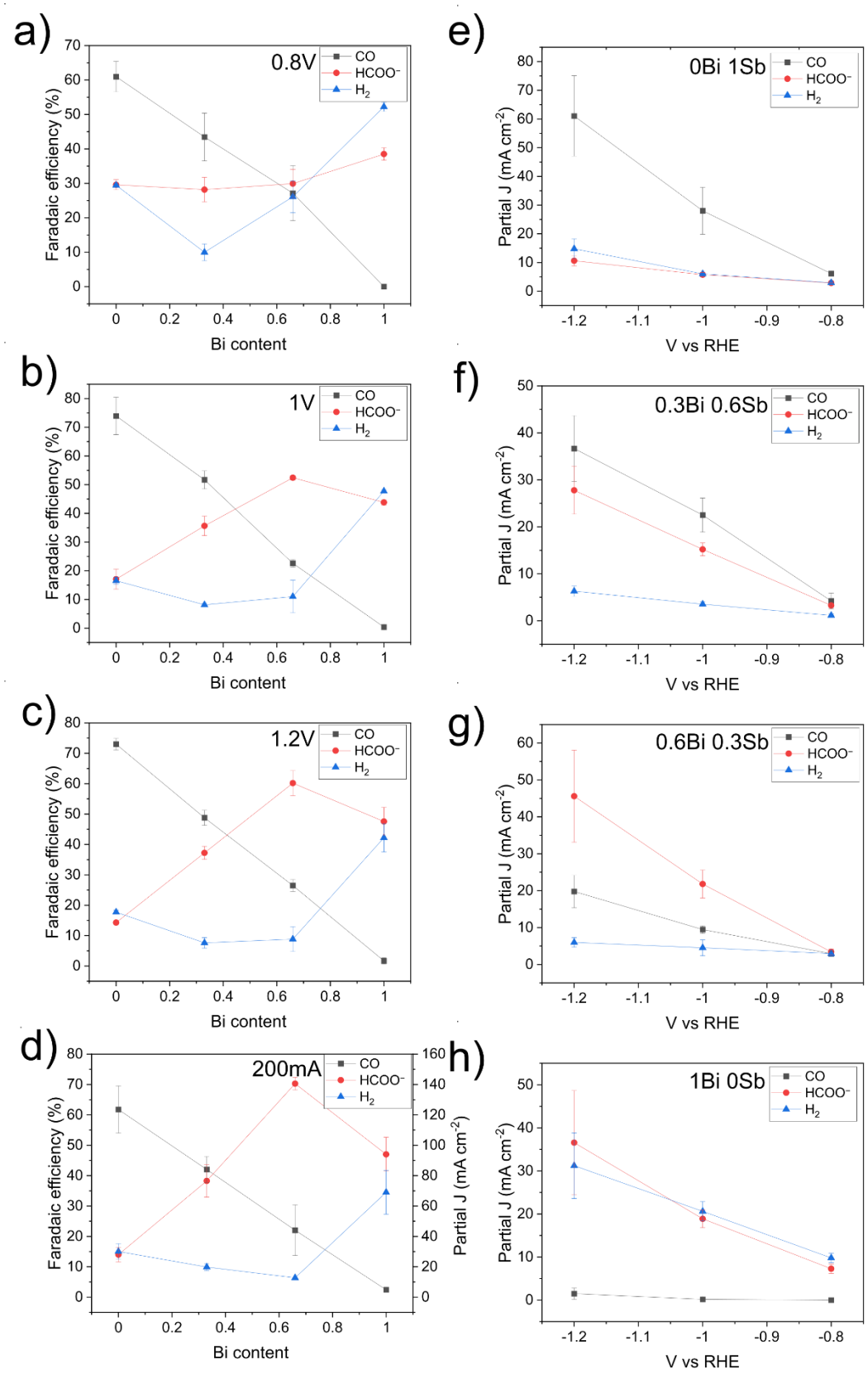

Figure 6.6: Electrochemical CO_2RR performance of Cu-Sb/Bi samples. (a-c) Faradaic efficiencies of samples plotted against Bi content for chronoamperometric -0.8V, -1V and -1.2V runs (d) Faradaic efficiency of samples plotted against Bi content for chronopotentiometric 200mA runs (e-h) Partial current densities of samples plotted against applied voltage for 0Bi 1Sb, 0.3Bi 0.6Sb, 0.6Bi 0.3Sb and 1Bi 0Sb samples

The electrochemical activity for CO_2RR was evaluated for Cu-Sb/Bi sulfide samples with Sb:Bi of different ratios, shown in Figure 6.6. It was found that the 0Bi 1Sb sample shows the highest CO Faradaic efficiency of 75% at -1V, while the 0.6Bi 0.3Sb sample shows the highest $HCOO^-$ Faradaic efficiency of 60% at -1.2V. In the 1Bi 0Sb sample, the amount of $HCOO^-$ decreases while the amount of H_2 increases such that both are produced at approximately similar amounts.

The unexpected behaviour of 1Bi 0Sb, which produces less $HCOO^-$ and more H_2 than anticipated, suggests an intriguing underlying process. This is explained further by the post-reduction EDX characterization in section 6.4, where a reduced amount of Bi contributes to this behaviour as 1Bi 0Sb has a similar Bi at% as 0.3Bi 0.6Sb.

The similarity between the 0Bi 1Sb sample and the 1Bi 0Sb sample is that both have roughly equal amounts of $HCOO^-$ and H_2 produced, but 0.3Bi 0.6Sb and 0.6Bi 0.3Sb samples produce more $HCOO^-$ than H_2. This could again point to a commonality in the H_2 and $HCOO^-$ paths, with the paths diverging in the mixed samples (having both Sb and Bi). This could indicate that the presence of both Sb and Bi has a beneficial effect on $HCOO^-$ but not H_2, which could indicate stabilization of *OCHO relative to *H which favours $HCOO^-$.[7, 8]

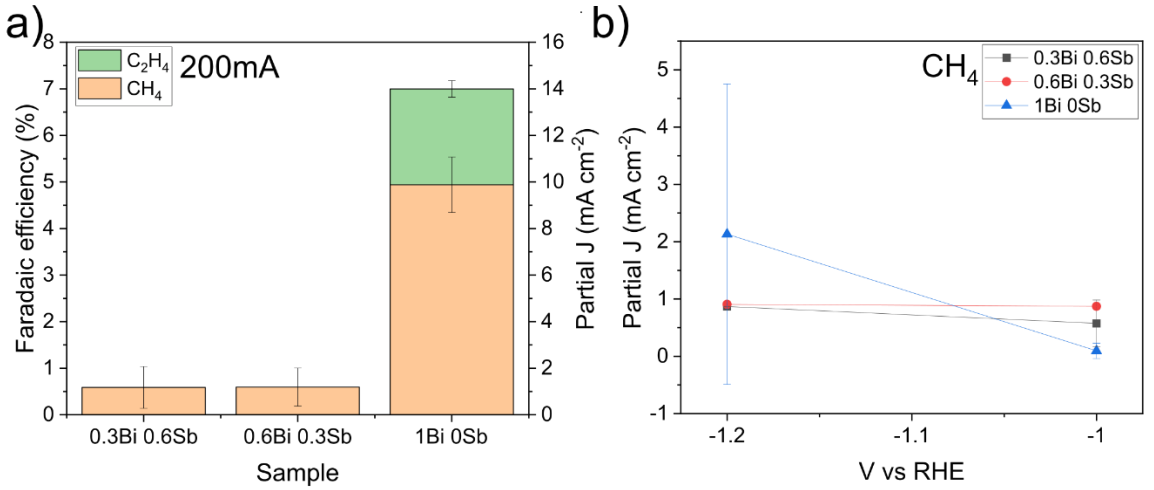

Figure 6.7: (a) Faradaic efficiency of CH_4 and C_2H_4 of samples for chronopotentiometric 200mA runs. (b) Partial current density of CH_4 of samples for chronoamperometric -1V and -1.2V runs

Unlike 0Bi 1Sb and the Cu-Sb-S system, when Bi is added, it is observed that at potentials more negative than -1V vs RHE, CH_4 is produced for the samples. Additionally, for the applied 200mA experiments, it is further observed that the 1Bi 0Sb sample also produces C_2H_4. The results are shown in Figure 6.7. It is likely that when Bi is added, some amount of Cu (with possibly minute amount of Bi) is formed which then serves as the active site for CH_4 formation.[3] At an applied current of 200mA, it is possible that enough Cu phase segregates that C_2H_4 can be produced on 1Bi 0Sb. The formation of reduced products thus possibly points to a certain amount of Cu formation (with possibly minute Bi) as reduced products are generally produced on Cu with no S and possibly minimal Bi. It is likely that if sulfur was completely absent in the catalysts, more CH_4 would be produced, as Goddard and co-workers reported a copper-bismuth catalyst that is able to produce CH_4 with a Faradaic efficiency of 70.6% at −1.2 V vs RHE.[3]

6.4 Post-reduction characterization

.

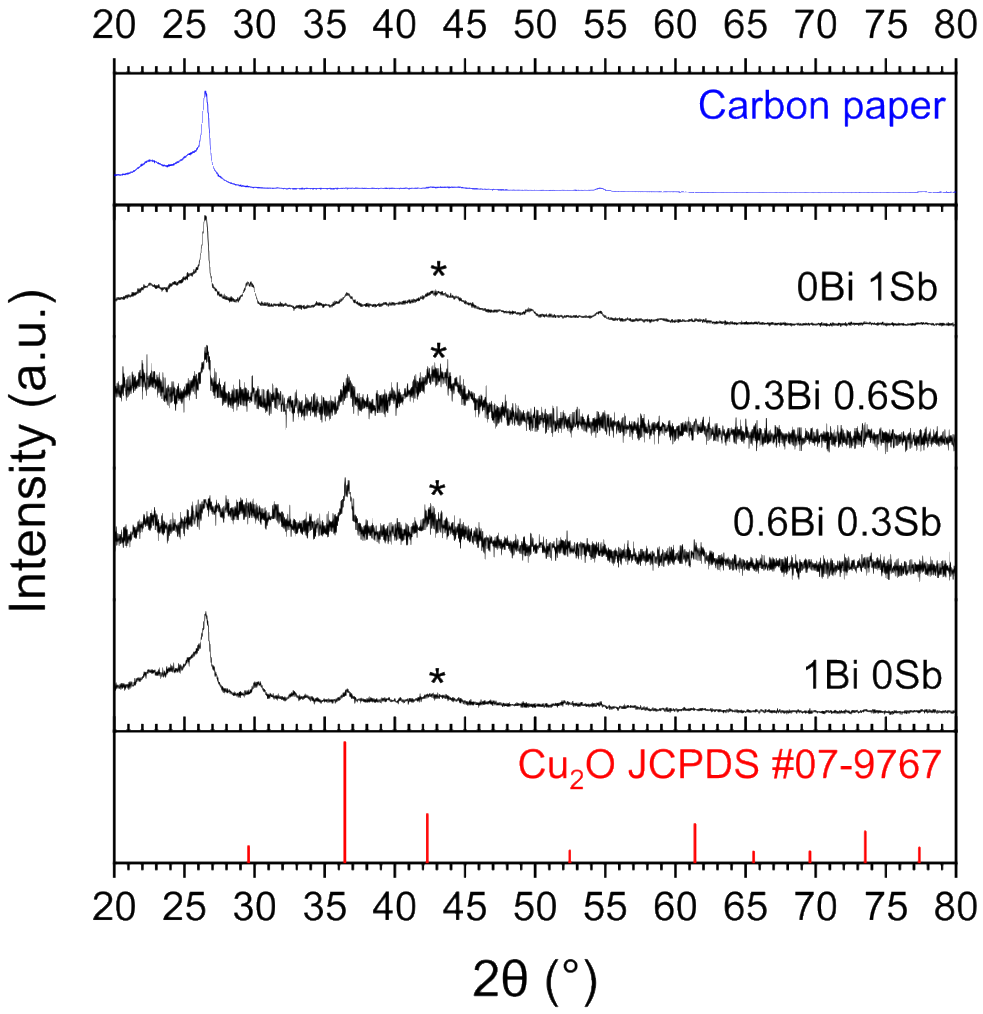

Figure 6.8: Post-reduction XRD of Cu-Sb/Bi S samples on carbon paper. The broad hump in the XRDs at 40-47° is marked with asterisks.

XRD of the samples on carbon paper taken after electrochemical CO_2 reduction in Figure 6.8 show a conversion to metallic phase with some Cu_2O present, indicating post-CO_2RR reoxidation of samples. Unexpectedly and contrary to hypothesis at the beginning of the chapter, the phase after reduction is a broad hump found between a 2θ of 40-47°, even for the fully Cu-Bi-S sample, which indicates that instead of clear phase segregation between Cu and Bi as is expected from their phase diagram, they form an amorphous or minimally crystalline phase (with unclear miscibility) with the same hump as the other samples.

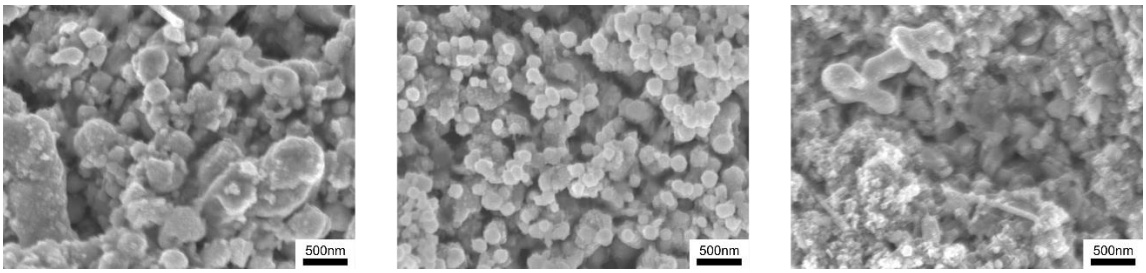

Figure 6.9: SEM images of (a) 0.3Bi 0.6Sb, (b) 0.6Bi 0.3Sb and (c) 1Bi 0Sb samples on carbon paper after reduction

Figure 6.9 shows the SEM images of the samples on carbon paper after reduction. The morphology of the 0.3Bi 0.6Sb and 0.6Bi 0.3Sb samples did not change by much, only that the phase seems to have changed and along with it minor surface changes (for eg, the disks in 0.6Bi 0.3Sb have become more rounded), with the particle size being largely the same. However, 1Bi 0Sb seems to have undergone a more drastic morphology change, with the particles now having been broken up into much smaller particles that are closer in size to 0.3Bi 0.6Sb and 0.6Bi 0.3Sb. This could indicate an increased instability of the 1Bi 0Sb reduced alloy which resulted in more drastic reconstruction.

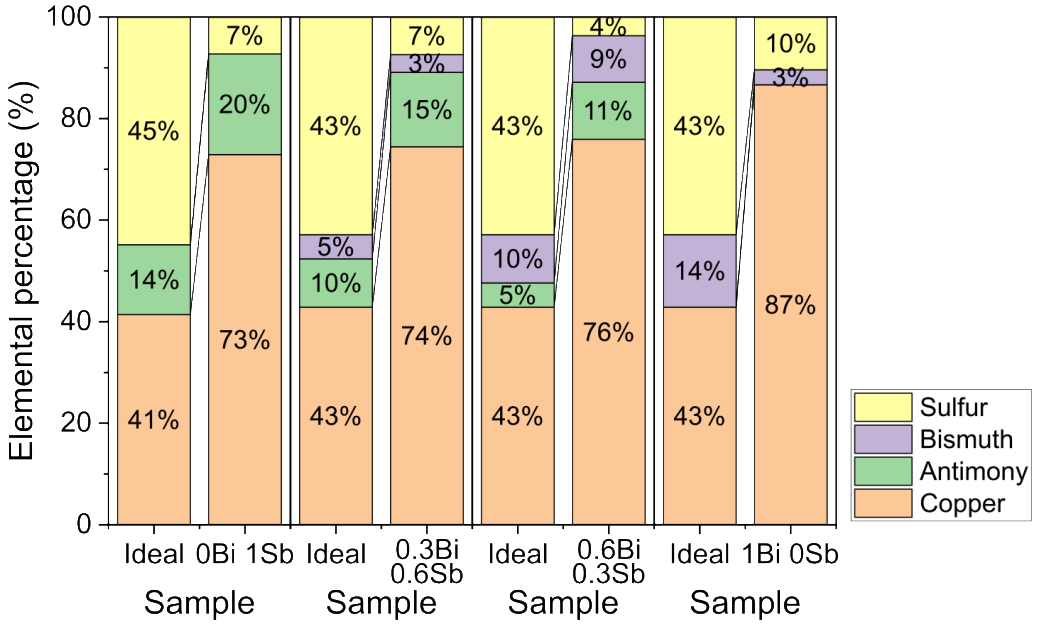

Figure 6.10: EDX ratios of the four Cu-Sb/Bi-S powder samples after reduction

EDX analysis of the catalysts post-reduction at -1V in Figure 6.10 (compared against ideal compositions calculated from stoichiometry e.g. $Cu_{12}Sb_4S_{13}$ for 0Bi 1Sb and Cu_3BiS_3 for

1Bi 0Sb) reveals that from 0Bi 1Sb to 1Bi 0Sb, while antimony content decreases linearly as according to stoichiometry, the bismuth content changes from stoichiometry. It peaks at 9% in the 0.6Bi 0.3Sb sample and then decreases to 3% in the 1Bi 0Sb sample. The decrease in antimony correlates with the decrease in CO production, consistent with the notion that CO production only happens on Cu-Sb alloy. The maximum amount of $HCOO^-$ is produced with the 0.6Bi 0.3Sb sample, which also has the highest Bi content. Thus, $HCOO^-$ production can be seen to be correlated with Bi content. Plots of CO FE against Sb, as well as $HCOO^-$ FE against Bi, are shown in Figure 6.11:

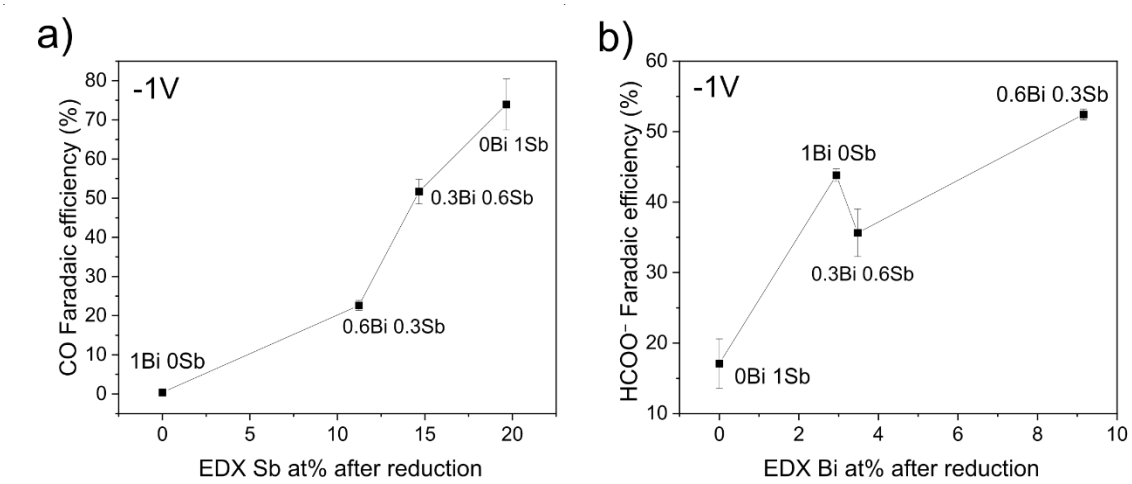

Figure 6.11: Plot of (a) CO FE against Sb at% and (b) HCOO− FE against Bi at%

More insight can be gained by comparing the CO_2RR results and the EDX results for 0.3Bi 0.6Sb and 1Bi 0Sb, which has similar amount of Bi but with Sb replaced by Cu. Electrochemical CO_2RR results show that the amount of $HCOO^-$ is largely similar, but CO production in 0.3Bi 0.6Sb is replaced with H_2 production in 1Bi 0Sb. This indicates that Sb facilitates CO formation but replacing it with Cu results in increased H_2 production.

Tabulating the Sb/Cu and Bi/Cu ratios:

Table 6.1: Table of Sb/Cu vs Bi/Cu, EDX vs ideal

Sample	Sb/Cu EDX	Sb/Cu ideal	Bi/Cu EDX	Bi/Cu ideal
0Bi 1Sb	0.272	0.333	0	0
0.3Bi 0.6Sb	0.197	0.222	0.047	0.111
0.6Bi 0.3Sb	0.148	0.111	0.121	0.222
1Bi 0Sb	0	0	0.034	0.333

In table 6.1, the ideal ratios are taken from the ratios of the elements in the sulfide synthesis. As can be seen, the Sb/Cu ratios are quite close to ideal even after CO_2RR, which implies minimal Sb loss relative to Cu. However, the Bi/Cu ratios are very far from the ideal, ranging from one tenth to one half of the ideal ratio. In other words, the majority of Bi is lost. Instead of the phase segregation of Bi and Cu, what the results show is a large loss of Bi and a small amount of Bi possibly being incorporated into Cu or phase segregated.

6.5 Comparison with literature

Table 6.2 compares with the literature for Cu-Bi and Cu-Bi-S catalysts:

Table 6.2: Cu-Bi catalysts reported in literature

Catalyst	Electrolyte	Potential (V vs. RHE)	Faradaic efficiency of main product	CO_2RR main product	Reference
Cu-Bi catalysts					
Cu-Bi bimetallic microspheres	0.5 M $NaHCO_3$	–0.93	95%	$HCOO^-$	[1]
Lattice-dislocated Bi nanowires on Cu foam	Not mentioned	−0.69	95%	$HCOO^-$	[2]
Cu nanowire bridged Bi nanosheet arrays	0.5 M $KHCO_3$	-0.86	87%	$HCOO^-$	[9]
Amorphous bimetallic Cu-Bi	0.5 M $KHCO_3$	-1.0	94.7%	$HCOO^-$	[10]
MOF derived bimetallic CuBi	0.5M $KHCO_3$	-0.77	100%	$HCOO^-$	[11]
Cu–Bi dendrites	0.1M $KHCO_3$	-0.9	90%	$HCOO^-$	[12]
Cu–Bi Nanoalloys	0.5 M $KHCO_3$	-1.2	70.6%	CH_4	[3]
Bi single atoms anchored on CuO	0.1 M $KHCO_3$	400mAcm^{-2}	60%	C_2H_4	[4]
Cu–Bi bimetallic aerogels	1M KOH	N/A	Multiple products	Tunable	[13]
Cu/Bi MOF	0.5 M $KHCO_3$	N/A	Multiple products	Ethanol and methanol	[14]
Cu-Bi-S catalysts					
Bi–Cu_2S nanocrystals	0.1 M $KHCO_3$	−1.2	Near unity	$HCOO^-$	[5]

Bi/Cu_xS_y heterointerfaces	0.5 M $KHCO_3$	-0.8 to -1.2	Over 85%	$HCOO^-$	[6]

As can be seen from Table 6.2, the majority product for bimetallic Cu-Bi catalysts is $HCOO^-$. However, as Cu becomes dominant (>85%), reduced products get produced as seen in the last four Cu-Bi papers in Table 6.2. While the amount of reduced products that were obtained in this chapter were not as high, it is likely that this may be due to sulfur suppressing these products in favour of $HCOO^-$ which is very similar to the phenomenon on pure Cu. Thus, there are hints that this system, despite being amorphous, may at least be partially phase-segregated. The highest $HCOO^-$ FE reached by the 0.6Bi 0.3Sb sample, which was about 70%, is lower than the literature, indicating that further work needs to be done to optimize the Bi:Sb ratio between 66% and 100% to increase the $HCOO^-$ Faradaic efficiency.

6.6 Discussion on CO vs $HCOO^-$ selectivity

The difference in selectivity between Cu-Sb and Cu-Bi catalysts is likely due to the solubility of Sb in Cu to form an alloy Cu_2Sb. On one hand, Cu-In, Cu-Sn and Cu-Sb form alloys as discussed in Section 2.5.1. This means that the C-binding of Cu is weakened by the alloying In, Sn or Sb which tunes it towards CO instead of reduced products (C_2H_4, CH_4, etc), while the $HCOO^-$ selectivity of In, Sn or Sb is reduced due to the presence of Cu. This results in CO as the main product with some amount of $HCOO^-$ as the secondary product.

However, Bi is not soluble in Cu. This means that its preference for O-binding likely dominates and suppresses formation of CO or reduced products on Cu atoms due to the preference for O-binding on neighbouring Bi atoms.[11]

This is likely the main reason for the difference observed in the sulfide-derived catalysts as well, but because both Cu-Sb-S (specifically derived from the tetrahedrite phase) and Cu-Bi-S reduce to form a more or less amorphous catalyst there is not enough evidence to support this. TEM-EDX or XPS may be necessary to discern whether Bi and Sb have a solubility difference in the amorphous catalyst during reaction.

6.7 Conclusion

The substitution of Sb with Bi in Cu-Sb-S was studied to investigate the change in catalyst performance and behaviour. Three samples with increasing Bi content, 0.3Bi 0.6Sb, 0.6Bi 0.3Sb and wittichenite 1Bi 0Sb were synthesized. Including tetrahedrite 0Bi 1Sb in the results, the four samples were compared. It is seen that increasing amounts of Bi after reduction correlates with increasing $HCOO^-$, while decreasing amounts of Sb after reduction correlates with decreasing CO. H_2 production in the pure 0Bi 1Sb and 1Bi 0Sb samples closely tracks $HCOO^-$ production, with the two deviating in the samples containing both Sb and Bi (0.3Bi 0.6Sb and 0.6Bi 0.3Sb). Post-reduction XRD shows a broad hump which may indicate that Bi may be mixed to some extent with Cu and Sb, despite the phase diagram showing complete immiscibility with Cu. The highest $HCOO^-$-performing catalyst is 0.6Bi 0.3Sb with a $HCOO^-$ FE of 70% at an applied geometric current density of 200mA. This is lower than Cu-Bi bimetallic alloys in literature, which may be increased by optimizing the Bi:Sb ratio to be between 66% and 100%.

References

[1] L. Jia *et al.*, "Copper-Bismuth Bimetallic Microspheres for Selective Electrocatalytic Reduction of CO2 to Formate," *Chinese Journal of Chemistry,* vol. 37, no. 5, pp. 497-500, 2019, doi: https://doi.org/10.1002/cjoc.201900010.

[2] X. Zhang, X. Sun, S.-X. Guo, A. M. Bond, and J. Zhang, "Formation of lattice-dislocated bismuth nanowires on copper foam for enhanced electrocatalytic CO2 reduction at low overpotential," *Energy & Environmental Science,* 10.1039/C9EE00018F vol. 12, no. 4, pp. 1334-1340, 2019, doi: 10.1039/C9EE00018F.

[3] Z. Wang *et al.*, "Highly Selective Electrocatalytic Reduction of CO2 into Methane on Cu–Bi Nanoalloys," *The Journal of Physical Chemistry Letters,* vol. 11, no. 17, pp. 7261-7266, 2020/09/03 2020, doi: 10.1021/acs.jpclett.0c01261.

[4] W. Li *et al.*, "Lowering C−C coupling barriers for efficient electrochemical CO2 reduction to C2H4 by jointly engineering single Bi atoms and oxygen vacancies on CuO," *Applied Catalysis B: Environmental,* vol. 318, p. 121823, 2022/12/05/ 2022, doi: https://doi.org/10.1016/j.apcatb.2022.121823.

[5] X. Han *et al.*, "Heterostructured Bi–Cu2S nanocrystals for efficient CO2 electroreduction to formate," *Nanoscale Horizons,* 10.1039/D1NH00661D vol. 7, no. 5, pp. 508-514, 2022, doi: 10.1039/D1NH00661D.

[6] X. Yang *et al.*, "In-situ electrochemical restructuring of Cu2BiSx solid solution into Bi/CuxSy heterointerfaces enabling stabilization intermediates for high-performance CO2 electroreduction to formate," *Nano Research,* vol. 16, no. 5, pp. 7974-7981, 2023/05/01 2023, doi: 10.1007/s12274-022-5337-8.

[7] R. Kortlever, J. Shen, K. J. P. Schouten, F. Calle-Vallejo, and M. T. M. Koper, "Catalysts and Reaction Pathways for the Electrochemical Reduction of Carbon Dioxide," *The Journal of Physical Chemistry Letters,* vol. 6, no. 20, pp. 4073-4082, 2015/10/15 2015, doi: 10.1021/acs.jpclett.5b01559.

[8] M. T. Tang, H. Peng, P. S. Lamoureux, M. Bajdich, and F. Abild-Pedersen, "From electricity to fuels: Descriptors for C1 selectivity in electrochemical CO2 reduction," *Applied Catalysis B: Environmental,* vol. 279, p. 119384, 2020/12/15/ 2020, doi: https://doi.org/10.1016/j.apcatb.2020.119384.

[9] L. Li, F. Cai, F. Qi, and D.-K. Ma, "Cu nanowire bridged Bi nanosheet arrays for efficient electrochemical CO2 reduction toward formate," *Journal of Alloys and Compounds,* vol. 841, p. 155789, 2020/11/15/ 2020, doi: https://doi.org/10.1016/j.jallcom.2020.155789.

[10] Y. Xiong *et al.*, "Rapid synthesis of amorphous bimetallic copper-bismuth electrocatalysts for efficient electrochemical CO2 reduction to formate in a wide potential window," *Journal of CO2 Utilization,* vol. 51, p. 101621, 2021/09/01/ 2021, doi: https://doi.org/10.1016/j.jcou.2021.101621.

[11] Z. Yang *et al.*, "MOF derived bimetallic CuBi catalysts with ultra-wide potential window for high-efficient electrochemical reduction of CO2 to formate," *Applied Catalysis B: Environmental,* vol. 298, p. 120571, 2021/12/05/ 2021, doi: https://doi.org/10.1016/j.apcatb.2021.120571.

[12] Z. B. Hoffman, T. S. Gray, Y. Xu, Q. Lin, T. B. Gunnoe, and G. Zangari, "High Selectivity Towards Formate Production by Electrochemical Reduction of Carbon Dioxide at Copper–Bismuth Dendrites," *ChemSusChem,* vol. 12, no. 1, pp. 231-239, 2019, doi: https://doi-org.remotexs.ntu.edu.sg/10.1002/cssc.201801708.

[13] Y. Wang *et al.*, "Tunable selectivity on copper–bismuth bimetallic aerogels for electrochemical CO2 reduction," *Applied Catalysis B: Environmental,* vol. 317, p. 121650, 2022/11/15/ 2022, doi: https://doi.org/10.1016/j.apcatb.2022.121650.

[14] J. Albo, M. Perfecto-Irigaray, G. Beobide, and A. Irabien, "Cu/Bi metal-organic framework-based systems for an enhanced electrochemical transformation of CO2 to alcohols," *Journal of CO2 Utilization,* vol. 33, pp. 157-165, 2019/10/01/ 2019, doi: https://doi.org/10.1016/j.jcou.2019.05.025.

Chapter 7 Conclusions and Recommendations

This chapter concludes the thesis with a discussion of the lessons derived from the study; namely that sulfur is not generally desirable in electrochemical CO_2 reduction catalysts. Recommendations such as to use sulfides in photoelectrochemical CO_2 reduction, or to use trimetallics in electrochemical CO_2 reduction, are raised. The importance of in-situ characterization is also mentioned.

7.1 Summary of study and findings

This study focuses on Cu-M-chalcogenides (sulfides and selenides) for electrochemical CO_2 reduction by using a second metal to tune binding, with sulfur to impart a degree of covalency to improve selectivity. Generally, sulfides seem to promote $HCOO^-$ and block the CO-pathway which is a necessary intermediate to both CO and reduced products.[1] This is primarily seen on copper sulfide-derived catalysts.[2-4] **Chapter 1** highlighted the hypotheses and scope of this thesis. The hope of this study was that the addition of the second metal can yield surprising results which allow the CO-pathway and thus produce CO or reduced products. The second goal of this study was also to look for trends in the choice of second metal and the electrochemical CO_2RR performance of the bimetallic chalcogenides. **Chapter 2** discusses the mechanism of CO_2 reduction, catalyst reconstruction, background of existing two-element catalysts for electrochemical CO_2 reduction and elucidated the scope of study of three-element bimetallic chalcogenide catalysts.

Chapter 4 starts the study by choosing 9 metals as the second metal for the catalysts. (In, Sn, Sb) are shown by literature to alloy with Cu to produce CO which could have some CO selectivity also in the sulfide form. (Bi) with Cu is shown by literature to produce $HCOO^-$. Cu-(Ga, Ge, Ag, Co, Fe)-S were tested to to widen the search to other metals that do not demonstrate good selectivities when alloyed with Cu but were nonetheless included in case it led to surprising results. It is found that the first group demonstrated decent promising results for further investigation, especially Sb as Cu-Sb-S showed good CO selectivity. The other two groups of elements did not show significant CO_2RR activity. This could be due to optimal d-band alignment for the fifth row main group elements and favourable alloying with Cu to form intermetallic compounds, both of which can synergize well with Cu for optimal binding. However, for (In, Sn), due to lack of reduction of the parent sulfide, excess sulfur possibly results in excess *H bound on the surface which then yields either $HCOO^-$ or H_2. The second half of the chapter contrasts S vs Se in the Cu-Sb-S/Se system. Se produced more H_2 byproduct than S in line with literature results for other chalcogenide-derived catalysts, which also has different interactions with Cu and Sb (notably, Sb is less

stable at higher voltages with Se), but does not provide any selectivity advantages over S. Sulfur was thus chosen as the better performing chalcogenide.

Chapter 5 focuses on an in-depth study of the Cu-Sb-S system. Three starting phases were synthesized: skinnerite (SK, Cu_3SbS_3), tetrahedrite (TH, $Cu_{12}Sb_4S_{13}$) and chalcostibite ($CuSbS_2$). It is found that they have different CO selectivities with TH the most selective at about 75-80%. It is also found that like copper sulfide-derived catalysts in the literature, Cu-Sb-S reduces in the presence of an applied voltage to become S-doped Cu_2Sb. Phase segregation in the SK sample was found to result in lower CO selectivity as more byproducts $HCOO^-$ and H_2 were produced from segregated S-doped Cu. Higher S content (and lower Sb content) in TH can be correlated to lowered crystallinity which may explain the improved CO selectivity in TH. Cu-Sb-S is the only other sulfide-derived catalyst other than CdS to consistently produce CO as most sulfide-derived catalysts (such as In-S, Sn-S, Bi-S) produce $HCOO^-$.

Experiments are followed up in **Chapter 6** where Sb is substituted with Bi. One crucial difference between Bi and Sb with respect to Cu is that it does not form an intermetallic alloy with Cu. Thus, while Cu_2Sb is formed when Cu-Sb-S reduces, it was not expected that Cu_xBi would form. This results in phase segregated S-doped Cu and S-doped Bi, the latter of which drives selectivity to $HCOO^-$. However, more byproduct H_2 was obtained than expected, likely because of the presence of S-doped Cu.

7.2 Evaluation of study with hypotheses

It is found that the choice to prioritize Cu-In, Cu-Sn and Cu-Sb to search for CO-selective materials was a success as Cu-Sb-S indeed did demonstrate CO selectivity despite the general tendency for sulfides to produce $HCOO^-$. However, Cu-In and Cu-Sn have low CO-selectivities, which is found to be due to the excess sulfur present due to the parent sulfide not reducing, which also confirms the hypothesis that CO selectivity is only improved when the parent sulfide reduces. However, while not included in the hypothesis, it was hoped to also find reduced products among other Cu-M-S as well, which was not found for second M=Ga, Ge, Ag, Fe, Co elements. This could be due to two factors:

1) the stoichiometric limitations of sulfides which do not allow us to dope in smaller amounts
2) the general difficulty of getting CuS-derived catalysts to produce CO

In bimetallic catalysts, the strategy to produce reduced products is to have a majority of Cu (about 90%) coupled with doping of other metals (Pd, Au, Zn, In, Sn, Sb, Al, Ga, Ge, etc).[5] This means that the Cu does the heavy work of binding the intermediates with the second metal only tuning that binding so that Cu binds the CO optimally. This is unlikely on CuS because CuS already does not produce CO due to incorrect binding, so this strategy is very difficult to work on sulfide-derived catalysts.

7.3 Future work

Three areas of future work may be possible to continue with the current study. One is to understand why some sulfide-derived materials (CdS, Cu-Sb-S) produce CO but other sulfide-derived materials (InS, SnS, CuS, etc) produce $HCOO^-$. This can be done via in-situ experiments such as infrared spectroscopy (IR), Raman techniques to probe the concentration of intermediates on the catalyst surface. Two is to investigate how well Cu-M-S sulfides (M=In, Sn, Sb, Bi) work when used as photoabsorbers in photoelectrochemical (PEC) cells as some of these materials have favourable band gaps. It is possible that because of the different dynamics of PEC systems would result in a different selectivity profile.

7.3.1 In-situ IR or Raman

In-situ IR or Raman offers excellent opportunities to study the catalyst intermediates on the surface and correlate these to intermediate binding and product formation, which is important in studying the dependence of product formation, such as CO and $HCOO^-$, on intermediates such as *COOH, *CO, *OCHO (via the C-H bond), *H and *OH.

Adsorbed intermediates can be probed via in-situ IR and Raman spectroscopy,[6-8] while in-situ XAS can be used to probe the catalyst oxidation state during reaction.[9, 10] These techniques require the use of specially designed cells that enable the probing signals to

reach the catalyst and then the detector with minimum attenuation in the cell or electrolyte.[11]

7.3.2 PEC CO_2 reduction

The four materials singled out in this thesis for electrochemical CO_2 reduction are Cu-In-S, Cu-Sn-S, Cu-Sb-S and Cu-Bi-S. However, these four materials are also decent materials for photoabsorbers (more precisely, photocathodes) for photoelectrochemical cells,[12, 13] thus these materials can also be used in photoelectrochemical CO_2 reduction.[14] It is possible that these materials can behave as both photoabsorbers as well as catalysts since they contain Cu as well as main group elements, both of which are excellent reaction sites for electrochemical CO_2 reduction. The possibilities are large because they can be paired with a CdS layer for better charge separation,[15] or further paired with cocatalysts such as Cu, Zn or N-doped carbon which can then act as more efficient catalysts for the PEC system.[16]

Moreover, the applied voltage during PEC CO_2 reduction is much smaller, at about -0.2V vs RHE. What this means is that the sulfides are more stable to reduction under PEC conditions than electrochemical conditions, and because light rather than electricity is the main driving force, the product selectivities may be different even without cocatalysts or n-type layers. PEC CO_2 systems have demonstrated good performance for production of CH_4 or other reduced products as reported in literature.[17, 18]

7.3.3 Trimetallics for CO_2 reduction

Trimetallics are a better opportunity for three-element catalysts that can perform electrochemical CO_2 reduction. This is because sulfides restrict the stoichiometry of metal elements to fixed ratios in the sulfide (where the ratios may not be the same as the metal alloys which perform optimally under electrochemical conditions) and also because excess sulfur could be detrimental to the system, favouring the formation of $HCOO^-$ or H_2 instead of CO or reduced products.

An in-depth DFT screening by Abild-Pedersen and co-workers identified a number of alloys, which they classify into heavy binding (Fe, Co, Ni, Pd, Pt), Cu, and light binding (Zn, Ag, Au, Al, Ga, In, Si, Ge, Sn, Pb, As, Sb, Bi).[5] So far, for the heavy binding metals, only Pd has shown good activity alloying with Cu for electrochemical CO_2 reduction. Considering only Cu-bimetallics and Pd-bimetallics, the following list can be obtained:

Table 7.1: Pd-bimetallics and Cu-bimetallics identified by Abild-Pedersen et al for electrochemical CO_2 reduction

Pd-bimetallics	**Cu-bimetallics**
Cu-Pd	
Pd-Zn	Cu-Zn
Pd-Au	Cu-Au
	Cu-Ga
Pd-Ge	Cu-Ge
Pd-In	Cu-In
Pd-Sn	Cu-Sn
Pd-Pb	Cu-Pb
Pd-As	

Specifically, pick a heavy CO-binding metal Pd (as it is the only metal to the left of Cu that can work as an electrochemical CO_2 reduction catalyst), pick Cu, and pick a light CO-binding metal in the main group. This way, a trimetallic can be formed with two levers of tuning (Pd on one hand and the light binding metal on the other) which may result in better selectivities for reduced products such as ethylene, ethanol, acetic acid, methane, etc. The trimetallic composition should be majority Cu with smaller amount of the other two metals. From Table 7.1 (with addition of Al or Sb as these are also viable and removing Pb or As as they are toxic), 8 possible trimetallics are recommended:

Table 7.2: Cu-Pd-M trimetallics that are recommended to try for CO_2 reduction as future work

Third element CO-biased	**Third element $HCOO^-$-biased**	**Third element H_2-biased**
Cu-Pd-Zn	Cu-Pd-In	Cu-Pd-Al
Cu-Pd-Au	Cu-Pd-Sn	Cu-Pd-Ga
	Cu-Pd-Sb	Cu-Pd-Ge

The first possible group is (Cu-Pd-Zn, Cu-Pd-Au), which are composed entirely of transition metals and as such feature a more precise tuning of binding energies with a bias towards CO. Careful tuning to ensure that Zn or Au are not too excessive is necessary to avoid excess CO formation, but increased *CO concentration on the surface is beneficial because it can lead to increased Faradaic efficiency of reduced products such as ethylene or perhaps oxygenates like ethanol and acetic acid. A two-way tuning is possible to tune Cu sites to be bind CO more strongly (Pd) or more weakly (Zn and Au) to create optimal conditions for tuning Cu selectivity toward reduced products like ethylene or ethanol.

The second possible group is (Cu-Pd-In, Cu-Pd-Sn and Cu-Pd-Sb). This group features a main-group element producing $HCOO^-$ on its own as the third metal, but as already noted in literature review, these three elements alloy with Cu to form CO-selective catalysts. Thus, the concept becomes similar to the first group, but this group also has the possibility of producing $HCOO^-$ as a by-product. This means that the dynamics of this group is likely to be different than the first group, but again a two-way tuning is possible between the heavy CO-binding side (Pd) and weak CO-binding side (Cu-In, Cu-Sn, Cu-Sb).

The third possible group is (Cu-Pd-Al, Cu-Pd-Ga and Cu-Pd-Ge). The third element in this group prefers to produce H_2 on their own, but some reports in literature have observed increased formation of C_2H_4 (with Al) and CH_4 (with Ga) when these elements are alloyed with Cu. This category needs the most care when used because too much third element can result in excess H_2 production. These systems likely work by increasing the surface concentration of *H, which may have beneficial effects on reduced products formation due to easier subsequent protonation of $*C_xH_y$ intermediates.

7.3.4 In situ TEM and role of morphology

The current work focused mainly on catalyst composition on performance and there was less emphasis on morphology due to the lack of in situ TEM. However, morphology is important as mentioned in chapters 2 and 3, and in situ TEM is proposed to be carried out as future work for Cu-M catalysts as the alloys can have different morphologies which may change during the reaction, segregating or combining together with different exposed facets or even amorphous surfaces (which was also seen in the XRD in chapters 5 and 6). These can play a key role in selectivity (as seen in amorphous TH being better than crystalline SK or CS in chapter 5) and as such warrants further investigation.

From our results, it appears that small crystallite size (with more grain boundaries) or more amorphous phase may be beneficial for Cu-M based catalysts. Dopant elements such as chalcogenides or other non-metal or non-soluble elements may induce such changes by disrupting crystallites and making them smaller or more amorphous. In-situ TEM investigation on such materials can provide more clues as to the design of alloys and dopant elements in catalysts to improve their selectivity, activity and performance for electrochemical CO_2 reduction.

7.3.5 Stability and selectivity relationship of chalcogenide-derived catalysts

As chalcogenide-derived catalysts may not be very stable due to tendency of the chalcogenide (sulfur, selenium, etc) to leave, it is necessary to investigate the evolution of the catalyst and how this evolution affects the selectivity of the catalyst. This would involve the testing of different samples of the same catalyst over different periods of time and characterizing those catalysts to correlate the selectivity changes over time with the catalyst morphology and composition.

References

[1] Y. Deng *et al.*, "On the Role of Sulfur for the Selective Electrochemical Reduction of CO2 to Formate on CuSx Catalysts," *ACS Applied Materials & Interfaces,* vol. 10, no. 34, pp. 28572-28581, 2018/08/29 2018, doi: 10.1021/acsami.8b08428.

[2] T. Shinagawa, G. O. Larrazábal, A. J. Martín, F. Krumeich, and J. Pérez-Ramírez, "Sulfur-Modified Copper Catalysts for the Electrochemical Reduction of Carbon Dioxide to Formate," *ACS Catalysis,* vol. 8, no. 2, pp. 837-844, 2018/02/02 2018, doi: 10.1021/acscatal.7b03161.

[3] Y. Huang, Y. Deng, A. D. Handoko, G. K. L. Goh, and B. S. Yeo, "Rational Design of Sulfur-Doped Copper Catalysts for the Selective Electroreduction of Carbon Dioxide to Formate," *ChemSusChem,* vol. 11, no. 1, pp. 320-326, 2018, doi: https://doi.org/10.1002/cssc.201701314.

[4] W. Luc *et al.*, "SO2-Induced Selectivity Change in CO2 Electroreduction," *Journal of the American Chemical Society,* vol. 141, no. 25, pp. 9902-9909, 2019/06/26 2019, doi: 10.1021/jacs.9b03215.

[5] J. Li, J. Halldin Stenlid, M. T. Tang, H.-J. Peng, and F. Abild-Pedersen, "Screening binary alloys for electrochemical CO2 reduction towards multi-carbon products," *Journal of Materials Chemistry A,* 10.1039/D2TA02749F vol. 10, no. 30, pp. 16171-16181, 2022, doi: 10.1039/D2TA02749F.

[6] T.-C. Chou *et al.*, "Controlling the Oxidation State of the Cu Electrode and Reaction Intermediates for Electrochemical CO2 Reduction to Ethylene," *Journal of the American Chemical Society,* vol. 142, no. 6, pp. 2857-2867, 2020/02/12 2020, doi: 10.1021/jacs.9b11126.

[7] J. Gao *et al.*, "Selective C–C Coupling in Carbon Dioxide Electroreduction via Efficient Spillover of Intermediates As Supported by Operando Raman Spectroscopy," *Journal of the American Chemical Society,* vol. 141, no. 47, pp. 18704-18714, 2019/11/27 2019, doi: 10.1021/jacs.9b07415.

[8] Y. Deng and B. S. Yeo, "Characterization of Electrocatalytic Water Splitting and CO2 Reduction Reactions Using In Situ/Operando Raman Spectroscopy," *ACS Catalysis,* vol. 7, no. 11, pp. 7873-7889, 2017/11/03 2017, doi: 10.1021/acscatal.7b02561.

[9] P. De Luna *et al.*, "Catalyst electro-redeposition controls morphology and oxidation state for selective carbon dioxide reduction," *Nature Catalysis,* vol. 1, no. 2, pp. 103-110, 2018/02/01 2018, doi: 10.1038/s41929-017-0018-9.

[10] S. H. Lee *et al.*, "Oxidation State and Surface Reconstruction of Cu under CO2 Reduction Conditions from In Situ X-ray Characterization," *Journal of the American Chemical Society,* vol. 143, no. 2, pp. 588-592, 2021/01/20 2021, doi: 10.1021/jacs.0c10017.

[11] X. Li, S. Wang, L. Li, Y. Sun, and Y. Xie, "Progress and Perspective for In Situ Studies of CO2 Reduction," *Journal of the American Chemical Society,* vol. 142, no. 21, pp. 9567-9581, 2020/05/27 2020, doi: 10.1021/jacs.0c02973.

[12] S. Kamemoto, Y. Matsuda, M. Takahashi, and S. Higashimoto, "Photocatalytic water splitting on Cu2SnS3 photoelectrode: Effects of Cu/Sn composite ratio on the photoelectrochemical performance," *Catalysis Today,* vol. 411-412, p. 113820, 2023/03/01/ 2023, doi: https://doi.org/10.1016/j.cattod.2022.06.035.

[13] D. Huang, L. Li, K. Wang, Y. Li, K. Feng, and F. Jiang, "Wittichenite semiconductor of Cu3BiS3 films for efficient hydrogen evolution from solar driven photoelectrochemical water splitting," *Nature Communications,* vol. 12, no. 1, p. 3795, 2021/06/18 2021, doi: 10.1038/s41467-021-24060-5.

[14] J. Yuan and C. Hao, "Solar-driven photoelectrochemical reduction of carbon dioxide to methanol at CuInS2 thin film photocathode," *Solar Energy Materials and Solar Cells,* vol. 108, pp. 170-174, 2013/01/01/ 2013, doi: https://doi.org/10.1016/j.solmat.2012.09.024.

[15] M. Tarek *et al.*, "Hetero-structure CdS–CuFe2O4 as an efficient visible light active photocatalyst for photoelectrochemical reduction of CO2 to methanol," *International Journal of Hydrogen*

Energy, vol. 44, no. 48, pp. 26271-26284, 2019/10/08/ 2019, doi: https://doi.org/10.1016/j.ijhydene.2019.08.074.

[16] X. Chang, T. Wang, P. Yang, G. Zhang, and J. Gong, "The Development of Cocatalysts for Photoelectrochemical CO2 Reduction," *Advanced Materials,* vol. 31, no. 31, p. 1804710, 2019, doi: https://doi.org/10.1002/adma.201804710.

[17] B. Zhou *et al.*, "Highly efficient binary copper− iron catalyst for photoelectrochemical carbon dioxide reduction toward methane," *Proceedings of the National Academy of Sciences,* vol. 117, no. 3, pp. 1330-1338, 2020.

[18] Gurudayal *et al.*, "Si photocathode with Ag-supported dendritic Cu catalyst for CO2 reduction," *Energy & Environmental Science,* 10.1039/C8EE03547D vol. 12, no. 3, pp. 1068-1077, 2019, doi: 10.1039/C8EE03547D.

APPENDIX A (for chapter 4)

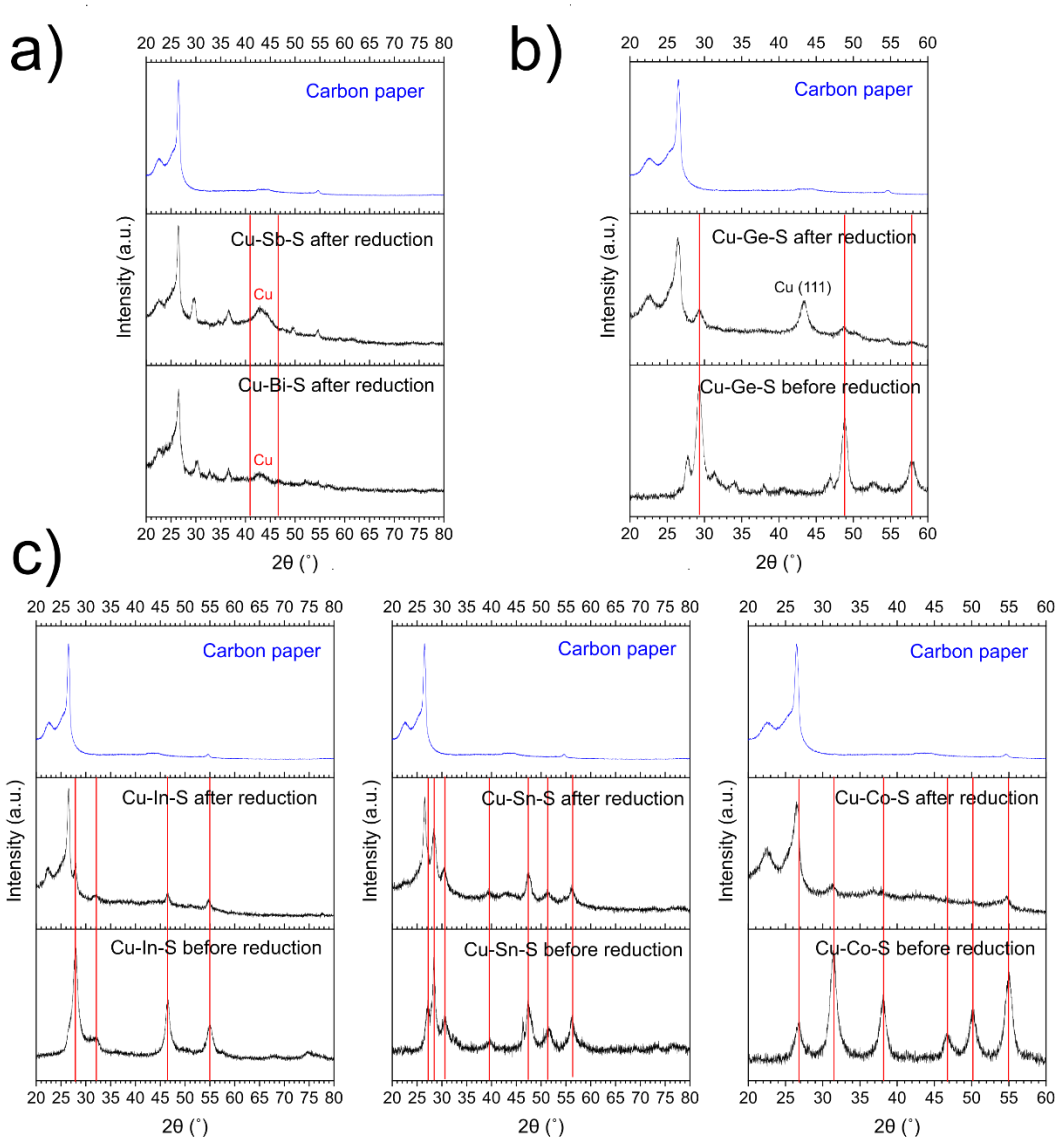

Figure A.1: a) Post-reduction XRD of Cu-Sb-S and Cu-Bi-S, showing a broad hump at 41-47° which is similar to the main peak of Cu(111) b) Post-reduction XRD of Cu-Ge-S showing the three peak structure of the original Cu-Ge-S but with an additional Cu(111) peak. c) Post-reduction XRDs of Cu-In-S, Cu-Sn-S and Cu-Co-S samples which contain the peaks of the original sulfide phases.

APPENDIX B (for chapter 5)

Section B.1: Experimental data

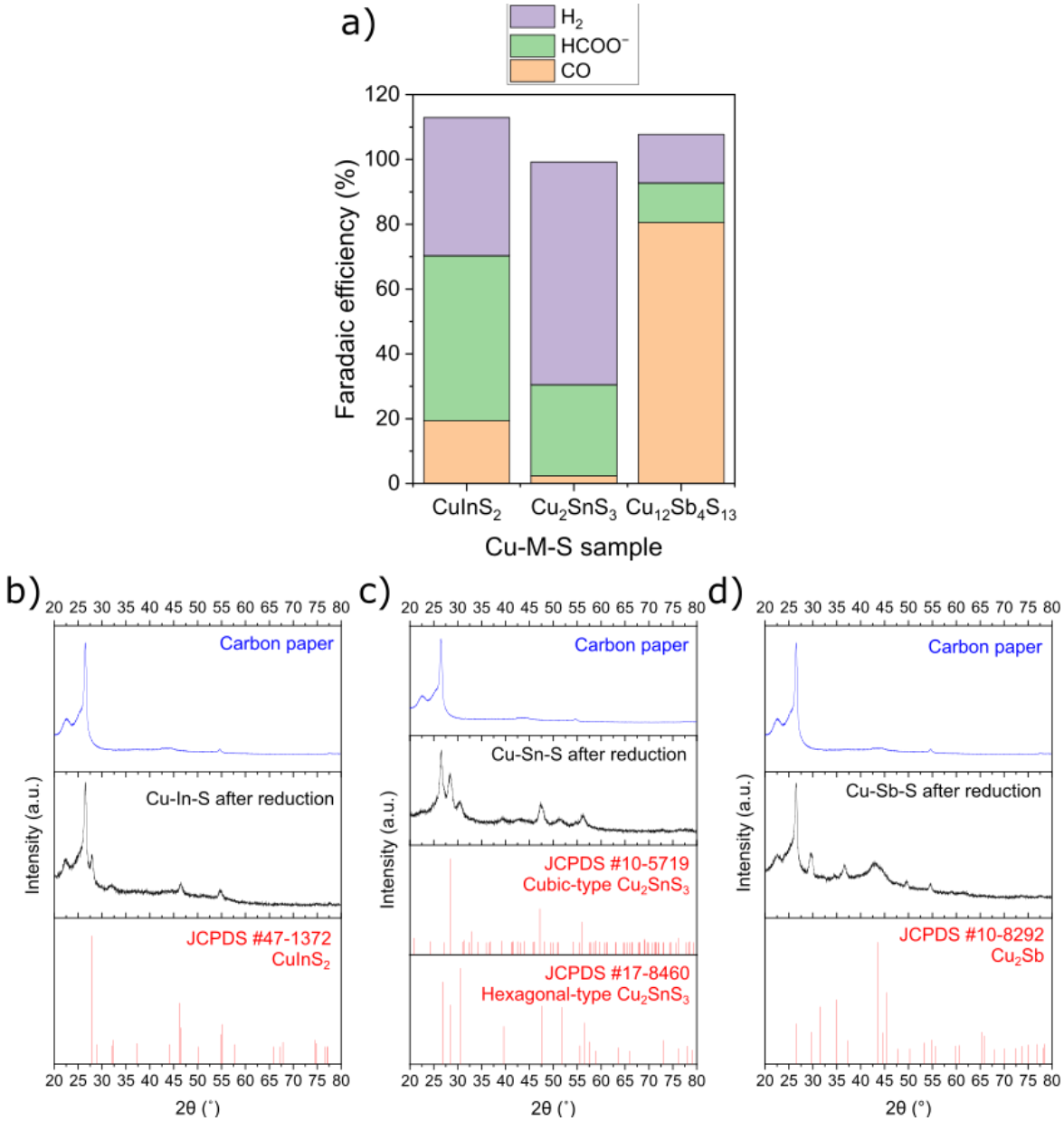

Figure B.1: a) Faradaic efficiency at -1V vs RHE and b-d) XRDs after reduction of Cu-In-S, Cu-Sn-S and Cu-Sb-S samples. The reference peaks for Cu-In-S are of cubic $CuInS_2$, the reference peaks for Cu-Sn-S are of cubic and hexagonal Cu_2SnS_3, while the reference peaks for Cu-Sb-S are of Cu_2Sb

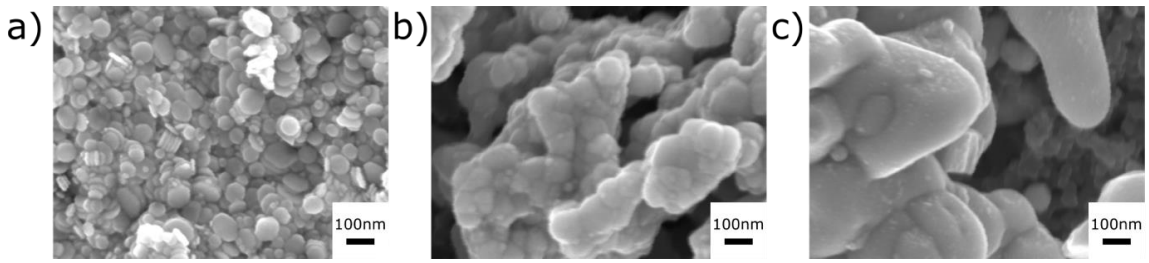

Figure B.2: Close up SEM images of the three catalyst samples on carbon paper before reduction. a) SK b) TH c) CS

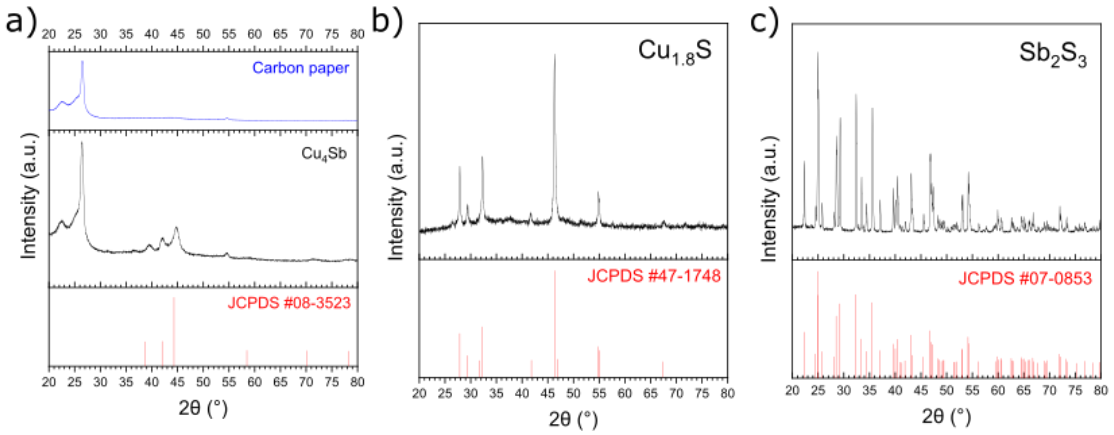

Figure B.3: XRD peaks of reference samples. Electrodeposited a) Cu_4Sb and powder b) $Cu_{1.8}S$ c) Sb_2S_3

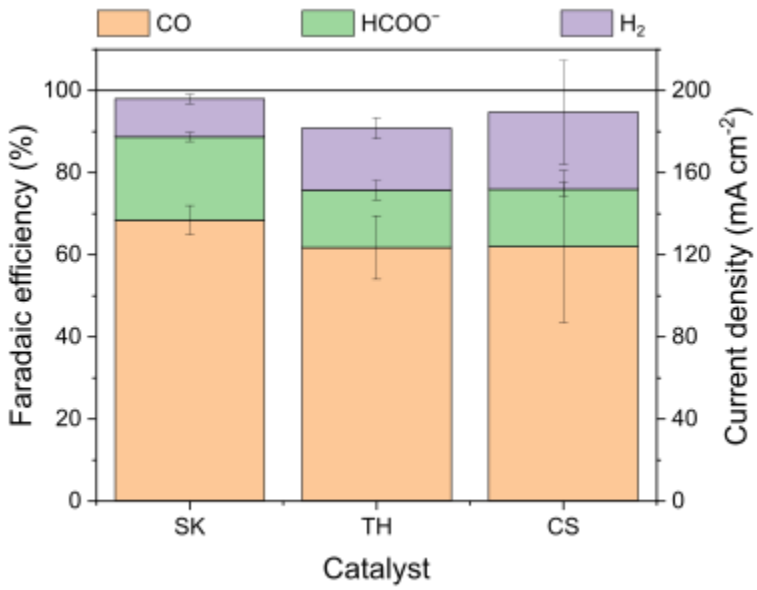

Figure B.4: Electrochemical CO_2 reduction of the three samples in applied constant 200mA cm^{-2} current density. To accommodate the high current density, carbon black at half of the weight of the catalyst was added to the catalyst inks in the middle of sonication prior to spraying on carbon paper.

Table B.1: ICP results of electrolyte for 9× loading samples used for XRD.

Sample name	[Cu] (ppb)	[Sb] (ppb)
SK	16.8	75.8
TH	14.1	19.6
CS	16.9	12.6

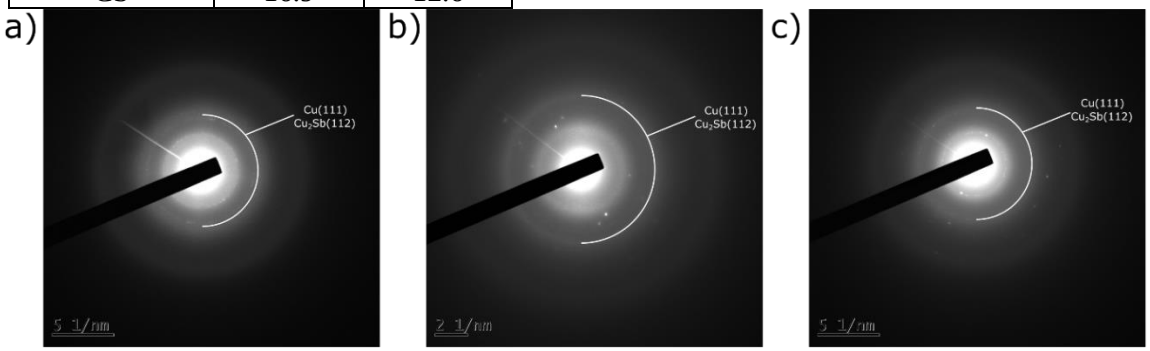

Figure B.5: SAED images of samples scraped off carbon paper after reduction at -1V vs RHE, with the main peak of Cu(111) or Cu_2Sb (112) indicated. a) SK b) TH c) CS

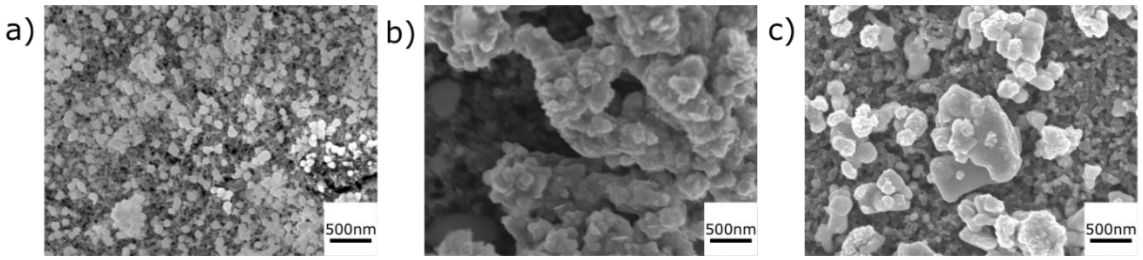

Figure B.6: SEM images of the three catalyst samples on carbon paper after reduction at -1V vs RHE. a) SK b) TH c) CS

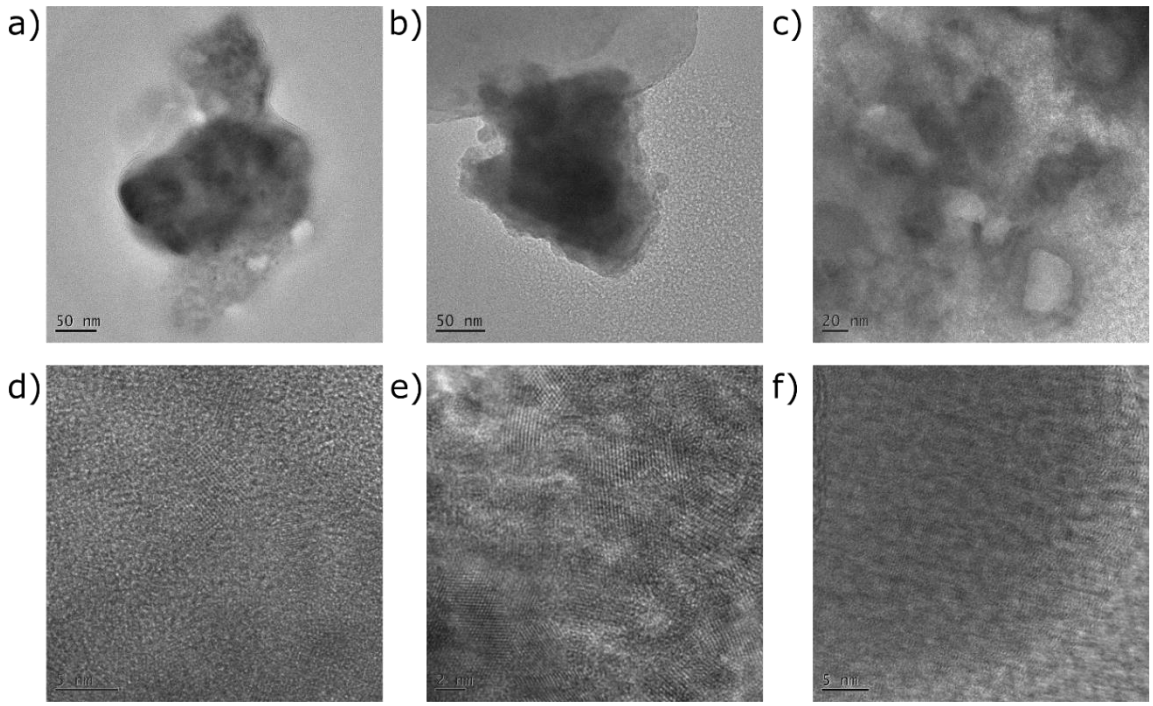

Figure B.7: TEM images of samples scraped off carbon paper after reduction at -1V vs RHE. a) SK low magnification b) TH low magnification c) CS low magnification d)SK high magnification e) TH high magnification f) CS high magnification

Section B.2: DFT calculations

B.2.1 Atomic structures of sulfur-decorated $Cu_2Sb(100)$ systems

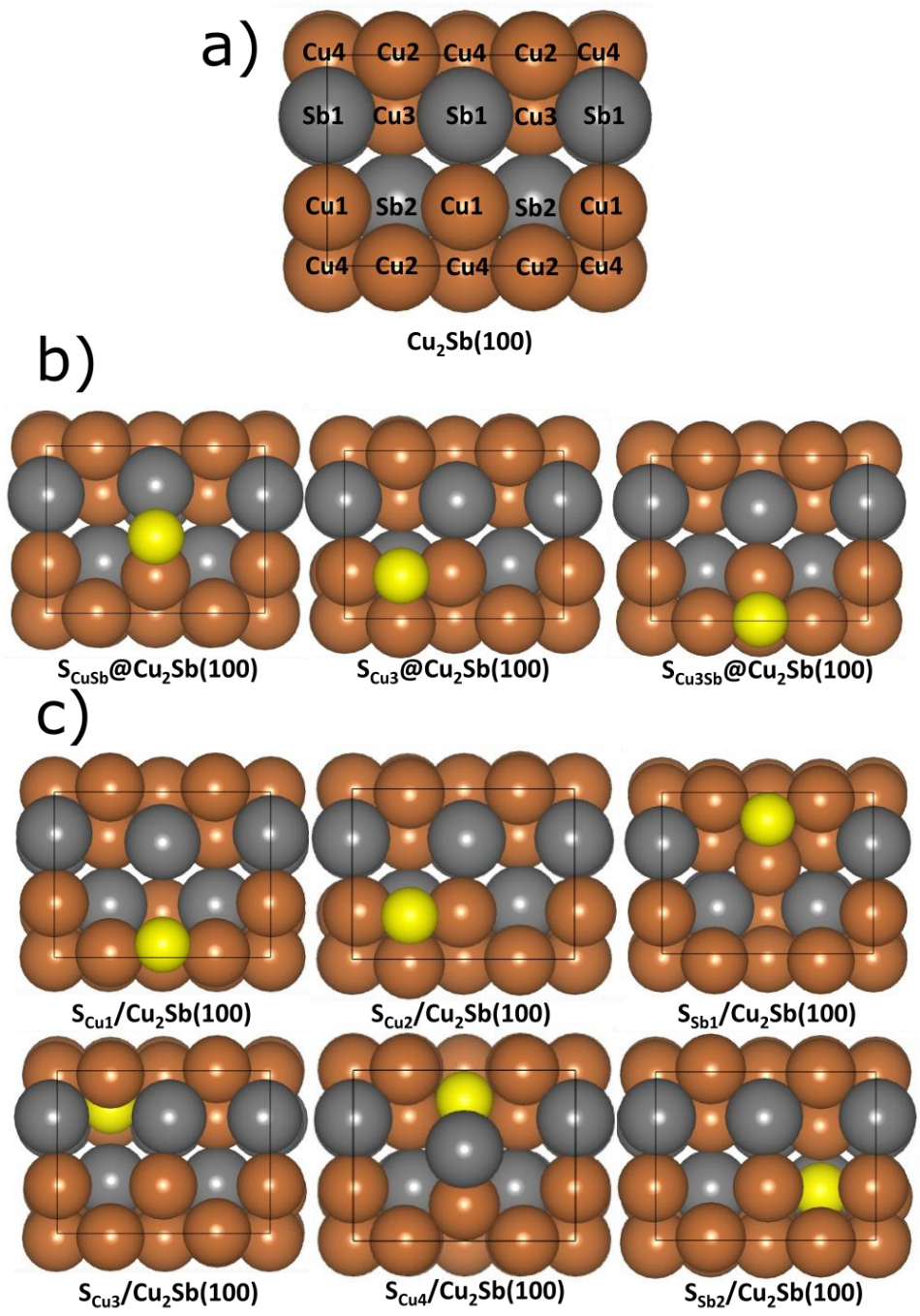

Figure B.8: Adsorption and substitutional sites for a S atom considered. (a) The clean pristine $Cu_2Sb(100)$ surface showing all symmetry inequivalent substitutional sites for a sulfur atom dopant. Note that Cu1, Cu2 and Sb1 sites in the topmost atomic layer while Cu3, Cu4 and Sb2 sites are in the next atomic layer, giving a total of six possible sites. (b) The three various adsorption configurations for a sulfur adatom on the bridge, threefold-Cu_3 and fourfold Cu_3Sb sites,

respectively. (c) The six substitutional sulfur atom dopant cases. The subscript in each notation denotes the adsorption or substitutional sites for a S atom.

B.2.2 Sulfur Stability Analysis

The energy penalty (ΔE) of forming a sulfur vacancy in each primitive cell of TH, CS and SK is calculated using equation B.1.

$$\Delta E = E_{\text{final}} - E_{\text{initial}} - E_{\text{S(g)}} \quad \text{(Equation B. 1)}$$

where E_{initial} and E_{final} refer to the electronic energy of the primitive cell of a parent phase with and without a single S atom vacancy respectively, and $E_{\text{S(g)}}$refers to the electronic energy of a single S atom in the gas phase.

The stability of Cu and Sb point defects mentioned in the main text was evaluated using the formation energy ($\Delta_{\text{form}}E$), which is defined in equation B.2.

$$\Delta_{\text{form}}E = E_{\text{defect}} - E_{\text{Cu}_2\text{Sb(100)}} + n_{\text{S}}E_{\text{S(g)}} + n_{\text{Cu}}E_{\text{fcc-Cu(s)}} + n_{\text{Sb}}E_{\text{tri-Sb(s)}} \quad \text{(Equation B. 2)}$$

where E_{defect}, and $E_{\text{Cu}_2\text{Sb(100)}}$ refer to the electronic energy of the configuration of interest and the pristine $Cu_2Sb(100)$ surface. $E_{\text{S(g)}}$, $E_{\text{fcc-Cu(s)}}$ and $E_{\text{tri-Sb(s)}}$ refer to the electronic energy of a single gas-phase S atom, Cu atom in the bulk primitive face-centered cubic crystal (space group: $F\text{m}\bar{3}\text{m}$), and an Sb atom in the bulk primitive trigonal crystal (space group: $R\bar{3}\text{m}$), respectively. n_{S}, n_{Cu} and n_{Sb} represent the number of S, Cu and Sb atoms removed or added to the system. Positive (negative) integers implying atoms added (removed).

To gauge the stability of sulfur doped systems, the desorption energy to form H_2S ($\Delta E_{\text{H}_2\text{S}}$) is used as a stability metric, which is calculated using equation B.3.

$$\Delta E_{\text{H}_2\text{S}} = E_* + E_{\text{H}_2\text{S(g)}} - E_{\text{S}^*} - E_{\text{H}_2\text{(g)}} \quad \text{(Equation B. 3)}$$

where E_*, $E_{\text{H}_2\text{S(g)}}$ and $E_{\text{H}_2\text{(g)}}$ represent the electronic energy of the surface site, an isolated H_2S molecule and an isolated H_2 molecule, respectively. In the equation used for calculating $\Delta E_{\text{H}_2\text{S}}$, the E_* for S adatoms refers to the electronic energy of Cu_2Sb (100). For the S dopant in the topmost atomic layer, E_* refers to the electronic energy of Cu_2Sb (100) containing an S atom vacancy.

Figure B.8(b) shows three different adsorption sites for a sulfur adatom: (1) Cu-Sb bridge site (S_{CuSb}@Cu_2Sb(100)), (2) threefold Cu-Cu-Cu hollow site (S_{Cu3}@Cu_2Sb(100)) and the (3) fourfold Cu-Cu-Cu-Sb hollow site (S_{Cu3Sb}@Cu_2Sb(100)). Substitutionally doped sulfur is considered in the two topmost atomic layers, giving a total of six symmetrical inequivalent doping configurations as portrayed in Figure B.8(c). These configurations are labelled as Cu1, Cu2 and Sb1 in the topmost atomic layer and Cu3, Cu4 and Sb2 in the next atomic layer. The stability of the S atoms in the

systems was evaluated with the formation energy ($\Delta_{\mathrm{form}}E$) and the desorption energy of S as H_2S (ΔE_{H_2S}) according to equations S2 and S3 respectively as tabulated in Table S3.

With S adatom on the hollow site of Cu(111) (abbreviated as S_{Cu3}@Cu(111)) as the reference system (ΔE_{H_2S} = +1.14 eV), we compared the stability of the various sulfur modified sites. This is because prior experimental and computational studies have indicated that S* remains stable on Cu (111) under CO_2RR working potentials from -0.6 V to -0.8 V vs RHE.[1] All three S adatom configurations on Cu_2Sb are less stable than S adatoms on Cu(111). Hence S adatoms are less likely to adsorb on Cu_2Sb(100) during the operating condition of -1.0 eV. Since ΔE_{H_2S} for S_{CuSb}@Cu_2Sb(100) is at least around 0.6 eV more positive than that for the other two adsorption configuration, S_{CuSb}@Cu_2Sb(100) was not considered in further analyses. The S atom substitutionally doped at the copper sites in the topmost atomic layer (i.e., S_{Cu1}/Cu_2Sb(100), S_{Cu2}/Cu_2Sb(100)) also showed poorer stability than S* on Cu (111). However, S substituting at the Sb site in topmost atomic layer (i.e. S_{Sb1}/Cu_2Sb(100)) is more stable than S_{Cu3}@Cu(111)by 0.59 eV.

Table B.2. Formation energies of the sulfur-decorated ($\Delta_{\mathrm{form}}E_{S*}$) and vacancy ($\Delta_{\mathrm{form}}E_{V}$) surface motifs and desorption energies of the sulfur in sulfur-decorated systems as H_2S (ΔE_{H_2S}).

	$\Delta_{\mathrm{form}}E_{S*/V}$ /eV	ΔE_{H_2S} / eV
S_{Cu3}@Cu(111), reference	-4.60	+1.14
S_{CuSb}@Cu_2Sb(100)	-3.80	+0.34
S_{Cu3}@Cu2Sb(100)	-4.46	+1.00
S_{Cu3Sb}@Cu2Sb(100)	-4.39	+0.93
S_{Cu1}/Cu_2Sb(100)	-4.45	+0.79
S_{Cu2}/Cu_2Sb(100)	-4.11	+0.80
S_{Sb1}/Cu_2Sb(100)	-4.14	+1.73
S_{Cu3}/Cu_2Sb(100)	-2.66	-0.99
S_{Cu4}/Cu_2Sb(100)	-3.25	-0.05
S_{Sb2}/Cu_2Sb(100)	-3.34	+0.93
V_{Cu1}/Cu_2Sb(100)	-0.20	-
V_{Cu2}/Cu_2Sb(100)	+0.16	-
V_{Sb1}/Cu_2Sb(100)	+1.05	-

When an S atom desorbs from the surface as H_2S, it inevitably leaves behind a vacancy. For instance, the S atom in S_{Cu1}/Cu_2Sb(100) desorbs as H_2S leaving a V_{Cu1}/Cu_2Sb(100) vacancy structure. Correspondingly, S_{Cu2}/Cu_2Sb(100) forms the V_{Cu2}/Cu_2Sb(100) structure and S_{Sb1}/Cu_2Sb(100) forms the V_{Sb1}. The formation energy of the three vacancy sites trend as V_{Cu1}/Cu_2Sb(100) >

$V_{Cu2}/Cu_2Sb(100)$ > $V_{Sb1}/Cu_2Sb(100)$, with the formation of $V_{Cu1}/Cu_2Sb(100)$ being most thermodynamically favoured. We also predict that $V_{Sb1}/Cu_2Sb(100)$ is unlikely to form, since $S_{Sb1}/Cu_2Sb(100)$ is predicted to be stable during operating conditions and the $\Delta_{\mathrm{form}}E_{\mathrm{V}}$ value for V_{Sb1} at least 1.0 eV more positive than that for $V_{Cu1}/Cu_2Sb(100)$ and $V_{Cu2}/Cu_2Sb(100)$. Hence, we include $V_{Cu1}/Cu_2Sb(100)$ and $V_{Cu2}/Cu_2Sb(100)$ in our analysis of selectivity and reactivity trends towards 2e-CO_2RR. As a limiting case of a restructured surface, we also consider the $Cu_2Sb(101)$ stepped surface.

For the substitutionally doped sulfur in the second atomic layer ($S_{Cu3}/Cu_2Sb(100)$, $S_{Cu4}/Cu_2Sb(100)$ and $S_{Sb2}/Cu_2Sb(100)$) to desorb as H_2S, the sulfur atom must first diffuse through the solid to the surface before it can be hydrogenated. The vacancy is thus created in the topmost layer. For a fair comparison of $\Delta E_{\mathrm{H_2S}}$, we assume the most stable $V_{Cu1}/Cu_2Sb(100)$ as the vacancy structure after H_2S desorption. While the three configurations gave $\Delta E_{\mathrm{H_2S}}$ values that are less positive than S_{Cu3}@Cu(111), the S atom must first diffuse through the solid to the surface before it can be hydrogenated. This diffusion process is likely activated, hence S atoms in the second atomic layer could be kinetically stabilised during the operating conditions.

B.2.3 Additional Computational Details on the Computational Hydrogen Electrode Approach

The catalytic activity of the surface models was analysed using the computational hydrogen electrode approach[2], in which the electrochemical potential of a proton–electron pair, $\tilde{\mu}(\mathrm{H^+ + e^-})$, is related to the chemical potential of H_2 at ambient conditions (278.25 K, 1 atm, 0 V), $\mu_{\mathrm{H_2}}$, and the operating potential vs. RHE, U, according to equation B.4:

$$\tilde{\mu}_{(\mathrm{H^+ + e^-})} = \frac{1}{2}\mu_{\mathrm{H_2}}(278.15\ \mathrm{K}, 1\ \mathrm{atm}, 0\ \mathrm{V}) - eU \qquad \text{(Equation B. 4)}$$

where e is the elementary charge. The potential-dependent Gibbs energy change ($\Delta_{\mathrm{r}}G(U)$) for any reaction can be estimated using equation B.5:

$$\Delta_{\mathrm{r}}G(U) = \Delta E_{ele} + \Delta E_{ZP} + \Delta \int C_p\ \mathrm{d}T + T\Delta S + \Delta E_{sol} - neU \qquad \text{(Equation B. 5)}$$

where ΔE_{ZPC} is the change in zero-point energy, $\Delta \int C_p\ \mathrm{d}T$ is the change in enthalpic temperature correction, T is the temperature, ΔS is the entropy change, ΔE_{sol} is the solvation energy and n is the number of electrons transferred. We adopted the value of these terms as already evaluated in Tang et al. [3] as tabulated in Table B.4.

We evaluated the catalytic performance in two parts. We studied the selectivity towards electrocatalytic CO or formate formation pathways. We then analysed trends in electrochemical barriers from the free energy diagrams.

B.2.4 Adsorption metrics analysis

The adsorption energies of CO_2 reduction reaction intermediates like H* ($\Delta_{ads}G_{H^*}$), HCOO* ($\Delta_{ads}G_{HCOO^*}$), COOH* ($\Delta_{ads}G_{COOH^*}$) and CO* ($\Delta_{ads}G_{CO^*}$) were calculated using H_2, H_2O and CO_2 as reference states for H-, O- and C-containing species as shown in equations B.6 – B.9. To minimize the error in the gas phase energy calculations using the PBE functional as reported by Peterson et al., we corrected the Gibbs energy of CO, CO_2, H_2 and H_2O by -0.51, +0.13, -0.08 and 0.06 eV, respectively.[4]

As such, the potential dependent adsorption Gibbs energies of H*, HCOO*, COOH* and CO* are given by equations B.6 – B.9:

$$\Delta_{ads}G_{H^*}(U) = G_{H^*} - \frac{1}{2}G_{H_2} - G_* + eU \quad \text{(Equation B. 6)}$$

$$\Delta_{ads}G_{HCOO^*}(U) = G_{COOH^*} - G_{CO_2} - \frac{1}{2}G_{H_2} - G_* + eU \quad \text{(Equation B. 7)}$$

$$\Delta_{ads}G_{COOH^*}(U) = G_{HCOO^*} - G_{CO_2} - \frac{1}{2}G_{H_2} - G_* + eU \quad \text{(Equation B. 8)}$$

$$\Delta_{ads}G_{CO^*}(U) = G_{CO^*} + G_{H_2O} - G_{CO_2} - G_{H_2} - G_* + 2eU \quad \text{(Equation B. 9)}$$

The 11 models that were considered further besides the reference $Cu_2Sb(100)$ are the two S adatom structures, (i) S_{Cu3}@$Cu_2Sb(100)$ and (ii) S_{Cu3Sb}@$Cu_2Sb(100)$; three structures with S as a dopant in the topmost atomic layer, (iii) $S_{Cu1}/Cu_2Sb(100)$, (iv) $S_{Cu2}/Cu_2Sb(100)$ and (v) $S_{Sb1}/Cu_2Sb(100)$, three structures with S as a dopant in the second topmost atomic layer, (vi) $S_{Cu3}/Cu_2Sb(100)$, (vii) $S_{Cu4}/Cu_2Sb(100)$ and (viii) $S_{Sb2}/Cu_2Sb(100)$, two vacancy structures, (ix) $V_{Cu1}/Cu_2Sb(100)$ and (x) $V_{Cu2}/Cu_2Sb(100)$ and lastly (xi) $Cu_2Sb(101)$.

Table B.3. Adsorption Gibbs energy for key intermediates i.e., H*, COOH*, HCOO* and CO*, involved in 2e-CO_2RR

Surface Structure	$\Delta_{ads}G_{H^*}$/ eV	$\Delta_{ads}G_{COOH^*}$/ eV	$\Delta_{ads}G_{HCOO^*}$ / eV	$\Delta_{ads}G_{CO^*}$ / eV
Cu(111)	-0.17	0.58	-0.45	0.17
$Cu_2Sb(100)$, reference	-0.05	0.66	0.09	0.17
S_{Cu3}@$Cu_2Sb(100)$	***0.08***	***0.70***	***0.44***	***0.21***
S_{Cu3Sb}@$Cu_2Sb(100)$	***0.14***	***0.85***	***0.38***	***0.31***
$S_{Cu1}/Cu_2Sb(100)$	***0.22***	***0.96***	***0.54***	***0.43***

S_{Cu2}/Cu_2Sb(100)	***0.09***	***0.73***	***0.47***	***0.19***
S_{Sb1}/Cu_2Sb(100)	***0.06***	***0.77***	***0.21***	***0.18***
V_{Cu1}/Cu_2Sb(100)	***0.02***	-0.22	***0.14***	0.11
V_{Cu2}/Cu_2Sb(100)	-0.08	***0.75***	***0.25***	***0.21***
S_{Cu3}/Cu_2Sb(100)	-0.20	0.12	-0.24	0.06
S_{Cu4}/Cu_2Sb(100)	-0.20	0.58	-0.27	-0.26
S_{Sb2}/Cu_2Sb(100)	***0.01***	0.29	-0.14	0.28
Cu_2Sb(101)	-0.84	0.50	-0.50	-0.05

The adsorption Gibbs energy is calculated using DFT-derived electronic energies and the correction terms in Table B.4. Values which are in bold and italics are more positive than that of the reference Cu_2Sb(100).

We determined the most stable adsorption sites of H*, COOH*, HCOO* and CO* on all Cu_2Sb-based structures with the adsorption energies shown in Table B.2. The Cu-Cu bridge site is the most stable adsorption site for H* and CO*. COOH* and HCOO* adopted η^2(C,O) and η^2(O,O) adsorption configurations on two adjacent Cu atoms. These adsorption configurations are shown in Figure SB.9. We first compare adsorption energies of reaction intermediates on our reference surface, Cu_2Sb(100), against that on a prototypical CO_2RR catalyst, Cu(111). We note that alloying of Sb into Cu as Cu_2Sb(100) results in negligible change in CO* adsorption strength while the adsorption strength of H*, COOH* and HCOO* decreases.

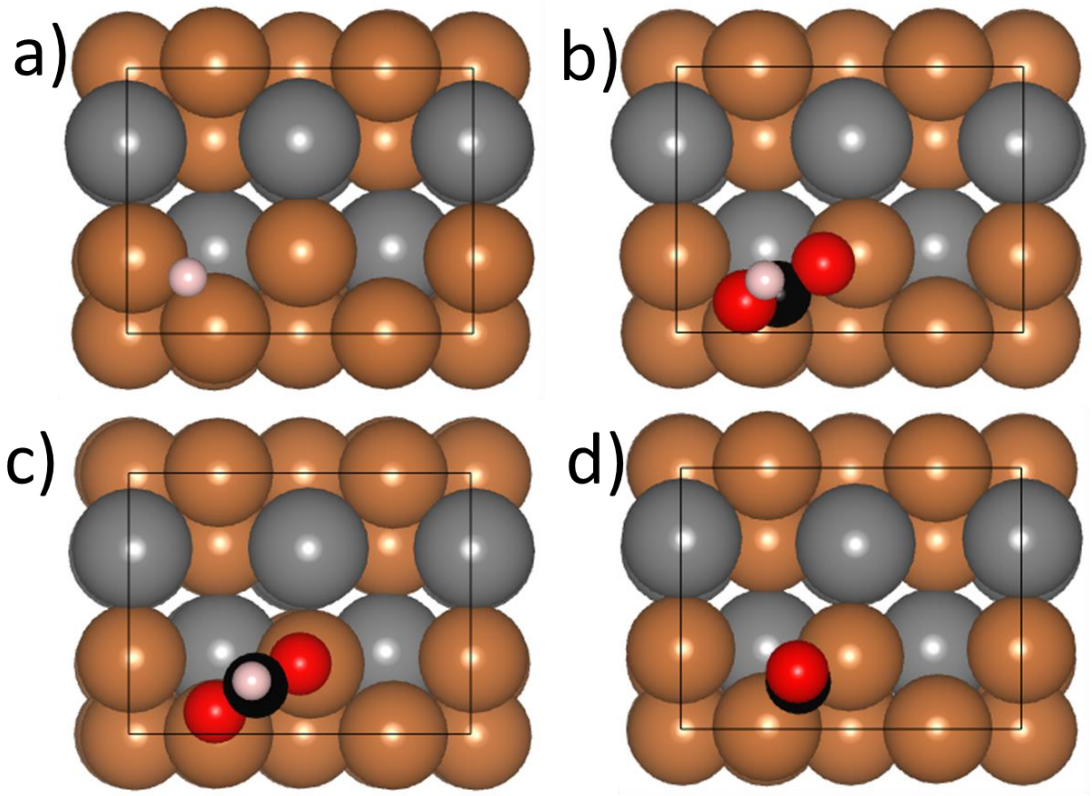

Figure B.9. Adsorption configurations of the key intermediates i.e., (a) *H, (b) *COOH, (c) HCOO* and (d) *CO, involved in 2e-CO_2RR.

We then compare the adsorption energies on all surfaces in Table B.2 against those on $Cu_2Sb(100)$. Note that values bolded and italicized are more positive than the corresponding ones for $Cu_2Sb(100)$. than the reference surface, $Cu_2Sb(100)$. Similar adsorption configurations of intermediates are obtained across sulfur-modified Cu sites, Cu vacancies, and $Cu_2Sb(101)$. From Table B.2, one can dichotomize the set of surface models into two group in terms of adsorption energies. Generally, sulfur as an adatom or as a substitutional dopant in the topmost layer and in vacancy structures weakened the binding strength of the adsorbates relative to $Cu_2Sb(100)$. Sulfur dopants in the second atomic layer and Cu_2Sb (101) enhanced the binding of adsorbates relative to $Cu_2Sb(100)$. More importantly, eight surfaces, i.e., $S_{Cu3}@Cu_2Sb(100)$, $S_{Cu3Sb}@Cu_2Sb(100)$, $S_{Cu1}/Cu_2Sb(100)$, $S_{Cu2}/Cu_2Sb(100)$, $S_{Sb1}/Cu_2Sb(100)$, $S_{Sb2}/Cu_2Sb(100)$, $V_{Cu2}/Cu_2Sb(100)$ bind CO* less strongly than both Cu (111) and Cu_2Sb (100). It has been demonstrated that CO_2RR catalysts that are selective towards the 2e products experimentally possess a CO* binding energy that is weaker than that on Cu(111). [3, 5]

The weaker binding of CO* on the eight surfaces will promote CO* desorption rather than further reduction to CHO* or COH*. Since the CS, SK and TH samples showed a high selectivity towards the 2e-CO_2RR products even at a more negative applied voltage of -1.2 V, these eight active site motifs are more likely to be present in the catalytic active Cu-Sb-S phases.

B.2.5 2e$^-$ CO_2RR and HER catalytic activity analysis

We adopted a similar approach by Tang et al. to evaluate the selectivity of the 2e-CO_2RR products (i.e., CO and HCOOH).[3] It has been well-accepted that the formation of COOH* occurs via the electrochemical hydrogenation of a CO_2. The driving force for COOH* formation as a function of the applied potential is given by $\Delta_{\mathrm{ads}}G_{\mathrm{COOH}^*}(U)$ as in equation B.10:

$$\Delta_{\mathrm{R1}}G(\mathrm{CO_2(g)} + * + \mathrm{H^+} + \mathrm{e^-} \rightarrow \mathrm{COOH}^*) = \Delta_{\mathrm{ads}}G_{\mathrm{COOH}^*}(U) \quad \text{(Equation B. 10)}$$

HCOO* occurs from the chemical step involving CO_2 and H*, whose formation is unaffected by the applied potential and is governed by equation B.11:

$$\Delta_{\mathrm{R2}}G(\mathrm{CO_2(g)} + \mathrm{H}^* \rightarrow \mathrm{HCOO}^*) = \Delta G_{\mathrm{HCOO}^*}(U) - \Delta G_{\mathrm{H}^*}(U) \quad \text{(Equation B. 11)}$$

Equation B.12 is also required to describe the availability of H* for the formation of HCOO*:

$$\Delta_{\mathrm{R3}}G(* + \mathrm{H^+} + \mathrm{e^-} \rightarrow \mathrm{H}^*) = \Delta G_{\mathrm{H}^*}(U) \quad \text{(Equation B. 12)}$$

Essentially, a product is more selective at a specific operating potential if the thermodynamic driving force to produce the relevant intermediate (COOH* or HCOO*) from the reactant species is larger. One can then use $\Delta_{\mathrm{R1}}G - \Delta_{\mathrm{R2}}G$ as a descriptor for determining the selectivity of a given active site motif towards either CO or formate. A more negative (positive) value indicates a larger driving force for the CO (formate) pathway.

To plot the potential energy diagrams, the 2e-CO_2RR pathway forming CO considered is given by B.13 – B.15 while that forming formate as HCOOH is given by B.16 – B.18:

$$\mathrm{CO_2(g)} + * + (\mathrm{H^+} + \mathrm{e^-}) \rightarrow \mathrm{COOH}^* \ (\Delta_{\mathrm{C1}}G) \quad \text{(Equation B. 13)}$$

$$\mathrm{COOH}^* + (\mathrm{H^+} + \mathrm{e^-}) \rightarrow \mathrm{CO}^* + \mathrm{H_2O} \ (\Delta_{\mathrm{C2}}G) \quad \text{(Equation B. 14)}$$

$$\mathrm{CO}^* \rightarrow \mathrm{CO} + * \ (\Delta_{\mathrm{C3}}G) \quad \text{(Equation B. 15)}$$

$$* + (\mathrm{H^+} + \mathrm{e^-}) \rightarrow \mathrm{H}^* \ (\Delta_{\mathrm{F1}}G) \quad \text{(Equation B. 16)}$$

$$\mathrm{CO_2} + \mathrm{H}^* \rightarrow \mathrm{HCOO}^* \ (\Delta_{\mathrm{F2}}G) \quad \text{(Equation B. 17)}$$

$$\mathrm{HCOO}^* + (\mathrm{H^+} + \mathrm{e^-}) \rightarrow \mathrm{HCOOH} + * \ (\Delta_{\mathrm{F3}}G) \quad \text{(Equation B. 18)}$$

In addition, hydrogen evolution reaction (HER) is considered to proceed via B.19 – B.20:

$$* + (\mathrm{H^+} + \mathrm{e^-}) \rightarrow \mathrm{H}^* \ (\Delta_{\mathrm{H1}}G) \quad \text{(Equation B. 19)}$$

$$H^* + (H^+ + e^-) \rightarrow H_2 + * \ (\Delta_{H2}G) \qquad \text{(Equation B. 20)}$$

The Gibbs energy changes for the CO, formate and HER pathways at 0.0 V are given in Table B.4, B.5 and B.6 respectively.

B.2.6 Other DFT data

Table B.4: DFT-calculated surface energies. The description of the orthogonal, asymmetric slabs of different Cu_2Sb facets encompassing only the primitive surface cell used in terms of slab thickness, constraints on the slab, lateral lattice parameters (*a* and *b*), surface area per primitive surface cell and surface energy.

Facet	Termination	Total no. of layers	No. of fixed layers	*a* / Å	*b* / Å	Surface Area / Å^2	Surface energy / J m^{-2}
(100)	Cu,Sb	6	2	3.98	6.09	24.12	2.38
(110)	Cu,Sb	6	2	5.63	6.09	34.28	2.48
(110)	Cu	6	2	5.63	6.09	24.28	2.44
(101)	Cu,Sb	9	3	7.28	3.98	28.95	2.67
(001)	Cu,Sb	9	3	3.97	3.97	15.76	3.28

Table B.5. Gas-phase and adsorbate Gibbs energy correction. Contributions to the Gibbs energy of gas-phase and adsorbate species from zero-point energy (E_{ZP}), enthalpic temperature correction ($\int C_p dT$), entropic contribution ($-TS$) and solvation correction involved in 2e-CO_2RR pathway.

Species	E_{ZP} / eV	$\int C_p dT$ / eV	$-TS$ / eV	E_{sol} / eV
CO	0.13	0.09	-0.67	-
CO_2	0.31	0.10	-0.67	-
HCOOH	0.90	0.11	-0.99	-
H_2	0.27	0.09	-0.44	-
H_2O	0.57	0.10	-0.67	-
HCOO*	0.61	0.06	-0.12	0.00
COOH*	0.62	0.09	-0.17	-0.25
H*	0.13	0.01	-0.02	0.00
CO*	0.17	0.07	-0.16	-0.10

Table B.6. Selectivity metrics at operating voltage of -1.0 V for Cu(111) and all 12 Cu_2Sb-based surface motifs. $\Delta_{R1}G$ and $\Delta_{R2}G$ govern the driving force for COOH* and HCOO* formation respectively. A positive (negative) value of $\Delta_{R1}G - \Delta_{R2}G$ would favour CO (formate). The $\Delta_{R3}G$ is used as a descriptor to define surface hydrogenation. A negative $\Delta_{R3}G$ value favours surface hydrogenation.

Surface Structure	$\Delta_{R1}G$ / eV	$\Delta_{R2}G$ / eV	$\Delta_{R1}G$ - $\Delta_{R2}G$ / eV	$\Delta_{R3}G$ / eV
Cu(111)	-0.42	-0.28	-0.15	-1.17
Cu_2Sb(100)	-0.34	0.14	-0.48	-1.05
S_{Cu3}@Cu_2Sb(100)	-0.30	0.36	-0.66	-0.92
S_{Cu3Sb}@Cu_2Sb(100)	-0.15	0.24	-0.39	-0.86
S_{Cu1}/Cu_2Sb(100)	-0.04	0.32	-0.36	-0.78
S_{Cu2}/Cu_2Sb(100)	-0.27	0.38	-0.65	-0.91

$S_{Sb1}/Cu_2Sb(100)$	-0.23	0.15	-0.38	-0.94
$S_{Cu3}/Cu_2Sb(100)$	-0.88	-0.03	-0.85	-1.20
$S_{Cu4}/Cu_2Sb(100)$	-0.42	-0.08	-0.35	-1.20
$S_{Sb2}/Cu_2Sb(100)$	-0.71	-0.15	-0.56	-0.99
$V_{Cu1}/Cu_2Sb(100)$	-1.22	0.13	-1.34	-0.98
$V_{Cu2}/Cu_2Sb(100)$	-0.25	0.33	-0.58	-1.08
$Cu_2Sb(101)$	-0.50	0.34	-0.84	-1.84

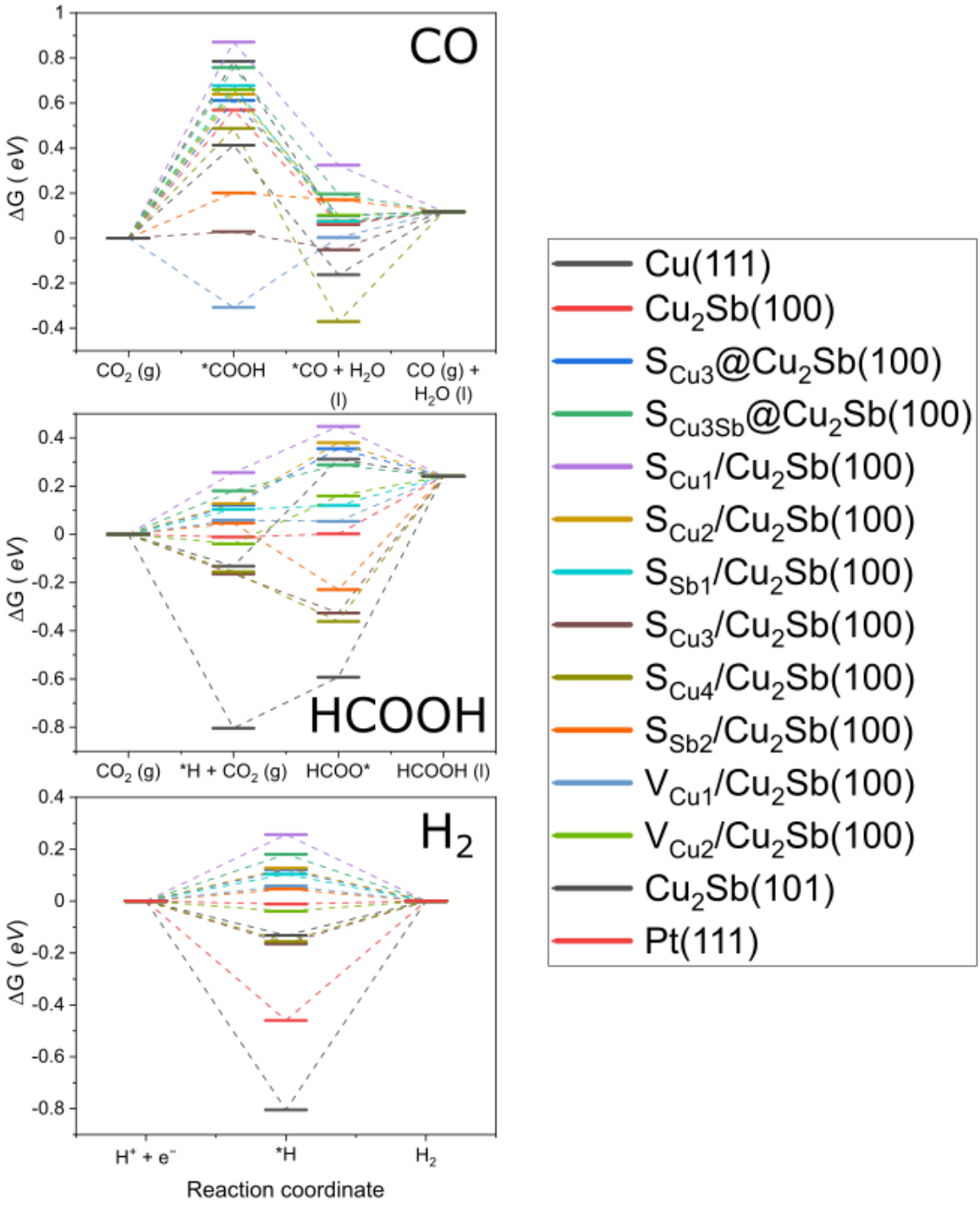

Figure B.10: Free energy diagrams of all three reaction pathways at 0V

Table B.7. Gibbs energy change for each elementary step considered in equations B.13 – B.15 for the 2e-CO_2RR CO pathway at 0.0 V. The Gibbs energy changes at any applied potential can be calculated, in principle, using the computational hydrogen electrode approach.

Surface Structure	$\Delta_{C1}G$ / eV	$\Delta_{C2}G$ / eV	$\Delta_{C3}G$ / eV
Cu(111)	0.79	-0.73	0.06
Cu_2Sb(100)	0.57	-0.50	0.05
S_{Cu3}@Cu_2Sb(100)	0.61	-0.51	0.02
S_{Cu3Sb}@Cu_2Sb(100)	0.76	-0.56	-0.08
S_{Cu1}/Cu_2Sb(100)	0.87	-0.55	-0.21
S_{Cu2}/Cu_2Sb(100)	0.64	-0.56	0.04
S_{Sb1}/Cu_2Sb(100)	0.68	-0.60	0.04
S_{Cu3}/Cu_2Sb(100)	0.03	-0.08	0.17
S_{Cu4}/Cu_2Sb(100)	0.49	-0.86	0.49
S_{Sb2}/Cu_2Sb(100)	0.20	-0.03	-0.05
V_{Cu1}/Cu_2Sb(100)	-0.31	0.31	0.11
V_{Cu2}/Cu_2Sb(100)	0.66	-0.56	0.02
Cu_2Sb(101)	0.41	-0.58	0.28

Table B.8. Gibbs energy change for each elementary step considered in equations B.16 – B.18 for the 2e-CO_2RR formate pathway 0.0 V. The Gibbs energy changes at any applied potential can be calculated, in principle, using the computational hydrogen electrode approach.

Surface Structure	$\Delta_{F1}G$ / eV	$\Delta_{F2}G$ / eV	$\Delta_{F3}G$ / eV
Cu(111)	-0.13	0.44	0.07
Cu_2Sb(100)	-0.01	0.01	0.24
S_{Cu3}@Cu_2Sb(100)	0.12	0.23	-0.11
S_{Cu3Sb}@Cu_2Sb(100)	0.18	0.11	-0.05
S_{Cu1}/Cu_2Sb(100)	0.26	0.19	-0.21
S_{Cu2}/Cu_2Sb(100)	0.13	0.25	-0.14
S_{Sb1}/Cu_2Sb(100)	0.10	0.02	0.12
S_{Cu3}/Cu_2Sb(100)	-0.16	-0.16	0.57
S_{Cu4}/Cu_2Sb(100)	-0.16	-0.21	0.60
S_{Sb2}/Cu_2Sb(100)	0.05	-0.28	0.47
V_{Cu1}/Cu_2Sb(100)	0.06	0.00	0.19
V_{Cu2}/Cu_2Sb(100)	-0.04	0.20	0.08
Cu_2Sb(101)	-0.80	0.21	0.83

Table B.9. Gibbs energy change for each elementary step considered in equations B.19 – B.20 for the HER pathway 0.0 V. The Gibbs energy changes at any applied potential can be calculated, in principle, using the computational hydrogen electrode approach.

Surface Structure	$\Delta_{H1}G$ / eV	$\Delta_{H2}G$ / eV
Cu(111)	-0.13	0.13
Cu_2Sb(100)	-0.01	0.01
S_{Cu3}@Cu_2Sb(100)	0.12	-0.12

S_{Cu3Sb}@Cu_2Sb(100)	0.18	-0.18
S_{Cu1}/Cu_2Sb(100)	0.26	-0.26
S_{Cu2}/Cu_2Sb(100)	0.13	-0.13
S_{Sb1}/Cu_2Sb(100)	0.10	-0.10
S_{Cu3}/Cu_2Sb(100)	-0.16	0.16
S_{Cu4}/Cu_2Sb(100)	-0.16	0.16
S_{Sb2}/Cu_2Sb(100)	0.05	-0.05
V_{Cu1}/Cu_2Sb(100)	0.06	-0.06
V_{Cu2}/Cu_2Sb(100)	-0.04	0.04
Cu_2Sb(101)	-0.80	0.80
Pt(111)	-0.46	0.46

References

[1] R. Garcia-Muelas, F. Dattila, T. Shinagawa, A. J. Martin, J. Perez-Ramirez, and N. Lopez, "Origin of the Selective Electroreduction of Carbon Dioxide to Formate by Chalcogen Modified Copper," *J Phys Chem Lett,* vol. 9, no. 24, pp. 7153-7159, Dec 20 2018, doi: 10.1021/acs.jpclett.8b03212.

[2] J. K. Nørskov *et al.*, "Origin of the Overpotential for Oxygen Reduction at a Fuel-Cell Cathode," *The Journal of Physical Chemistry B,* vol. 108, no. 46, pp. 17886-17892, 2004/11/01 2004, doi: 10.1021/jp047349j.

[3] M. T. Tang, H. Peng, P. S. Lamoureux, M. Bajdich, and F. Abild-Pedersen, "From electricity to fuels: Descriptors for C1 selectivity in electrochemical CO2 reduction," *Applied Catalysis B: Environmental,* vol. 279, 2020, doi: 10.1016/j.apcatb.2020.119384.

[4] A. A. Peterson, F. Abild-Pedersen, F. Studt, J. Rossmeisl, and J. K. Nørskov, "How copper catalyzes the electroreduction of carbon dioxide into hydrocarbon fuels," *Energy & Environmental Science,* vol. 3, no. 9, 2010, doi: 10.1039/c0ee00071j.

[5] K. P. Kuhl, T. Hatsukade, E. R. Cave, D. N. Abram, J. Kibsgaard, and T. F. Jaramillo, "Electrocatalytic conversion of carbon dioxide to methane and methanol on transition metal surfaces," *Journal of the American Chemical Society,* vol. 136, no. 40, pp. 14107-13, Oct 8 2014, doi: 10.1021/ja505791r.